UNIVERSITÀ
DEGLI STUDI
FIRENZE

DOTTORATO DI RICERCA IN
INTERNATIONAL DOCTORATE IN ATOMIC AND
MOLECULAR PHOTONICS

CICLO XXX

COORDINATORE: Prof. Francesco Saverio Cataliotti

Room-temperature Source for Metrological Grade Terahertz Spectroscopy.

Settore Scientifico Disciplinare: FIS/03

Dottorando
Michele De Regis

Tutore
Dr. Paolo De Natale

Coordinatore
Prof. Francesco Saverio Cataliotti

Anni 2014/2017

Contents

Introduction

The terahertz (THz) spectral window, that is generally considered to span from 1 to 10 THz, is nowadays crucial for plenty of every-day-life and scientific applications, as homeland security, environment monitoring, quality inspection of food and biomedicine. Among these applications, high precision THz spectroscopy of rotational and ro-vibrational molecular transitions promises to deliver many novel physical insights.

But, despite its primary importance, a considerable technological gap still separes this region from the rest of the electromagnetic spectrum. In particular, the lack of room-temperature sources and detectors makes high-precision frequency measurements of molecular transitions an open challenge. Although recent technologies (as frequency multipliers, photo-mixers and quantum-cascade-lasers) already provided accurate frequency measurements on different molecular transitions in the lower part of the THz spectrum (<4 THz), the only continuous-wave (CW) sources spanning the whole Terahertz window dates back to the mid 80s years, being represented by the Tunable Far-Infrared Lasers (TuFir) approach based on difference frequency generation (DFG). In those years, CW THz radiation produced by nonlinear mixing of two CO_2 lasers emission was successfuly used to perform high resolution spectroscopy up to 9 THz. However, the low reliability and very low emitted powers of that very bulky instrumentation, hampered for decades its widespread use.

On the other hand, the tremendous progressess meanwhile achieved in the optical telecomunication field, have made available plenty of nonlinear integrated optical devices, as well as robust, compact and powerfull infrared laser soucres. This has created the conditions to imagine a novel family of DFG-based THz emitters, being able to compete with the precisions achieved by the most modern THz emitters and capable for spectroscopic measurement in the whole THz spectral window.

The work described in the present dissertation just regards the building from scratch of a room-temperature CW THz spectrometer and its application to high precision spectroscopy in the 1-7.3 THz range. The followed experimental stategy, based on DFG in a lithium niobate (LN) waveguide, allowed us to transfer to the THz frequencies the spectral purity and the tunability which characterize of the most mature technologies in the infrared part of the electromagnetic spectrum. Furthermore, thanks to the surface emission geometry allowed by the non-collinear Cherenkov phase-matching scheme, the absorption losses, usually limiting the available THz power in the common nonlinear generation setups, have been minimized enough to allow both room-temperature detection and high-precision spectroscopy.

The first two chapters of this thesis will be devoted to a more comprehensive discussion of the considered issues and to the foundamantal physical ideas at the basis of our experimental work. In the third chapter, a detailed technical descriptions of the accomplished experimental apparatus will be given, while in the fourth chapter the characteristics of the generated CW radiation and its usage in high-resolution molecular spectoscopy will be described. Finally, in the fifth chapter, the optical and the electronic setup for the frequency stabilization of the THz emission will be presented, as well as the ultimate precision of few parts in 10^{-9} achieved in spectroscopic measurements.

Before to start, I would like personally thank all the pepole I've worked with at the Italian Institute of Optics (CNR-INO) in Florence and, particularly, Dr. Luigi Consolino and Dr. Saverio Bartalini, without whom this work would not be possible.

1

State of the art and motivations

1.1 The ”terahertz gap”

The milestone paper ”On physical lines of force”, written by James Clerk Maxwell in 1861, is rigtly considered the second great unification theory in the history of Physics, after the Newton’s law on universal gravitation. Indeed, just as Newton guessed that the same force ruling the falling of bodies on earth was also responsible for the planets motion, Maxwell’s work has built a bridge between light and electromagnetism, revealing the two phenomena as parts of the same physical being. Thus, more than 150 years later, it is a fairly undisputed fact that both radio-waves and visible light, micro-waves and X-rays are electromagnetic waves having different frequencies. Anyway, despite the fact that Maxwell theory provide a rigorous description of any classical electromagnetic phenomena, regardless to the considered band, not all of them experienced the same technological development. In particular the terahertz (THz) spectral window, usually considered as the $(1-10)\cdot 10^{12}\ Hz$ frequency range, still suffers a serious lack of suitable devices, regarding to high-power, broadly tunable sources as well to fast room temperature detectors. As suggested by C. Sirtori in the occasion of the invention of THz quantum cascade laser[1], the THz range represent a watershed between the low frequency region of the electromagnetic spectrum, lying in the domain of electronics, and the purely optical domain [1]. Now, if the latter is dominated by the laser technology and transistor is the king device regarding to the former, a foggy scenario still characterize the THz window, so far as to deserve for it the name ”THz gap” (see figure 1.1).

By the way, plenty of practical and scientific applications of the THz radiation justify the increasing amount of experimental efforts carried out in the last few decades by the

---

[1] A detailed description of such a device will be given in the following of this chapter.

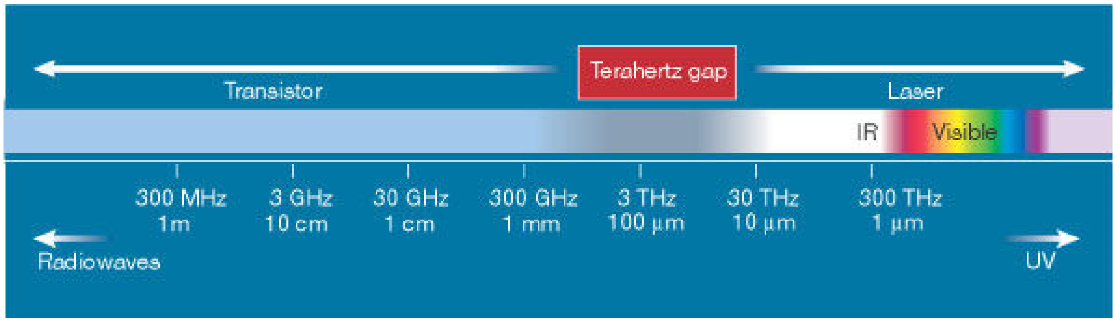

Figure 1.1: The terahertz window positioned within the electromagnetic spectrum. Figure reprinted from [1].

THz community. Many of these application deal with THz imaging, that can be implemented both with pulsed [2] and continuous-wave (CW) [3] sources. The low energy THz photons possesses the uncommon property to strongly interact with water, as well as to pass unabsorbed through plenty of polymers and textiles. For this reason they could in principle be used as non-ionizing probes for medical diagnosis [4]-[6], packaging inspection [7], body scanners or plant physiology [8]. For instance, in the pulsed regime, THz imaging has been demonstrated to be able to distinguish between epidermis cancer and harmless skin irregularities [5]. Unfortunately, due to the relatively poor brightness of almost all the currently available THz sources and, hence, to the extremely long times required in order to scan a typical sample, THz imaging systems are difficulty finding their place among the every-day-use devices. Such long scan times may not compromise all those applications in which just one sample or, as in many industrial productions, many nominally identical replicas of a single item have to be investigated. THz imaging in transmission geometry and THz tomography (in reflection geometry) have been demonstrate to be capable, for example, for luggage inspection [9]. Anyway, the scanning time, in the order of several tens of minutes, suggest such techniques to be employed only as a supplement to X-rays scanners, providing further details about objects treated as suspicious.

The most reliable technique to be adopted for applications is certainly the THz spectroscopy. Time domain spectroscopy (TDS), accomplished using pulsed sources, is the basis of many practical uses of THz radiation. For example, such a technique has been demonstrated to be useful in detecting contaminants as stones, plastic particles or eggshell in food. Indeed, since many eatables as sugar, wheat flour and chocolate have low water content and are transparent to THz pulses, unwanted contaminations can be distinguished by analyzing the shape of their temporal profile [10]-[11].

Increasing interest in THz technology has been demonstrated in the last few years also by plastic, leather and paper industry. Homogeneity of manufactured samples, as well as the critical temperature of polymers glass transition, can be determed by monitoring the refractive index at the THz wavelengths[12]-[14]. These latter mentioned works have been realized by exploiting pulsed THz sources, but frequency spectroscopy performed with CW radiation would be equally suited to these purpose.

CW sources, which are the main subject of this PhD thesis, play a central role in high-resolution THz spectroscopy and frequency metrology, representing a key tool for many applications. Indeed, in many cases the chemical composition of gas mixtures of very practical interest can be retreived by observing only a limited part of their absorption (or emission) spectrum. Under such circumstances, the considered spectral window constitutes a molecular fingerprint region. Generally, several parameters, as momentum of inertia or temperature, have to be taken into account in order to determine the frequency range in which the molecular signature can be easily identified. For example, because of their small momentim of inertia, at room-temperature, the rotational spectrum of light molecules, such as symmetric rotors like hydrogen halides [15]-[17] or asymmetric rotors like water or hydrogen sulfide [18]-[21], have their maximum in the THz range. Temperature also has a considerable impact on the linestrength. At low frequencies (i.e. $h\nu << k_B T$) temperature affects the spectrum only by the absorption/emission factor, scaling as $1/T$. Oppositelly, at higher frequencies the absorption profile is dominated by the Boltzmann distribution, implying an exponential decay in the population of states and making THz spectroscopy particularly suited in order to investigate molecular systems at low temperatures. Surely, one of the most notable example in this sense is the study of the interstallar medium and molecular clouds, for which THz technology has recently drawn attention of the astronomy community. Novel physical insight are expected from spectrospically based Far-infrared systems such as ALMA [22], SOFIA and Hershel, not only about star formation and evolution, but also about about ions and unstable species (not easy to produce in a laboratory) and large-prebiotic molecules [23].

Another intresting application regards the measurement of the composition of the earth atmosphere. Identification of the molecular species constituing the atmosphere and their relative amounts are usually performed by Fourier transform spectrometers mounted on stratospheric balloon platforms. Such measurements are of great importance since they provide the basic information needed to develop models able to predict atmospheric evolution as well as novel insight about fundamental chemical processes involved in global warming mechanisms [24]. For example, a proper knowledge of hydrogen peroxide (H_2O_2) concentration (and its dependence on altitude) is crucial for understanding the

HO_x catalitic cycle responsible for the ozone depletion. Such a concentration has been retrieved by observing the rotation-tortion spectrum characterizing the THz thermal emisson in the upper stratosphere. At the same time, disposing of laboratory data to be used as a reference for in situ measurements is a prerequisite for this and other spectroscopic applications, as plasma fusion diagnostic [25] or drug identification. All these applications require an accurate database of line positions and shapes. This, added to the fact that, in this spectral region, typical natural linewidths are in the order of a few hertz, motivates the increasing experimental efforts devoted to the accomplishment of narrow-line tunable THz sources.

Beside the practical implications so far described, more fundamental research could be eligible for metrological-grade THz emitters. In facts, most of the pysical details considered in the most recent molecular models, such as Zeeman shift, AC-Stark shift or blackbody shift, cannot be observed with the state of the art THz spectrometers, due to their limited precision and accuracy. Indeed, in order to appreciate the energy contribution expected for all these effects, frequency measurements with an absolute accuracy of at least 10^{-11} are required. Since spectral accuracy provided by the currently available THz spectrometers is limited to few parts in 10^{-9} [26], a technological gap still has to be bridged by supplementary efforts. If that wasn't enough, an uniqe possibility for THz metrology to leave its footprint on nature understanding seems to come from the rising field of cold molecules pysics. Indeed, despite the most accurate frequency measurements so far peformed have been achieved on atomic samples, with relative accuracy in the order of 10^{-18} [27], molecular systems seems to be more appropriate to answer fudamental questions usually considered to be matter for high-energy pysics. Cold molecules experiments has been proposed, for istsance, in order to investigate the time evolution of the fine-structure constant [28]. Once again, this can be done by comparing astronomical data with laboratory measurements, in this case regarding the $OH - \Lambda$ doublet microwave transition. The employment of cold molecular samples allowed to overcome the main experimental obstacle, consisting in the limited observation time arising from a poor center of mass motion control, providing the 100 Hz accuracy needed in order to compare laboratory data with the ones acquired from the astrophysical OH megamasers [29]. Another appealing application regards the measurement of a possible non-zero electric dipole moment of electrons, which is expected to confirm or deny the amount of CP violation predicted by recent theories going beynd the standard model. Remarkable results have been achieved in experiments based on cold molecular samples as YbF and ThO [30]-[31] as them exhibit, respect to the heavy atoms commonly used, larger polarizability and internal electric field. Further applications of laser spectroscopy of cold molecules includes tests of parity violation in chiral molecules [32]-[33], quantum-

electrodynamical shift of molecular energy levels [34] and spectroscopic measurement of the Boltzmann constant [35].
The choice of an optimal spectral region in which to carry on spectroscopy on cold molecules is still matter of debate. Microwave domain seems to be one of the most suitable ones because some important transition lying in this range are insensitive to the magnetic fields, implying considerable advantages, such as an easier comparison with the astrophysical spectra. Furthermore, Doppler broadening, being proportional to the radiation frequency has a less dramatic effect in this range. On the other side, the recent development of narrow-line, tunable and bright mid-IR sources, such as the quantum cascade lasers (QCLs), gave a significative boost to molecular ro-vibrational spectroscopy. Also thanks to the optical frequency combs (OFCs) technology, providing a bridge between the mid-IR and the microwave cesium frequency standard, many sub-Doppler absolute frequency measurements have been performed in this range, being the relative accuracy of such a measurements naturally enhanched as higher frequencies are involved. To the best of our knowledge, no attempts to bring toghether THz and cold molecular technology has been specifically proposed to date. Anyway, THz spectroscopy of cold molecules, not only can provide an estimated improvement of about two order of magnitude in relative accuracy respect to room-temperature THz spectroscopy [36], but also a dramatic increase in the precision with respect to the microwave range. Moreover, since coherent THz radiation represents a natural candidate in order to investigate and coherently control the rotational states of the cooled samples, CW THz sources are destined to play an important role in the future development of this research field.

The main goal of the present work was that of accomplish a CW source of coherent THz radiation, covering a frequency range as broad as possible and able to compete with the existing ones in terms of spectroscopic capabilities. To this purpose, the ideal device should fullfill several requirements, ranging from an acceptable output power level (possibily sufficient for room temperature detection) to a wide mode-hop-free tunability range, from an extensive coverage of the portion of the 1-10 THz spectral range and to a narrow-line emission profile. Furthermore, to be suitable for the scientific applications just described, a modern THz spectrometer cannot be saparated from an absolute frequency reference which gives it metrological features. It is a matter of fact that all these properties can hardly be combined in a single device and some compromise has to be reached. For example, THz QCLs provide considerable power levels (usually in the mW range) and acceptable mode-hop-free tunability but, regarding to the single device, the tuning range is limited to few GHz around the central emission frequency. Moreover, the higher frequency ever emitted by a CW THz QCL is 4.5 THz. On the opposite front, up to 9 THz have been achieved with tunable far infrared lasers (TuFIR) but with power levels limited to ten of nW. The following of this chapter is just devoted to a brief overview of the different CW THz sources so far developed, many of which already provided excellent results in specctroscopic measurements.

1.2 CW THz sources: state of the art

A detailed picture of the scenario in which this work has to be included, with particular emphasis to the historical element, has recently given by L. Consolino et al. [36]. Taking a cue from that work, in the following pages the whole family of the existing CW THz emitters will be divided in three groups: devices based on direct lasing action, devices based on frequency up-convertion (in practice, frequency multipliers) and devices based on frequency down-conversion. THz radiation obtained by technques related to the nonlinear optics domain will be excluded to this overview. Since this argument constitutes the backbone of the present work, it will be discussed in detail in the next chapter. Despite this section will be focused on relatively compact and potentially transportable sources, we owe to mention the family of far-IR emitters based on free electron acceleration such as backward wave oscillators (BWOs) and free-electron lasers (FELs). In a BWO an electron beam is collimated by a magnetic field and accelerated by a static electric field, the latter being periodically perturbated by the field produced by a metal grating. Such a perturbation induces the electrons to distribute in bunches and coherently transfer their own energy to an electromagnetic wave propagating in the opposite direction on the grating surface. In this way, tunable THz radiation can be achieved by adjusting the frequency of the generated wave, which is related to the electrons velocity. BWOs have been demonstrated to be capable for providing narrow-linewidth ($< 20\ kHz$) THz emission in the $0.03 - 1.2\ THz$ range, with output power up to $100\ mW$ below $0.2\ THz$ and in the milliwatt range around $1\ THz$ [100 libro]. Regarding to the tunability range provided by such a technique, it is of about the 10% of the emitted frequency. Furthermore, these sources have been used to perform sub-Doppler spectroscopy of rotational transitions of CO in the low frequency part of the THz spectrum [38]-[39]. Other sources of pseudo-CW THz radiation are represented by the FELs. In a FEL a relativistic electron beam is subjected to an alternating magnetic field inducing sinusoidal oscillation in the electrons motion. As a consequence, monochromatic waves are irradiated in a range that can span from microwaves to X-rays. Parameters influencing the emitted frequency are the intensity and the spatial period of the alternating magnetic field and the energy of the electron beam. Differently from the laser devices as such, in which coherent light amplification occurs thanks to the population inversion established between a material sample levels, in FELs amplification is achieved by synchronizing the radiation field and the electron oscillations. Furthermore, since in similar apparatus the electronic oscillation generating the radiation occur in vacuum, and hence no intrinsic limitation exist in the power to be held, these accelerators are able to produce partucularly intense emissions (up to the kW range), tunable along the whole THz band. On the other hand, the high costs and the large dimensions, due to the several tens of meters required in order to accelerate the electrons, make these devices much less pervasive respect to the optics-based THz sources. THz FEL facilities are currently open in the US (FIRE-FLY and FIR-FEL), Japan (iFEL) and Europe (FELIX in Netherlands, CLIO in France and FELIBE in Germany). It is worth to mention, for completness, that in the early 1990s the first compact FEL has been realized at the ENEA laboratories (in Frascati, Italy) and applied for for byological studies and cultural heritage diagnosis [40].

Direct lasing devices

Historically, the first example of table-top CW THz sources has been represented by the optically pumped far-infrared lasers (FIR). The development of such a technology dates back to the early 70s years, when, in the seminal work of Chang et al. [41], population inversion between rotational states of optically pumped methyl-fluoride gas (CH_3F) was demonstrated. Different infrared (IR) sources are potentially suitable as a pump for the active medium. Anyway, being the molecular absorption bandwidth centered around 10 μm wavelength, the radiation provided by CO_2 lasers the most used to this purpose. The pumping radiation induces an optical transitions between the fundamental vibrational level to the many rotational sublevels (spaced by few THz each others) composing the first excited state. Acting on the length of the laser cavity, a continuous frequency adjustment can be obtained accordingly with the molecular gain curve. By the way, such an energy structure implies severe limitations on the FIR lasers tunability as only a discrete wavelengths ensemble can be involved in the THz emisson process. Indeed, if on one hand the latter one can be broadened increasing the gas pressure, on the other side it implies a dramatic reduction both of the intensity of the emitted radiation and on its coherence time. Despite of this intrinsic drawback, the FIR technology plays to date a primary role in the framework of the currently available THz sources. Indeed, after the first experimental demonstraton in 1970, different molecular species as, for example, formic acid ($HCOOH$), methanol (CH_3OH), difluoromethane (CH_2F_2) and methyl-iodite (CH_3I), have been exploited as active medium, leading to impressive results in terms of spectral coverage and output power level. In particular, methanol based FIR lasers may take advantage of more than 300 rotational transitions, leading to emission lines distributed along the whole THz spectral window and whose intensity is sufficient to be employed in sectroscopic aplications. In some cases, for example the line at 2.52 THz, output power levels exceeding 100 mW have been recorded [42]. Furhtermore, many other emission lines can be added to the spectral content of these devices by employing as active medium different isotopic species as, in the case of methanol, CH_3OD, CH_2DOH or CHD_2OH. After more than 40 years, FIR lasers are still considered an usefull tool by part of the THz community and remarkable technological improvements have been reported until the present days. For instance, intresting works recently published demonstrate the possibility to enhance the optical gain by exploiting a novel technique based on a zig-zag pumping geometry [43]. In this way $CHOOH$ or CH_2F based FIR with output power in the milliwatt range have been realized, providing an effective tool for high-precision spectroscopy in the 0.17-2.24 THz spectral range. Despite this fact, in the last few decades, the interest respect to the bulky FIR setups has progressively fallen in favour to more compact devices, in particular the THz quantum cascade lasers (QCLs).

Proposed in the 70s by the pionieristic work of R. F. Kazarinov et al. [44] this semiconductor based devices have been experimentally realized for the first time in 1994 by J. Faist and F. Capasso in the mid-IR [45] and, in 2002, in the THz spectral window thanks to the work of Tredicucci et al. [46]. Although QCLs fall under the category of semiconductor lasers, they differ substantially by the usual emitting diodes in which the light is produced as a consequence of the recombination between conduction electrons and holes lying in the valence band. Regardless of the emitted wavelength, a QCL is a periodic heterostructure constituted by an array of quantum wells (QW). Each period, whose length is tipically about $50 - 60\ \mu m$, is composed by an active layer, whose optical thickness is in the order of the conduction electrons De Broglie wavelength, and an injection region. In this latter structure the energy characterizing the conduction band is considerably higher respect to the active region that, for this reason, acts as a deep potential well for the charge carriers. For example, in the first mid-IR QCLs the active region was constituted by AlInAs, while the injection barrier was composed by GaInAs, providing a number of charge carriers ranging from few tens to more than one hundred. The most peculiar feature distinguishing the QCLs from the usual p-n junction lies in the fact that the valence band is not involved at all in the emission process. Oppositelly, the 2-dimensional heterostructure add to the conduction band, naturally present in the material, several sublevels that will be the ones involved in the population inversion process. Referring to the layer plane as xy and indicating as z the direction of the carrier injection,

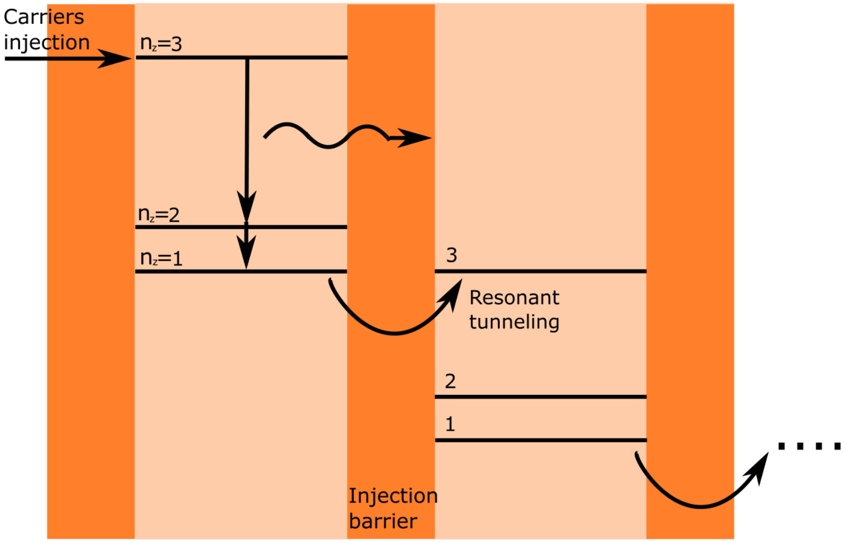

Figure 1.2: Schematic illustration of lasing and cascading in a QCL heterostructure.

the sublevel energies can be labeled by an integer number n_z and expressed as

$$E(n_z) = \frac{\hbar^2\pi^2 n_z^2}{2m_e^* L^2} \tag{1.1}$$

where m_e^* is the effective mass of the conduction electrons and L is the thickness of the active region. Adjusting this latter parameter the device can be taylored in order to provide emission in the mid-IR and in the THz frequency range, usually unavailable with the common semiconductor lasers. Moreover, the flat density of states g_E, emerging as a consequence of the $d = 2$ dimensionality of the structure ($g_E \propto E^{d/2-1}$), leads to more symetric and narrow lineshape.

Referring to figure (1.1), the lasing action can be described as follow. Three sub-bands, at the energies $E_3 > E_2 > E_1$, describes identically the electronic structure of each QW, while a bias voltage can be applied along the z direction in order to allign the E_1 level of a certain QW with the E_3 level of the following one. Once an electron current J is injected in the E_3 level of the first QW, the carriers are distributed in a continuum of quasi-plane wave states described by the quantum number $k_{\parallel}^2 = k_x^2 + k_y^2$ and the condition for the population inversion are established. Indeed, the high momentum $k_{\parallel}$ to be transferred in order to achieve the 3 → 2 transition and the weak overlap of the relative wavefunctions makes the lifetime of this process to be in the order of $5 - 10$ ps. In order to minimize the relaxaton time associated to the 2 → 1 transition, and therefore allow the population inversion, the E_1 level can be taylored so that the gap $E_2 - E_1$ coincide with the optical phonon energy, whose emission tipically occurs on a 0.1 ps time scale. Finally, the electrons so decayed in the lower energy sub-band are diffused through the injection barrier to the E_3 state of the subsequent QW by resonant tunneling, triggering the cascading effect.

Regarding specifically the THz QCLs, since their first experimental demonstration to date several heterostructures, as for example InGaAs/AlInAs [47], InGaAs/GaAsSb [48] or InGaAs/AlInGaAs [49] have been designd in order to increase the emitted power and functioning temperature. Indeed, one of the main drawbacks affecting the THz QCLs is the need of a cryogenic cooling, emerging as a direct consequence of the low THz photons energy. Being the latter one comparable to optical phonon energy in the active region, contrary to what happens in the mid-IR QCLs, without an appropriate cooling, electron-electron scattering mediated by phonon exchange would be the dominant relaxation process, actually hampering the lasing action. Significant progress toward the accomplishment of high-temperature THz QCLs have been achieved by the resonant-phonon three-well design, proposed by Luo et al. in 2007 [50] or exploiting high transferred momentum transitions (also known as diagonal transitions) in order to inhibit the relaxation channels, expecially below 3.5 THz. On this regards, remarkable results have been already achieved in the pulsed regime, where emission around 3.22 THz at about 200 K has beed experimentally demonstrated in 2012 [51]. These big step forward augurs well for the accomplishment, even in the CW regime, of devices able to operate beyond 240 K for which, hence, cryogenic liquids employment could be substituted by thermo-electric cooling.

Optical medium typology and the light confinament mechanism play a funamental role even in determining the available output power levels. On this regard, until 2005 THz QCLs based on bound-to-bound active region design stil held the record [52]. In such devices the laser cavity containing the active region was constituted by a metal-metal waveguide, providing an optimal light confinement but limiting the intensity of the emitted radiation. By the way, just one year later, a novel configuration based on Si-surface-plasmon waveguides was proposed, leading to CW THz emission with optical power 136 μW at 4.47 THz and operating at 10 K of heat-sink temperature [53]-[54].

Another technological challenge has been represented by the attemts to accomplish THz QCLs having as wide mode-hop-free tunability range as possible. In order to accomodate this necessity, promising results have been obtained with the distribuite-feedback (DFB) QCLs, fistly designed in the mid-IR spectral region and then extended to the THz window. Such devices are implemented by spatially modulating the waveguide profile, providing single mode operation with continuous tunability achieved by adjusting the injection cur-

rent, the temperature or taking advantage by an external cavity grating. Anyway, despite the brilliant results obtained in the mid-IR, with continuous tunability range in the order of 25% of the emitted frequency, in the THz window, being the wavelength comparable with the output facet size, only few tens of GHz around the emitted frequency can be covered with this approach. In the last few years, considerable improvements have been obtained adopting a novel wire-shaped design. In such wire-QCLs up to 330 GHz mode-hop-free frequency scans have been performed manipulating the transverse profile of the guided mode [55]-[56].
The non trivial goal to obtain coherent THz radiation by direct lasing action can be circumvented by nonlinearly converting to the THz frequencies radiation of shorter or longer wavelength. In the next paragraph we will discuss the case of frequency multipliers, in which electromagnetic radiation in the GHz range is frequency up-converted to the THz range.

THz radiation by frequency multiplication

A frequency multiplier can be schematically described by an antenna that receives a CW microwave signal (in the 10-100 GHz range) and transfers it, by a waveguide, to a nonlinear device capable for generating higher-order harmonics. Generally, the microwave signal is produced by an oscillating circuit containing, as a key feature, a gunn-diode. The voltage-to current relation characterizing a gunn diode presents negative slope regions to be exploited in order to counterbalance the impedance of the oscillator that, hence, produces an attenuation-free CW signal. In almost all the cases, the nonlinear element responsible for the frequency up-conversion is represented by a Shottky diode. Respect to the standard p-n junctios, this latter device is distinguished by the fact that the depletion region is realized depositing a metallic layer on top of a semiconductor wafer and, for these reason, results to be utterly devoid of any charge carrier. As a consequence, typical commutation times of these devices are in the order of 100 ps and the nonlinearities, generated by the microwave signal rectification, reach up to the third harmonic.
Using whisker-contacted-Shottky-diodes, the most diffused devices until the mid-1990s, the THz spectral coverage was limited to the millimeter wavelength region. This limitation was due to conversion-efficiency saturation introduced by the finite maximum carrier speed in the GaAs substrate. Being the conversion efficiency an increasing function of the microwave frequency, this saturation effect hampered effectively the achievement of frequencies larger than 100 GHz. In 1993, B. J. Rizzi et al. showed how, implementing a novel planar design, several diodes (lets say n) could be wired in series leading to an amplification of the imput power scaling as n^2. Thanks to this approach, doubler devices

was buit covering up to 174 GHz and emitting about 55 mW output power [57]. This result, accompained by the birth of novel modelling approaches, pulled the trigger on a period of constant technological advances leading to optimized nonlineadr structures and contacts, particularly regarding the impedance matching between the waveguides and the diodes [58]. The final result has been the accomplishment of more cascaded multiplication stages up to reach, in 2005, emitters covering up to 1.75 THz with output power levels in the order of 100 μW [59] and, in 2011, frequency multipliers with about 15 μW in the 2.48-2.75 THz range [60].

THz radiation by frequecy down-conversion

A mirror-approach respect to the just described one, consists in nonlinearly down-converting infrared or visible radiation into the THz range, i.e. achieving coherent emission by mixing two CW optical fields differing in frequency just for few THz. For the time being, we will leave out from this overview the optical processes taking advantage from the second order susceptibility in dielectric materials. Being these latter ones the physical foundation of all this experimental work, they deserve a more comprehensive discussion, that will be carried out in the following of this chapter. In both the two technique we are going to describe in this paragraph, the nonlinear process occurs in semiconductor structure, i.e. the MIM diodes in the case of tunable FIR and photo-conductive antennas. As we already seen talking about the FIR lasers, these devices had their bigger limitation in the tunability range, necessarily entailing serious problems for spectroscopic applications. In order to overcome these limitation, tunable far-infrared spectrometers (TuFIR) have been developed since the late 70s years [61]-[62]. In its early years, this approach basically consisted in adding to the FIR molecular laser line microwave sidebands by nonlinear mixing in a Shottky diode. Oppositelly to the THz central frequency, whose value is fixed by the specific molecular transition, the microwave radiation could be continuously adjusted as it was produced by a resonant klistron oscillator, in which an electron beams was accelerated by a radio-frequency signal. On this basis, several improvements have been achieved during the 80s thanks, in particular, to the work of K. M. Evenson. In 1984, he and co-workers accomplished a difference frequency generation setup by mixing on a metal-insulator-metal (MIM) diode the radiation emitted by two CO_2 lasers, whose frequencies, differing of 0.57 THz or 3.5 THz depending on the used transitions, were stabilized on two CO_2 saturated-absorption lines [63]. The desired tunability was accomplished by mixing one of the two lasers, before to focalize it on the MIM diode, with a radio frequency signal whose frequency could be adjusted in the

0-150 MHz range. Adopting this strategy, the generated THz frequency was given by

$$\nu_{TuFIR} = \nu_{FIR} \pm 150\ MHz, \tag{1.2}$$

being $\nu_{FIR} = \nu_1 - \nu_2$ the one provided by the difference frequency generation process. This benchmark was enanched just a few years later by Nolt et al. with the experimental demonstration of third order TuFIR lasers [64]. Such devices distinguished from the previously descripted ones as the adjustable sidebands were added to the THz radiation by directly mixing the radio frequency signal on the MIM diode. This three-wave-mixing process leaded to THz emission with power in the hundreds of nW level and tunable over a range of 40 GHz around several fixed THz frequencies, from 0.3 THz up to 6 THz. The upper limit in the THz spectrum, due to the larger difference frequency available between the two CO_2 lasers, was overcomed by substituting one of these with an ammonia-laser. Since NH_3 molecule posses several lines at lower frequenciy respect to CO_2, difference frequencies are possible in order to cover the whole THz spectral window (i.e. up to about 10 THz). Thanks to this significative improvement, continuously tunable THz radiation with demonstrated capability for high precision spectroscopy, was generated in 1994 up to 7.9 THz [65] and in 1999, after a proper optimization of the pumping mechanism for the ammonia laser, radiation above 9 THz was obtained [66]. For many years, MIM diodes and TuFIR constituted the reference point for metrological grade THz experiments and, regarding the 5-10 THz range, remained so until the present days. Despite of this fact, more recent sources based on frequency down-conversion have been concieved, providing results of absolute importance in spectroscopy. In these source, commonly called THz photomixing synthesizers or optical-heterodyne-downconverter, the THz radiation is directly emitted from a semiconductor antenna structure, triggered by a photo-conductive (PC) switch.

A PC antenna is a compact solid state device, consisting of two metal layers deposited on a semiconductor bulk, in which CW THz radiation can be produced by photomixing. Two optical laser beams, spectrally separed by the desired THz frequency, are focalized within the semiconductor substrate producing, by interference, a temporarily modulated intensity profile. A static field accelerates the electron-hole pairs generated by light absorption. In such a way, the intensity profile coherently drives a photocurrent that oscillates in time at the difference frequency $\nu_{THz} = \nu_1 - \nu_2$. Typically, the semiconductor bulk is constituted by a semi-insulating (SI) GaAs substrate on which a low-temperature-grown (LTG) GaAs layer is deposited. A metallic antenna (usually in a logarithmic uniplanar spiral geometry) is attached on top of this layer while, in order to extract the generated THz radiation, a silicon hyper-hemispherical lens is placed on the back side of the substrate.

The main asset of photomixing techniques lies in the broad tuning range provided by the dual-frequency pump lasers. For its part, the log-spiral antenna with interdigitatated electrode fingers [67] doesn't introduce any limitation in the continuous tunability range that, in practice, coincided with the mode-hop-free operational band of the optical sources. Several factors contribute to limit the spectral coverage of these sources, including the input impedance of the metallic structure, its radiation pattern, the low radiation resistance related the thermal conductivity of the substrate and, particularly, the finite carriers mobility and lifetime. Regarding to this latter one, the time constant of log-spiral geometry and the carrier lifetime of LTG-GaAs, in the order of few hundreds femtoseconds, ensure a flat conversion efficiency in the order of $10^{-6} - 10^{-5}$ and outputpower in the microwatt range in the $0.1 - 1\ THz$ spectral window. Beyond 1 THz the output power scales as ν_{THz}^{-4}. The generation bandwidth can be extended up to 2 THz exploiting a resonant antenna structure on a GaAs substrate, characterized by an higher power resistance and having a resonant frequency at about 1.8 THz for a 50 μm dipole [68]-[69]. Since the output power is proportional to the antenna resistance, in a single-dipole configuration, a power enanchement can only be accomplished by increasing the antenna impedance and optimizing the power transfer between the photomixer and the antenna by a proper impedance matching. In particular this latter is not a trivial issue, as the THz conductivity of the photomixer is very low (typically $< 10\ k\Omega^{-1}$) [70]. An alternative strategy consists in exploiting a different dual-dipole design in which, if on one side the input resistance is reduced in half, on the other hand the inductive tuning compensates the the electrode capacitance eliminating the consequent roll-off frequency. In such devices operation up to 2.7 THz have been demonstrated with output power of about 0.3 μW [71]. Remarkabily the remaining limitation, being due to the finite carrier lifetime, leads to a frequency profile scaling as ν_{THz}^{-2} instead of ν_{THz}^{-4} as it was for the log-spiral antenna output. Further room for improvement have been showed removing the photocurrent limitation due to the low threshold for thermal damage of LT-GaAs. This can be implemented by replacing the former material with different nonlinear elements such as p-i-n photodiodes.

2

Physical background

As we have seen in the previous chapter, many nonlinear devices used in order to achieve THz generation by frequency up- and down-conversion are based on semiconductor technology. The finite carrier lifetime of such materials translates into severe limitations in the available THz spectrum, specially regarding the high frequency range. Anyway, plenty of dielectric crystals, exhibiting strong optical nonlinearities, are commonly employed in THz generation setups. In such materials, the mechanism by which an optical field is converted to the THz range does not involve any charge to be transferred to the conduction band. THz emission can rather be seen as the result of an anharmonic response of the bounded electrons to an exciting beam. This fundamental difference implies not only that no intrinsic limitation in the spectral coverage are expected, but also that the material is able to handle larger amount of exciting power because of the lower absorption. Of course, also the generation techniques based on nonlinear crystals are not immune from some drawbacks. The price to be paid is a conversion efficiency tipically lower than in semiconductor materials[1] and the difficulties in ensuring a coherent energy transfer between spectral regions as distant as the optical and the THz range are. In other words, this last statement can be resumed as the necessity to fullfill a phase-matching condition. In this chapter we will give a brief description of the physics which underpins our experimental approach: a non-collinear waveguided phase matching. In particular, we will try to make it clear the considerable advantages that can be expected by this scheme in terms of spectral coverage, nonlinear efficiency and tunability.

---

[1] Actually, this statement is partially ambiguous. Indeed, as we will see, in the second order processes the fraction of the optical power that is converted to the THz range is proportional to the incoming intensity. Anyway, even in the case of the present work, in which a considerable conversion efficiency has been reached by confining the optical power into a waveguide, the transferred energy ratio is order of magnitudes lower than in a photomixer.

2.1 Nonlinear Optics

The study of the light-matter interactions moves from the fact that an electromagnetic waves passing trought a dielectric material induces a polarization wich, in turns, acts as a source of new optical fields. The mathematical relation between the optical dergees of freedom, that for a non-magnetic media are the electric field $\mathbf{E}(\mathbf{r}, t)$, the magnetic field $\mathbf{H}(\mathbf{r}, t)$ and the polarization vector $\mathbf{P}(\mathbf{r}, t)$, is given by the set of Maxwell's equations[2]:

$$\nabla \cdot (\varepsilon_0 \mathbf{E} + \mathbf{P}) = 0 \tag{2.1a}$$

$$\nabla \cdot (\mu_0 \mathbf{H}) = 0 \tag{2.1b}$$

$$\nabla \wedge \mathbf{E} = -\mu_0 \frac{\partial \mathbf{H}}{\partial t} \tag{2.1c}$$

$$\nabla \wedge \mathbf{H} = \varepsilon_0 \frac{\partial \mathbf{E}}{\partial t} + \frac{\partial \mathbf{P}}{\partial t} \tag{2.1d}$$

where ε_0 and μ_0 are respectively the dielectric constant and the magnetic permeability of vacuum. From a physical point of view, the vector $\mathbf{P}(\mathbf{r}, t)$ must be interpreted as the ensemble average of the electrical dipole moments induced by the field in a small region of the material centred around $\mathbf{r}$, and it is therefore a function of $\mathbf{E}$.

Until the early 1960s, i.e. until the advent of the laser sources allowed to obtain intense and coherent optical fields, most of the optical fenomena could be described assuming for the system a linear response to the electromagnetic excitation. In other words the polarization vector could be taken in the form $\mathbf{P} = \mathbf{P}^{(L)} = \varepsilon_0 \chi \mathbf{E}$, where χ represents the dielectrical susceptibility of the material. In this framework, being χ independent of the exciting intensity, the medium will not bring any modification to the spectral content of the outcoming fields. In 1961 P.A. Franken and co-workers observed, for the first time, a frequency doubling process occurring in a quartz crystal pumped by a ruby laser beam [72]. It was the first experimental realization of second harmonic generation, and it marked the beginning of nonlinear optics: the study of those phenomena for which the linear approximation doesn't hold. The stricter way to approach the nonlinear optical processes is based on the quantum treatment of both the medium and the electromagnetic fields. Nevertheless, for our purposes the formal complexity of such description is not required and, in order to get the results we shall need, a semiclassical treatment will be sufficient. The use of quantum electrodynamics will be limited to the few cases in which

---

[2] Here the SI units system is adopted and is assumed the absence of localized charges ($\rho = 0$) and currents ($\mathbf{J} = 0$).

it could help an easier visualization of the underlying physics.
As a first step, we will find an expression for the macroscopic polarization in the form $\mathbf{P}(t) = \mathbf{P}^L + \mathbf{P}^{NL}$, with

$$P_i^{(L)} = \varepsilon_0 \sum_j \int dt_1 \chi_{ij}^{(1)}(t - t_1) E_j(t_1) \tag{2.2}$$

and

$$P_i^{(NL)} = \varepsilon_0 \sum_{j,k} \iint dt_1 dt_2 \chi_{ijk}^{(2)}(t - t_1, t - t_2) E_j(t_1) E_k(t_2) + \tag{2.3}$$

$$\varepsilon_0 \sum_{j,k,l} \iiint dt_1 dt_2 dt_3 \chi_{ijkl}^{(3)}(t - t_1, t - t_2, t - t_3) E_j(t_1) E_k(t_2) E_l(t_3) + \cdots \tag{2.4}$$

The terms $\chi^{(n)}$ encodes the informations regarding both the material response and, reflected in their tensorial structure, the geometrical arrangiement of the particles comprising it. In many cases, the computational efforts needed for the optical susceptibility determination, generally requiring non trivial quantum mechanical calculation, are dramatically reduced once some structural simmetry is known. Common examples are represented by omogeneous systems (as liquids or gases) and centrosymmetric crystals, for wich the second order susceptibility $\chi^{(2)}$ identically vanishes.
In the following, we will restrict our attention to the second order process, taking advantage of the frequency domain description. Since in many practical situations the overall electric field can be seen as a superposition of (quasi) monochromatic waves (laser beams), it can be conveniently expressed as

$$\mathbf{E}(\mathbf{r}, t) = \frac{1}{2} \sum_m \mathbf{e}_m E_m(\mathbf{r}, \omega_m) exp[i(\mathbf{k}_m \cdot \mathbf{r} - \omega_m t)] + c.c. \tag{2.5}$$

Where $\mathbf{e}_m$ is an unitary vector expressing the polarization of the m-th wave and the wave vector $\mathbf{k}_m$ is related to the angular frequency ω_m and the refractive index n by $k_m = \omega_m n(\omega_m)/c$. An analogous expression can be found for the polarization vector. When the overall incoming optical field oscillates at two frequencies ω_1 and ω_2 one could see that, while in the linear term the Fourier components have to be evaluated at the same frequencies of the exciting beams, finding

$$P_i^{(L)}(\mathbf{r},t) = \frac{1}{2}\sum_{m=1,2}\chi_{ij}^{(1)} e_m^j E_m(\mathbf{r},\omega_m) exp[i(\mathbf{k}_m \cdot \mathbf{r} - \omega_m t)] + c.c. \tag{2.6}$$

new spectral features arise from $\mathbf{P}^{(2)}$. Indeed, the nonlinear polarization field oscillates at the frequencies $\omega_3 = \omega_1 + \omega_2$ (sum frequency generation SFG), $\omega_3 = \omega_1 - \omega_2$ (difference frequency generation DFG), $\omega_3 = 2\omega_1, 2\omega_2$ (second harmonic generation SHG) and $\omega_3 = 0$ (optical rectification OR). For SFG and DFG processes, of whom SHG and OR are subsets, the Fourier transform of $\mathbf{P}^{(2)}(t)$ results to be:

$$P_i^{(2)}(\omega_3) = \frac{\varepsilon_0 D}{2}\sum_{jk}\chi_{ijk}^{(2)}(-\omega_3;\omega_1,\omega_2)E_j(\omega_1)E_k(\omega_2) \quad (SFG) \tag{2.7a}$$

$$P_i^{(2)}(\omega_3) = \frac{\varepsilon_0 D}{2}\sum_{jk}\chi_{ijk}^{(2)}(-\omega_3;\omega_1,-\omega_2)E_j(\omega_1)E_k^*(\omega_2) \quad (DFG) \tag{2.7b}$$

where we have defined a degeneracy coefficient to be $D = 1$ if $\omega_1 \neq \omega_2$ and $D = 2$ if $\omega_1 = \omega_2$. Note that, respect to the reciprocal interactions i.e., for a SFG process, $\omega_3 = \omega_1 + \omega_2$, $\omega_1 = \omega_3 - \omega_2$ and $\omega_2 = \omega_3 - \omega_1$, the second order susceptibility tensor exhibits the following permutation simmetry:

$$\chi_{ijk}^{(2)}(-\omega_3;\omega_1,\omega_2) = \chi_{jki}^{(2)}(-\omega_1;-\omega_2,\omega_3) = \chi_{kij}^{(2)}(-\omega_2;\omega_3,-\omega_1) \tag{2.8}$$

reflecting, from a physical point of view, the same photon conversion efficiency for the reciprocal processes. Moreover, in many practical cases, the optical fields lie in spectral regions far from the medium resonances. Under these assumptions $\chi^{(2)}$ results to be independent of the frequency, turning this into a relation between different elements of the same tensor (Kleinman symmetry) [73]. In all of these cases the 27 elements of the second order susceptibility tensor are reduced to only 10 independent ones.

At this point, before to definitively join the smiclassical approach and pursue the Maxwell equation solution, a brief mention to a schematic description of SFG and DFG processes from a quantum mechanical point of view is useful. Differently from linear optical processes, as absorption and stimulated emission, in which a resonant interaction occurs between the field and the material, the concept of virtual transition is of fundamental importance for nonlinear optics. Here are involved transition from ultra-short

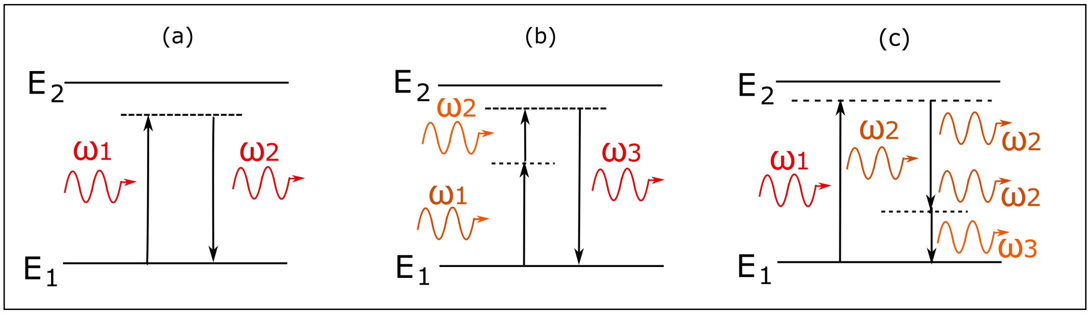

Figure 2.1: Virtual transitions in a two-energy-level system: a) transmission, b) sum frequency generation and c) difference frequency generation.

lifetime virtual levels for which the density of states is zero. This kind of interactios can lead both to linear and nonlinear phenomena. An example for the linear case is given by transmission (figure (2.1 a)). In this case the virtual transition plays a fundamental role reducing the light speed in the medium even when the photon energy is far from the resonance ($\hbar\omega_1 < E_2 - E_1$ in the example). The interaction bring the system to a state not corresponding to any energy eigenvalue and from here it decays back to the lower state. The short but finite lifetime of the virtual state imply the light slowing down. When SFG or DFG (see figure (2.1 b) and (2.1 c)) occurs, there are two involved short lifetime levels, reducing the cross-section of the process. For this reason the rate of frequency up- and down- conversion becames non-negligible only for intense photon fluxes. It is also noteworthy that, in the DFG case, the arrival of the second photon at frequency ω_2 ($< \omega_1$) induces a partial decay to a second virtual level placed exactly at $\hbar\omega_2$ below the upper one, leading to the emission of a further photon at the same frequency, in the same way as in the stimulated emission between real energy eigenstates. The process is thus completed when the system finally relaxes to the foundamental level E_1 and the net result is a new field at frequency $\omega_3 = \omega_1 - \omega_2$ accompained by the (parametric) amplification of the ω_2 field. In the current language of nonlinear optics the waves at frequencies ω_1, ω_2 and ω_3 are respectively called pump, signal and idler.

Now let us to come back to the semiclassical picture. From the Maxwell equations it follows that each of the three just defined fields must obey to a wave equation that, in the frequency domain, is

$$\nabla^2 E(\mathbf{r}, \omega) + \frac{\omega^2 n^2(\omega)}{c} E(\mathbf{r}, \omega) = -\mu_0 \omega^2 P^{(2)}(\omega) \tag{2.9}$$

where we have made the symplifying assumption that no free charges are present in the

dielectric material. The refractive index has been defined by the relation $n^2 = \varepsilon_0 \sum_{ij} e_i(\delta_{ij} + \chi^{(1)}_{ij})e_j$, in order to take into account of the anisotropic structure characterizing the nonlinear crystal.
For a first analysis, it could be usefull to limit our study to the situation of three copropagating fields in the plane wave approximation picture. This consists in the assumption that the spatial dependence of the field amplitudes is restricted to the propagation direction (x). Furthermore, often one might assume the fields amplitude does not vary appreciably within one wavelength (slow-varying-envelope approximation) i.e.

$$\frac{dE(x)}{dx} \cdot k >> \frac{d^2E(x)}{dx^2}. \tag{2.10}$$

Under these assumption, the coupled wave equations are for a SFG process ($\omega_3 = \omega_1 + \omega_2$)

$$\frac{dE_1}{dx} = -i\frac{\omega_1 d_{eff}}{n_1 c}E_2^* E_3 exp(-i\Delta kx) \tag{2.11a}$$
$$\frac{dE_2}{dx} = -i\frac{\omega_2 d_{eff}}{n_2 c}E_1^* E_3 exp(-i\Delta kx) \tag{2.11b}$$
$$\frac{dE_3}{dx} = -i\frac{\omega_3 d_{eff}}{n_3 c}E_1 E_2 exp(i\Delta kx) \tag{2.11c}$$

where $\Delta k = k_3 - k_2 - k_1$ represents the phase mismatch and d_{eff} is the effective nonlinear coefficient defined by $d_{eff} = 1/2 \sum_{ijk} e_3^i \chi^{(2)}_{ijk} e_1^j e_2^k$.
In a similar way, the coupled wave equations for a DFG process ($\omega_3 = \omega_1 - \omega_2$) are:

$$\frac{dE_1}{dx} = -i\frac{\omega_1 d_{eff}}{n_1 c}E_2 E_3 exp(i\Delta kx) \tag{2.12a}$$
$$\frac{dE_2}{dx} = -i\frac{\omega_2 d_{eff}}{n_2 c}E_1 E_3^* exp(-i\Delta kx) \tag{2.12b}$$
$$\frac{dE_3}{dx} = -i\frac{\omega_3 d_{eff}}{n_3 c}E_1 E_2^* exp(-i\Delta kx). \tag{2.12c}$$

This time the phase mismatch is $\Delta k = k_1 - k_2 - k_3$. When the conversion efficiency is sufficiently low, variations in the input fields amplitudes can be neglected and the previous equation can be easily integrated along the propagation direction. The obtained result is the same for both SFG and DFG processes:

$$|E_3(x)|^2 = \left(\frac{\omega_3 d_{eff}}{n_3 c}\right)^2 |E_1|^2 |E_2|^2 x^2 \left(\frac{sin(\Delta kx/2)}{\Delta kx/2}\right)^2 \tag{2.13}$$

. Integrating the intensity $I_3 = 2\varepsilon_0 n_3 c|E_3|^2$ over the transverse incoming beams interaction area $\mathcal{A}$ and defining the adimensional parameter $\xi = x/L$, where L is the total crystal length, the conversion efficiency can be written as

$$\eta = \frac{P_3}{P_1 P_2} = \eta_{norm}\xi^2 \left(\frac{sin(\Delta k L\xi/2)}{\Delta k L\xi/2}\right)^2 \tag{2.14}$$

where

$$\eta_{norm} = \frac{2d_{eff}^2 \omega_3^2 L^2}{\mathcal{A} n_1 n_2 n_3 \varepsilon_0 c^3}. \tag{2.15}$$

This latter expression clearly shows that a tight focusing of the pump and signal beams, as well as an high optical non-linearity of the medium (resulting in an high value for d_{eff}), are essential requirements for the efficiency of any frequency -up and -down conversion process. At first sight, it could also seems that even the crystal length L has to be maximised for this purpose. Nevertheless, this is true only when the perfect phase matching condition ($\Delta k = 0$) is achieved. Otherwise, the finite phase mismatch implies that, as the fields penetrate in the material, the three coupled waves become more and more dephased, until an efficient energy transfer from the pump and signal fields to the idler one is no more possible. As it is shown in figure (2.2), this happens when the fields penetrate a specific thickness within the medium, called coherence length and given by $L_{coh} = 2\pi/\Delta k$. As an example, figure (2.2 a) shows how the phase matching condition (PM) affects the generation efficiency in three different cases. The red solid curve represents the case in which a perfect PM is achieved: the frequency conversion occurs along the whole crystal that, in this case, has to be as long as possible. The other two dashed curves show that, when the coherence length is finite (even if bigger than L), the frequency conversion rate dramatically drops as a small fraction of the total length has been passed through by the pumping light.

In the last fifty years, many different techniques have been developed to obtain collinear PM. Among of them, birefringent PM and quasi-PM in periodically poled nonlinear crystal plays a dominant role both for SFG and DFG processes. By the way, since only DFG is suitable for THz generation, we will abandone the parallelism between this two processes and, in the following, we will focus on the frequency down-conversion.

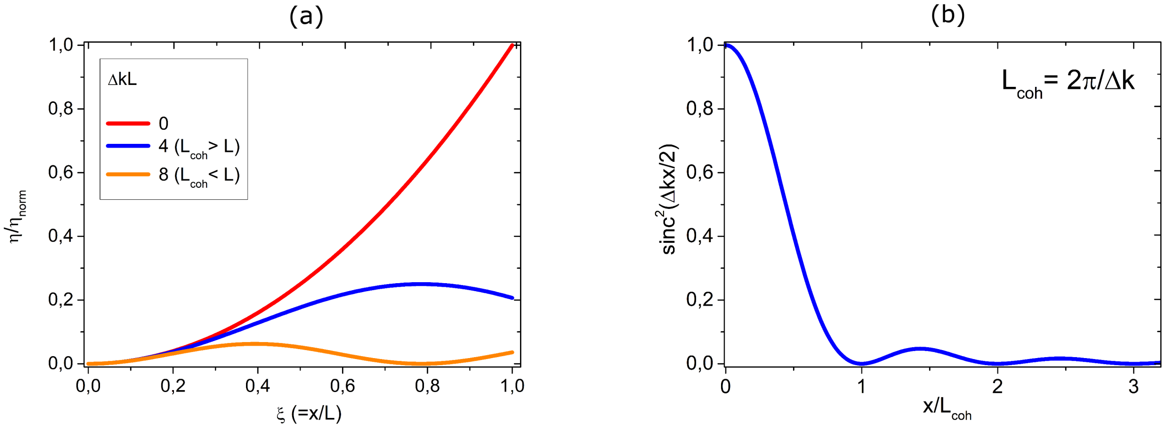

Figure 2.2: a) Second order conversion efficiency as a function of the (normalized) interaction length for different values of the phase mismatch. b) Normalized detuning curve. Here the coherence length is defined as the propagation depth for which the coherent energy transfer totally quit.

2.1.1 Collinear phase matching for THz DFG

We have seen in the previous section that the THz field undergoes coherent amplification only when a perfect PM is achieved, i.e. when $n(\omega_1)\omega_1 - n(\omega_2)\omega_2 = n(\omega_3)\omega 3$. In order to obtain collinear PM, one of the most suitable techniques is to exploit materials that are birefringent, as well as nonlinear. In a birefringent medium the refractive index depends on the angle that the fields form with a spcific direction inside the crystal, called extraordinary axis. The fields with a polarization parallel to this axis will propagates with velocity c/n_e, while the orthogonally polarized ones with velocity c/n_o. Here n_o and n_e are respectively the ordinary and the extraordinary refractive indexes of the material. In all the intermediate conditions, when the field has both a component lying in the ordinary plane and another one alligned with the extraordinary axis, the refractive index can be expressed as a function of of the angle θ formed by the propagation direction and the optical axis:

$$\frac{1}{n^2(\theta)} = \frac{sin^2\theta}{n_e^2} + \frac{cos^2\theta}{n_o^2}. \tag{2.16}$$

Thanks to this feature, the collinear PM can be fulfilled adjusting the fields polarization in order to maximise the nonlinear effect, and tilting the crystal accordingly to the desired frequency to be generated (angle tuning). In some cases, as for lithium niobate, the refractive index is strongly temperature dependent and the birefringent PM can be achieved also controlling the crystal temperature (temperature tuning). Notable examples of birefringent materials employed for nonlinear generation of THz radiation are Quartz, Lithium Niobate (LN), Gallium Selenide (GaSe) and 4-dimethylamino-N-methyl-4-stilbazolium-tosylate (DAST). Anyway, the most suitable choice for this kind of PM is represented by GaSe, a negative uniaxial crystal ($n_e < n_o$) leading to very large nonlinear response when the pump and the signal fields are mutually orthogonal. For instance, in this case the three waves $E_y(\omega_1)$, $E_x(\omega_2)$ and $E_x(\omega_T)$ are coupled by the component $d_{eff} = \frac{1}{2}\chi_{211}$ being in the order of $54pm/V$, while the extraordinary axis lies in the 13 plane, forming an angle θ with the propagation direction. In this case the PM condition is given by $n_T(\theta)\omega_T = n_o\omega_1 - n_2(\theta)\omega_2$ and, as demonstrated in [74], can lead to a THz output ranging from 0.2 to $5.3THz$.

Sometimes, to maximally exploit the nonlinear optical properties of certain materials, a parallel arrangiament of the three involved polarizations is required. This is the case of LN, for which the $d_{eff} = \frac{1}{2}\chi_{333}$ component of the second order susceptibility tensor, being in the order of $33pm/V$, largely exceed the other ones. Under these circumstances, a collinear approach consisting in achieve the PM in a periodically-poled lithium niobate crystal (PPLN) has demonstrated to be usfull. In a PPLN the sign of the second order susceptibility tensor is periodically inverted with a spatial period Λ along the propagation direction. The resulting modulation in the function $d_{eff}(x)$ leads to a modified expression for the phase mismatch term in the form

$$\Delta k = k_1 - k_2 - k_T + \frac{2\pi m}{\Lambda} \tag{2.17}$$

where m is an integer number. Thus, the crystal design can be optimized for the desired THz frequency choosing Λ to be equal to an integer multiple of the coherence length. In order to achieve THz power in the microwatt range, in many cases the PPLN crystals has been employed as active medium in optical parametric oscillators (OPO). An OPO can be realized placing the nonlinear material within an optical cavity, generally in a bow-tie geometry, resonant at the frequency of the signal or of the THz wave (providing singly-resonant OPO) or at both of the frequencies (leading to a doubly-resonant OPO). When the gain parameter g, that in case of perfect PM is given by

$$g = \frac{2\omega_T\omega_2 d_{eff} E_1}{\sqrt{k_T k_2}c^2}, \tag{2.18}$$

overcomes the cavity losses, the idler and/or signal fields replicates themselfes every round-trip L and provide two coherent output beams. The threshold condition that has to be fulfilled to trigger the parametric oscillation is

$$cosh(gL) = 1 + \frac{l_2 l_T}{2 - l_2 - l_T} \tag{2.19}$$

being $l_i = 1 - R_i exp(-\alpha_i L)$ with R_i and α_i respectively the reflectivity and the absorption coefficient at ω_i.
In 2009 R. Sowade et al. demonstrated that THz emission in the microwatt range can be achieved exploiting a cascaded singly resonant OPO process [75]. In that work, a 1030 nm pump beam generated a primary resonant signal field working as a pump for the THz generation in a PPNL crystal. The poling period and the resonator length uniquely selected both the primary signal frequency and the (secondary) THz one. Thanks to the self-adaptive optical scheme, similar setups do not require the resonator to be externally stabilized. Is also noteworthy that, in this configuration, to fullfill the quasi-PM condition, the THz wave must counterpropagate respect to the pump and signal fields. The spectral coverage, here restricted to the range $1.3 - 1.7 THz$, has been improved few years later thanks to a different scheme in which, adjusting the cavity length, the pump power was increased up to reach THz generation in a single nonlinear process. With such a strategy J. Kiessling et al. obtained up to 3.9 μW of THz power tunable from 1.4 to 2.9 THz, the tuning mechanism consisting in varying the temperature of the crystal, a PPLN with a poling period of $29.5 \mu m$ [76]. Further improvements have been obtained in 2013 implementing the doubly-resonant OPO strategy [77] in which two nonlinear crystals, pumped with two nearly resonant beams close to 2 μm, were placed in different focal points inside the same resonant cavity. A first PPLN crystal worked as active medium for the signal wave amplification while for the THz generation an oriented-pattern gallium arsenide (OP-GaAs) were used. With this approach the intracavity power reach the 100 W level, corresponding to THz power levels in the order of tens of μW obtained at different frequencies within the $1 - 4.5$ THz spectral range.
Lately, collinear intracavity THz DFG processes have been implemented in a novel tipology of THz QCLs [78]. Regarding to the heterostructure growth and fabrication, a THz DFG-QCL does not differ much from a standard mid-IR one, basically consisting in a dual-wavelength mid-IR QCL in which DFG occurs by taking advantage of the active region second order susceptibility. Notably, since no population inversion is required to be established across a THz transition, THz DFG-QCLs are able to operate at room temperature. As well as any the semiconductor-based device, the pump beams intensity and the coherence length are limited by the free carrier absorption, reducing the generation efficiency. On the other side, such a disavantage can be compensated by tailoring the heterostructure in order to increase its optical nonlinearities. Indeed, by a proper en-

geneering, the energy sublevels responsible for the lasing action can be adjusted so as to bring the emitted mid-IR frequencies to be resonant with the second order nonlinear process. This strategy has been demonstrated to be usefull in enhancing the nonlinear performances of THz QCLs based on bound-to-bound and dual upper state active region design, which in itself possess strong optical nonlinearities. Second order susceptibility in the order of $10^4 pm/V$, have been obtained in both the cases. Output power in the order of hundreds of nanowatt have been obtained from THz DFG-QCLs based on bound-to-bound design operating at room temperature and capable for THz emission in the microwatt range below 250 K [79]. More recently, microwatt level room temperature emissions have been acheved in 1-3 THz range exploiting the dual upper state active region design [80].

2.2 THz surface emission: waveguided-Cherenkov phase matching

In the previous section, the most exploited collinear PM techniques have been desctribed. Anyway, all of them present some common drawbacks. On one side, the quasi-PM bandwidth and the resonant cavity used in OPOs, the birefringent dispertion relations in GaSe and the free carrier absorption in DFG-QCLs limit the coherence length of the process and/or the continuous tunability range of the source. On the other hand, the nonlinear materials commonly employed usually possess high values for the absorption coefficient in the THz spectral range, reducing the amount of generated THz power available for the applications. For these reasons, in the present experimental work we chose to follow a different non-collinear approach made possible by the unique optical features of LN.
In order to describe the physics underlying our strategy, let us first come back to the PM condition for a DFG process, considered this time in its most general vectorial form

$$\Delta \mathbf{k} = \mathbf{k}_1 - \mathbf{k}_2 - \mathbf{k}_T, \tag{2.20}$$

and let us assume that, as it is in the real case, both the pump and the signal fields are two IR laser beams, co-propagating in the x direction along the crystal length. At the opposite, regarding to the generated THz field, we will assume that it could propagate in an arbitrary direction. We will indicate as θ the angle that the wavevector $\mathbf{k}_T$ forms with the x axis. Since in LN the absorbption losses in the IR wavelength range are negligible, once again we can integrate the three wave coupled equations (2.12) in the non-depleting-pump approximation, i.e. considering the amplitude of the fields E_1 and E_2 depending on the transversal coordinates y and z, but not on the propagation direction. The integration along the crystal length L provides

$$E_T = \frac{\omega_T d_{eff} E_1 E_2^* L}{n_T c\ cos\theta} exp[i(k_T^y y + k_T^z z)] sinc\left[\frac{L}{2}(k_1 - k_2 - k_T cos\theta)\right] \tag{2.21}$$

where an unimportant global phase factor has been omitted for semplicity. In this case, is worth to write the PM condition in the form

$$\frac{L\ \omega_T}{2c}(n_{IR} - n_T cos\theta) = 0, \tag{2.22}$$

in which we have neglected the IR dispersion for frequencies ω_1 and ω_2, differing for few THz. As one can immediatelly see, such a requirement can be exactly fulfilled for those materials in which the IR light propagates faster than the THz waves. Indeed, when $n_{IR} < n_T$ a conical THz wavefront, defined by the relation

$$\theta_C = arccos\left(\frac{n_{IR}}{n_T}\right), \tag{2.23}$$

is coherently generated along the whole crystal length. The angle θ_C formed by the THz wavevector and the x axis is called Cherenkov angle, because of the close analogy with other physical phenomena such as shock waves in fluids and, of course, Cherenkov emission by ultra-relativistic particles. In figure (2.3 a) a schematic representation of the process is shown. The Cherenkov angle can be interpreted as the propagation direction for which wave fronts generated at different points along the nonlinear medium constructively interfere each other. The geometrical construction clearly shows that this circumstance could't occur if the center of the wavefront would be contained within the circumference representing the wavefront previously generated, i.e. if $n_{IR} > n_T$.

LN and other ferroelectric crystals, such as lithium tantalate ($LiTaO_3$), possesses the desired property. Anyway LN represents the optimal choice for those applications exploiting telecom radiation (i.e. IR radiation at about 1.55 μm wavelength) as pump fields. LN has about 2.2 refractive index around $\lambda = 1.55\mu m$ and about 5.2 in the THz window, leading to Cherenkov angles of barely varying around 65 degrees[3]. If this angle overcome the critical value given, accordingly with the Snell law, by the difference of the refractive index at the crystal interface, the THz wave is completely reflected inside the crystal. Since this circumstance is verified at the interface between any nonlinear material and

---

[3] A more accurate extimation of θ_C, based on the available dispersion relation provided by the Sellmeier equations, will be given further in this work .

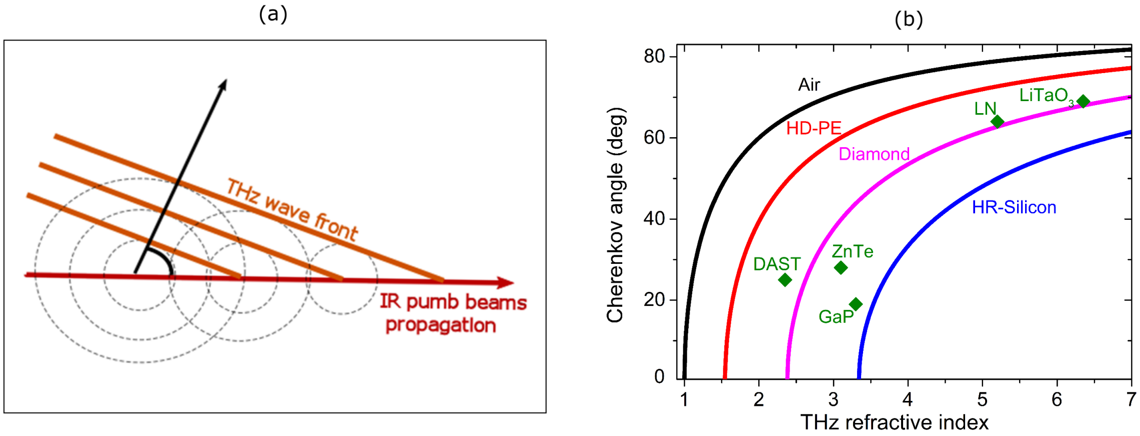

Figure 2.3: a) Wave-like picture for the Cherenkov Phase matching. Spherical wavefronts generated at different times along the pump propagation direction can be in phase only if the point-like source propagates in the medium faster than the generated THz wave, i.e. if $n_{IR} < n_T$. b) The green diamonds represent the Cherenkov emission angle for different nonlinear materials, supposed to be pumped at 1.55 μm. Solid lines represents crytical angle for different cladding materials. Points lying below a specific solid curve correspond to THz radiation undergoing total internal reflection.

air, a cladding material with a proper prism shape is needed in order to extract the generated radiation. In figure (2.3 b) Cherenkov angles corresponding to different nonlinear materials have been reported (dark green squares) as a function of their refractive index at the THz frequencies. Solid lines instead represent, for different cladding materials, the maximum emission angle for which can be possible to extract the produced radiation. For example THz waves produced in LN can be extracted by high-resistivity silicon (HR-Si) or diamond prism but not by high-density polyethylene (HD-PE). THz radiation produced in GaP or in $ZnTe$ can only be extracted by a HR-Si prism, while in it would be totally internally reflected at the interface, for example, with diamond.

From a practical point of view, the non-collinear approach based on Cherenkov PM, resulting in an infinite coherence length, entails the experimental need to keep the IR pump beams collimated along the whole crystal length. This means that the waist w_0 of a gaussian laser beam, whose wavelength lies in the telecom range, must be of about 47 μm in order to produce a Rayleigh length[4] $z_R = 1cm$ or, for instance, a waist of 82 μm to reach $z_R = 3cm$. On the other hand, we have previously seen that increasing the interacting area

---

[4] Here, accordingly with the common nomenclature, the waist of a gaussian beam is defined as dhe diameter of the intensity profile at the $1/e^2$ level, and the Rayleigh length as the distance, measured from the waist, within which the laser beam diverges less than a factor $\sqrt{2}$. The two geometrical parameters are related by $z_R = \pi n\, w_0^2/\lambda_0$, where λ_0 is the wavelength in vacuum.

implies a worsening of the generation efficiency. Moreover, even in a non-collinear emission scheme, a non negligible fraction of the produced THz radiation can be absorbed by the material if the thickness to be crossed is in the order of hundreds of μm. Now we aim to show that a waveguide approach leads not only to overcome these problems, but also to extend the range of the available THz frequencies.

In order to keep the IR beams collimated and, at the same time, overlapped on a small interaction area, the most suitable choice is to match the light with the fundamental mode of a tiny nonlinear waveguide. Furthermore, if this waveguide lies just beneath the surface of the substrate in which it is implanted, the generated THz radiation can be immediately extracted and the absorption losses can be minimized.

An optical waveguide is a physical device in which the electromagnetic radiation can propagate being confined in the transversal dimensions thanks to a proper distribution of the refractive index, generally constant along the propagation direction. The simplest guiding geometry is the slab waveguide, consisting in a dielectric layer (the guiding film), having a thickness in the order if the light wavelength, enclosed between two semi-infinite bounding media (claddings) having a smaller refractive index. Said xz the plane containing the waveguide plane, the light is confined in the orthogonal direction y thanks to the total internal reflection at the edges of the guiding film. For the boundary conditions imposed by such a configuration, the Maxwell equations provide, for a certain wavelength, a discrete number of solutions [81]. These can be divided in transverse-electrical modes (TE), in which the electric field is polarized along the y direction and the magnetic field in the xz plane, and transverse-magnetic modes (TM), in which the opposite situation occurs. This modes, usually labeled by an integer number $m = 1, 2, 3..$ are caratterized by an effective refractive number n_{eff}, whose value, lying between the cladding and the guiding ones ($n_c < n_{eff} < n_g$), expresses the phase velocity of the field. Regarding the optical profile, it is constant along the propagation direction while in the y direction it shows exactly $(m - 1)$ zeroes.

From the nonlinear generation point of view, the utility of the planar geometry is limited by the impossibility to confine the light in the y direction. Anyway, since the divergence of the emitted THz beam increases reducing the generation area, the slab-waveguide approach potentially helps when the experimental conditions make to collect the radiation difficult. When the collection capability is not a problem and the medium is sufficiently resistant to the high optical intensity, the channel-waveguides are surely the most suitable alternative. In this kind of structures the light is confined both in the y and in the z directions and the order of the guided mode is labeled by a couple of integer numbers related to the number of zeroes of the field distribution in the transverse plane. The complex amplitudes E_i comparing in (2.21) can be expressed as $E_i = A_i \Phi_{m,n}(y, z)$, where the function

Φ provides the effective modal area accordingly to

$$\mathcal{A} = \iint \Phi^2_{m,n}(y,z)dydz \tag{2.24}$$

while A is related to the confined optical power by $P_i = 2\mathcal{A}\varepsilon_0 n_{eff} c|A_i|^2$. In the following we will assume for the guided IR fields a gaussian intensity profile, i.e. a field distribution in the form $\Phi(y,z) = exp[-(y^2/r^2_{0y} + z^2/r^2_{0z})]$, where r_0 represent the radius for which the intensity profile is reduced by a factor $1/e^2$ respect to the centre. Under these assumptions, the generation efficiency can be retrieved integrating the Pointyng vectorr associated to the THz field over the interaction area:

$$\eta = \frac{P_T}{P_1 P_2} = \eta_{norm} g(\omega_T, r_{0y}, r_{0z}) sinc^2\left[\frac{L\omega_T}{2c}(n_{eff} - n_T cos\theta)\right] \tag{2.25}$$

where

$$\eta_{norm} = \frac{L^2 d^2_{eff}}{\pi^2 n_T n^2_{eff} c^3 \varepsilon_0 r_{0y} r_{0z}} \tag{2.26}$$

and

$$g(\omega_T; r_{0y}, r_{0y}) = \omega^2_T exp(-\frac{1}{4}[(k^y_T r_{0y})^2 + (k^z_T r_{0z})^2]). \tag{2.27}$$

This latter term contains the information about the spectral coverage expected for a certain mode size. Indeed, considering for semplicity a cylindrical simmetry for the waveguide structure (i.e. $r_{0y} = r_{0z} = r_0$), the function g can be written in the the simple form $g(\omega_T, r_0) = \omega^2_T exp(-\omega^2_T/\omega^2_{ro})$, where the roll-off frequency ω_{ro} is defined as $\omega_{ro} = \frac{2c}{r_0}(n^2_T - n^2_{eff})^{-1/2}$. Now, while at the low frequencies the emission profile is dominated by a $g \propto \omega^2_T$ behaviour, a dramatic decreasing in the generated power has to be expected beyond the roll-off frequency. In figure (2.4 a) the g function has been plotted for different mode radii. As can be seen, a broadening of the achievable bandwidth and an high-frequency shift of the maximum available efficiency rapidly occurs once the mode size is reduced. For example, radiation beyond 4.5 THz, representing the current frequency limitation in CW THz QCLs, can hardly be obtained with mode dimensions exceeding 10 μm. Oppositelly, a beam radius smaller than $5-6$ μm should be sufficient, in principle, in order to achieve nonlinear generation along the whole THz bandwidth.

Physically, this fact can be interpreted both in terms of wave momentum conservation and interference. Referring to the Heisenberg uncertainty principle, the non-collinear

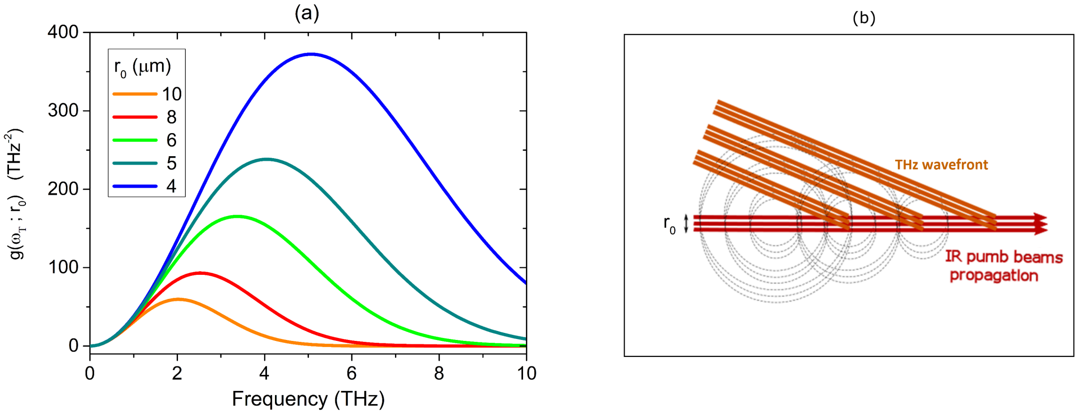

Figure 2.4: a) Accessible THz bandwidth for a CW waveguided DFG process in MgO:LN. Different lines correspond to different guided mode radius between 5 μm and 12 μm. Reducing the guided mode size implies to increase both the spectral coverage and the generation efficiency peak. This effect can be physically explained in the wave-like picture of part b). THz waves generated within a few microns depth (much smaller than the THz wavelength) undergoes constructive interference. Oppositelly, increasing the thickness of the generation volume, shorter wavelength waves will suffer destructive interference.

part of the phase mismatch Δk_{yz} can be compensated by an uncertainty of the wavevector $\Delta k \simeq 1/r_0$. The second way to look at this phenomena can be argued by looking at figure (2.4 b). As we have already seen, the achievement of Cherenkov PM can be seen as a process of constructive interference of spherical wavefronts, generated at different points along the pump beams propagation. Now, also the THz waves generated at different depth beneath the crystal surface will interfere each others. For this reason, when the distance between two wavefronts approach the THz wavelength, destructive interference occurs, while only generation depths much smaller than λ_T contribute to a coherent enhancement of the THz radiation intensity.

2.2.1 Optical rectification of ultrashort laser pulses

Although this work is focused primarily on the generation of CW THz radiation (and on its spectroscopic application), it is intresting to extend the discussion started in the previous section to the case of Cherenkov generation of THz pulses. From the theoretical point of view, this issue has been recently treated by J.A. L'Huillier et al. [82] on the basis of a linear antenna model, while the effectiveness of the waveguided approach in the pulsed regime has been experimentally investigated by K. Suizu et al. [83].

Regardless of the mathematical details (that will be described in the following), the easiest way to think at the physical principle on the basis of optical rectification (OR) is to consider a DFG process for each of the Fourier component which constitutes the starting optical pulse. Thus, the spectral content of the generated field will range from a DC component, i.e. at 0 Hz, up to the term resulting from the difference of the last and the first frequency components. The obtained wave will possess the same bandwidth of the starting one, being inversely proportional to this duration τ_p. As a consequence, if the duration of the optical pulse is in the order of $10 - 100fs$, a THz pulse will be produced. To look at this issue in a more rigorous way, we need to move away from the field description based on the monochromatic waves and consider a temporal profile having, for instance, a gaussian shape:

$$E(\mathbf{r}, t) = A\Phi(y, z)exp[-(t - x/u)^2/2\tau_p^2 + i\omega_c t] \tag{2.28}$$

in which ω_c is the carrier frequency and $u = \partial\omega/\partial k = c/n_g$ is the group velocity of the pulse. Note that here we have assumed that no dispersion of the pulse occurs during the propagation in the nonlinear medium. Regarding the spatial profile, we are assuming a gaussian-shaped guided mode, similarly to what we did in the CW case. This time it results more useful to express the parameter A as a function of the pulse energy U:

$$A = \sqrt{\frac{U}{\varepsilon_0 c\pi^{3/2}\tau_p n_g r_{0y} r_{0z}}}. \tag{2.29}$$

In many cases, the IR source used as a pump in OR experiments is a mode-locked laser emitting a train of pulses separed by a fixed time delay. The reciprocal of this delay is called repetition-rate ν_{rep} and, multiplied by U, provides the average power of the pulsed source, that is commonly measured with a power meter.

The calculation of the nonlinear efficiency can be carried out similarly to what we previously did. In this case, the Fourier transform of the field will be

$$E(\mathbf{r}, \omega) = \sqrt{2\pi}\tau_p A\Phi(y, z)exp[-(\omega_c - \omega)^2\tau_p^2/2 + i(\omega_c - \omega)x/u], \tag{2.30}$$

leading to a second order polarization, to be inserted in the wave equation, in the form

$$P^{(OR)}(\mathbf{r}; \omega) = \frac{4U\ d_{eff}}{\pi c\ n_g\ r_{0y} r_{0z}}\ \Phi^2(y, z)e^{-i\omega x/u}e^{-\tau_p^2\omega^2/4}. \tag{2.31}$$

As a consequence, the spectral coverage of a rectified THz pulse differs significantly

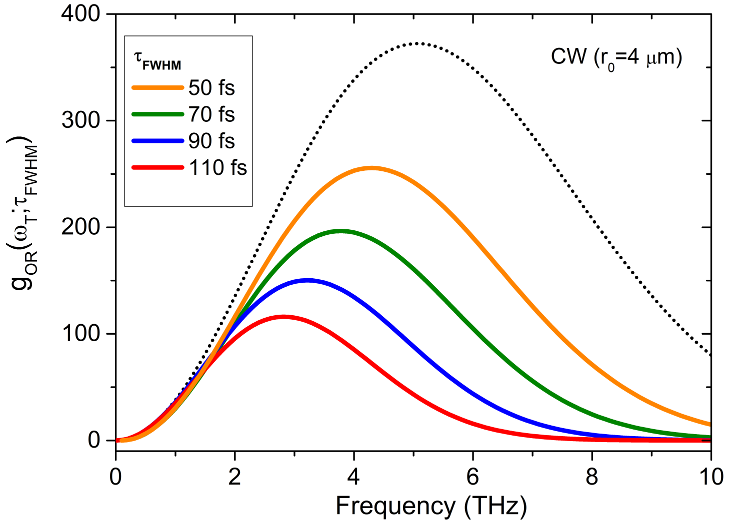

Figure 2.5: THz bandwidths achievable for different duration of an IR gaussian pulse, optically rectified in a LN channell waveguide of 5 μm radius. Dotted gray line represents the corresponding bandwidth for a DFG process in CW regime.

from that of a CW THz source. Indeed, the g function results to be modified in the form:

$$g_{OR}(\omega_T; r_{0y}, r_{0z}, \tau_p) = g_{CW}(\omega_T; r_{0y}, r_{0z})e^{-\tau_p^2\omega_T^2/2}. \tag{2.32}$$

In figure (2.5) different THz spectral bandwidths, achievable assuming a spot radius of 5 μm, have been plotted. The dotted line refers to the result to be expected for CW operation. Similarly to what happens increasing the mode radius, generation peak and coverage reduce as the pulse duration become longer. The solid lines in figure have been calculated for different values of the full width at half maximum ($\tau_{FWHM} = 2\sqrt{ln2}\tau_p$) of the intensity profile, being such a parameter the usually provided one by the lasers manufacturers. Note that, even considering an extremely small modal size, tipically to be accomplished by using a waveguiding structure, infrared pulses of less than 50 fs must be employed in order to get rectified pulses covering the whole THz spectral window.

Before to conclude this chapter we would like to recall that, since many years now, THz pulses obtained by OR have been largely used in time-domain spectroscopy (TDS) setups [84]. Under many aspects, such a technique is similar to the pump and probe spectroscopy. Indeed, as in the latter one, two pulses obtained dividing a starting one with a beam splittes are delayed one respect to the other and re-combined on a detector. The temporal shape of the pulse can be retreived as a function of the introduced delay and the spectral content is obtained by analyzing its Fourier transform. TDS simply consists in repeating this spectral measurement with and without the sample to be investigated. Furthermore, recently the pulsed OR-based THz sources has been emerged for their extraordinary usefulness in stabilizing and referencing other direct lasing emitters, mainly THz QCLs. This capability arises by their intrinsic comb nature, in a sense that will be explained soon. Basically an optical-frequency-comb (OFC) is constituted by a train of identical pulses, temporarly spaced by the same time $1/\nu_{rep}$, which in the frequency domain are represented by a discrete set of equally spaced frequencies (the comb structure). What distinguishes an OFC from a traditional mode-locked laser is the fact that the former covers, at least, an octave in the frequency domain. This latter feature is essential in the IR and visible part of the electromagnetic spectrum as, while the repetition rate ν_{rep}, determining the space between the teeth of the comb, can be controlled by a quartz oscillator stabilized by a Rb-GPS (global positioning system), an undetectable frequency offset ν_{off} hinders the precise knowledge of the n-th tooth frequency. This problem may be overcomed if the spectral coverage exceed the octave. In this case indeed, the spectral content includes the frequency pair $\nu_n = \nu_{off} + n\nu_{rep}$ and $\nu_{2n} = \nu_{off} + 2n\nu_{rep}$, so that ν_{off} can be measured and controlled duplicating in frequency (by a SHG process) the low part of the spectrum and superimposing it to the original one on a fast detector. The beating signal achieved in this way oscillates at the frequency [85]

$$\nu_{beat} = 2\nu_n - \nu_{2n} = \nu_{off}. \tag{2.33}$$

Once the frequency offset is known the OFC effectively works as a ruler for frequency metrology. This experimental trick is unnecessary in the case of rectified THz pulses, as the DFG process automatically cancels f_{off}. Despite the first demonstration of these comb-like features has been obtained with the photo-conductive-antenna based THz photomixers [86]-[87], in 2012 a THz comb realized by OR in the Cherenkov configuration, has been use to phase-lock a single frequency CW QCL at 2.5 THz [88]. In that work, a spectral coverage ranging fron few GHz up to more than 6 THz has been reported, demonstrating a remarkable improvement respect to the photomixer-based combs (limited to about 1.5 THz).

3

Experimental setup

In the previous chapter we carried out the theory of nonlinear optical processes, emphasizing how adopting a waveguided-Cherenkov PM approach many of the obstacles limiting the efficiency of THz generation can be circumvented. Among the other aspects, what makes this approach particularly suitable for the accomplishment of a source capable for high performances in spectroscopic applications, is the fact that the DFG allows to shift in the THz spectral range the optical features of the most mature laser technologies, available in the visible or in the IR region.
For this reason, the fundamental goal of our experimental efforts is to obtain a THz source showing the same spectral purity, tunability and high-resolution capabilities of the current IR spectrometers. It's worth hence to begin this chapter, focused on the description of the experimentl setup, describing the laser systems used.

3.1 Laser sources

Althought in principle the DFG process doesn't imply any restriction on the absolute frequencies of the pump and signal beams, all the light sources we chose to use in our setup emit in the region of the electromagnetic spectrum known as the telecom bandwidth. This is the spectral window in which the fiber-based devices used in telecommunications have their minimum transmission losses and small pulse broadening. Originally considered as the wavelength range going from 1260 nm to 1360 nm (O-band), nowadays the telecom bandwidth extends up to 1625 nm. Indeed the CL-band, ranging from 1530 nm to 1625 nm, has been demostrated to ensures optimal operations of many devices as ultra-long transmission lines, wavelength division multiplexers and Erbium-doped fiber amplifiers (EDFAs), of crucial importance in telecommunications technology. In particular, these latter devices represent a central tool even for the present experiment.

If this fact could be sufficient to justify the choice of the laser sources employed, another one affects our decision even in a more crucial way. Indeed, our long term goal is to give a metrological status to the designed source, making it capable for absolute frequency measurements in THz range. To this pourpose, when this setup has been conceved, we planned to entirely base our generation scheme on telecom laser sources, being these easily referable to the available frequency standard. Such ultra-stable and accurate reference signals are currently generated at the metrological institutes of many european countries, as PBT in Germany, LNE-SYRTE in France, NPL in the UK and AGH in Poland. In Italy, an ultra-stable signal (10^{-15} after 1 hour averaging) is provided by the Italian Institute for Metrological Research (INRIM), in Turin, and is distributed in many italian research institutes by an optical link (see figure 3.1), having an instability of 10^{-19}. This frequency reference, that is just at 194399.996 GHz ($\simeq$ 1542.14 nm) with an uncertainty $<$ 1 Hz, is already available at the European Institute for Nonlinear Spectroscopy (LENS) in Sesto Fiorentino and will be soon available in the THz laboratory of Italian Institute of Optics (INO-CNR) in Florence.

The telecom sources employed in the presented setup can be addressed to three different categories:

- the Erbium-doped fiber amplifiers (EDFAs), used to obtain the high-power CW IR radiation that will act as the pump and signal beams of the DFG process
- the tunable narrow-linewidth CW lasers, seeding the EDFAs
- the mode-locked laser, used both for testing the THz source performances in the pulsed regime and, more importantly, to improve its frequency stability in the CW mode.

The experimental characterization of all of these sources will be discussed in details in the following pages.

Seeding sources

The sources used as a seed for the fiber amplifiers are two commercial laser diodes (Toptica, model DL 100/pro) that, in the following, will be indicated as D1 and D2. They are based on a p-n junction emitting in a single mode and spanning the wavelength ranges from 1495 nm to 1605 nm (13.74 THz, D1) and from 1550 nm to 1650 nm (11.72 THz, D2). In the free-running mode, the diodes emit according to the modes of the 100μm long laser internal cavity, formed by the rear and the front facets of the diode. The free spectral range of this resonator is about 64 GHz and, in this condition, the linewidth of

Figure 3.1: Present day dissemination of the fiber link in Italy, in yellow the already working link, and in green the upcoming connections.

the laser, whose frequency can be tuned by adjusting the current and/or the diode temperature, results to be of the order of 100 MHz. In order to obtain a narrower emission, the ligth is filtered by an external cavity, realized by sending the diode output, properly collimated with a diffraction-limited lens, on a diffraction grating opertaing in the Littrow configuration. Again, the feedback light, i.e. the first diffraction order, is coupled by the lens with the internal cavity mode. Thus, the rear facet and the grating are going to form a high-finesse resonator with a length of few centimeters and a free-spectral-range smaller than the internal cavity one. Finally, a second collimating lens, and an optical isolator, couple the radiation with a single mode fiber, connected to the amplification stage.

In order to achieve a good spectral purity in the THz range, two narrow-line seeding sources are required. Indeed, thanks to the DFG approach, the linewidth of the generated radiation will be roughly twice the ones of the pump and signal fields. Furthermore, since in the THz spectral window many doppler-limited molecular transitions are only few tens of MHz broad, we must experimentally chek that the linewidth of the CW sources seeding our THz spectrometer does not exceed some hundreds of kHz. Since the typical resolution of the commonly available wavemeters is of the order of few GHz, we measured the laser diodes linewidth by implementing a basic heterodyne setup. To this purpose, the diode emission has been spatially overlaped to a femtosecond laser beam (described in details in the following) constituted, in the frequency domain, by a sequence of 100 MHz spaced ultra-narrow tooth. Once the pulsed and the CW fields are properly mixed on a fast photodiode (Thorlabs DET10C), a radio-frequency signal, arising from the beating of the laser diode emission with the nearest teeth, will be produced. Since the teeth can be assumed to be much narrower than the lineshape to be measured, the desired linewidth can be retrieved by observing the RF signal with a Fourier-transform spectrum analyzer (Tektronix RSA5106A). It is worth to stress out that the minimum measurable linewidth is limited by the acquisition time, that is the inverse of the resolution bandwidth (RBW). Indeed, unless the CW laser frequency is locked to a stable oscillator, any kind of mechanical or electrical noise leads to a frequency jitter, resulting in a line broadening that increases with the observation time. As an example, in figure (3.2 a) two beat-notes obtained for different acquisition times are shown, both of them being obtained by setting the laser diode D2 at a wavelength of 1605 nm. Here, the red trace, corresponding to a RBW of 1 kHz, shows the typical Lorentzian profile

$$S_{beat} = \frac{2}{\pi}\frac{\Gamma}{4\nu^2 + \Gamma^2}, \tag{3.1}$$

where Γ represents the full width at half maximum (FWHM). Conversely, the blue trace, obtained for a RBW of 10 Hz, cannot be described by a Lorentzian function as the

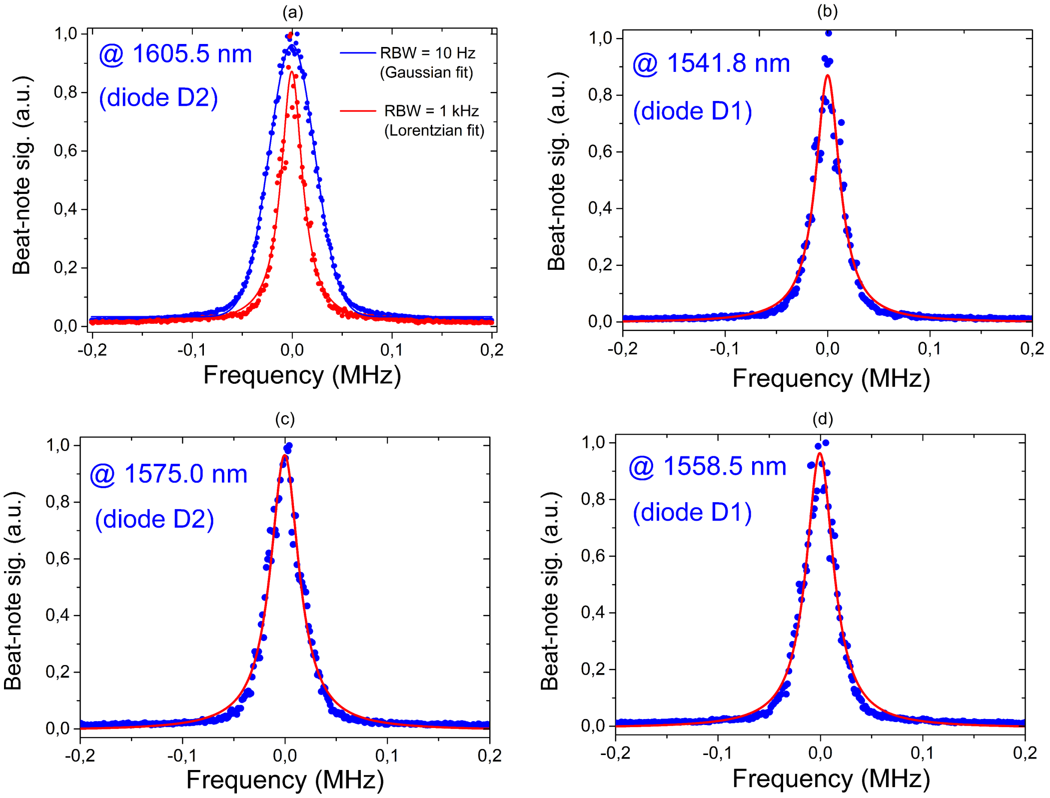

Figure 3.2: Measured line-shapes for different working points of relevance for spectroscopic tests. (a) blue and red traces correspond to different RWB, respectivelly 10 Hz and 1 kHz. lineshape of figures (b)-(d) have been acquired for RBW=1kHz.

randomly distributed frequency fluctuations lead to a broadened profile having a gaussian lineshape. In order to enhance the signal-to-noise ratio, that is tipically quite low in a single-shot measurement, both these profiles have been obtained by averaging ten different acquisitions performed under the same experimental conditions. Remarkabely, the measured linewidth results to be well below the MHz range. In particular, at this wavelenght, the FWHM obtained for a RBW of 10 Hz is (53.8 ± 0.2) kHz while for a RBW of 1 kHz the value reduces to (25.8 ± 0.4) kHz.

Similar measurements, performed on a millisecond time scale (RBW=1 kHz), confirm the emission linewidth of both the laser diodes D1 and D2 to be in the order of few tens of kHz in the whole IR bandwidth involved in the DFG experiment. Just in order to give an example, in figure (3.2) measured line profiles are shown for emission at 1541.8 nm, 1550.0 nm and 1558.5 nm for the diode D1 and at 1575.0 nm for D2. In particular, the pair of lines of figure (3.2 a and d) and the pair of figure (3.2 and 3.2 c) are responsible for the generation of CW radiation at 5.573 THz and 4.094 THz, used in high resolution spectroscopy test (discussed in the following chapter).

Erbium-doped fiber amplifiers (EDFAs)

As we pointed out in the previous chapter, nowadays optical rectification technique is largely exploited for the generation of THz pulses. On the other side, during the years following the advent of the Tu-FIR laser technology, the attempts to obtain CW THz radiation following the DFG approach have been more and more sporadic. One of the most notable exception has been reported by M. Koch and co-workers in 2010 [89]. In that work a CW source, with THz output power in the milliwatt range, was obtained by nonlinear mixing (in a Cherenkov PM scheme) of two modes of a vertical-cavity-emitting laser (VECSEL), interacting on a $4 \cdot 10^{-4}$ cm^2 area within a PPLN crystal. Such a remarkable amount of power was achieved by converting, with a nonlinear efficiency of the order of 10^{-8} W^{-1}, about 500 W of IR power, obtained by positioning the PPLN crysyal within an optical cavity resonant with the pump frequencies. The main drawback of such a technique is the limited spectral coverage (about 200 GHz around 1.9 THz). These limitations, arising from the intracavity approach and from the PM constrains imposed by the periodically poled structure, are circumvented in a waveguided generation scheme. On the other hand, despite the larger nonlinear efficiency, expected as a consequence of the smaller interaction area, a valid alternative to the intracavity approach has to be found in order to properly enhance the pump power. For this purpose, in our setup we take advantage of three different amplifiers.

In our EDFAs (IPG Photonics) the seeding IR radiation is injected in an active medium, constituted by an optical fiber doped with Er^{3+} ions and pumped by 980 *nm* wavelength radiation. Similarly to neodymium, probabily the most used element in optical amplification devices, erbium is a rare earth metal. High values for electronic transitions cross-section and fluorescence times much longer than other elements makes the population inversion particularly easy to be achieved in such materials. In case of the erbium-based devices, the pumping radiation induces electronic transition from the ground state $I_{9/2}$ to the level $I_{11/2}$, from which electrons decay to the $I_{13/2}$ state with a typical relaxation time of about 1 μs. The interaction coupling of this latter level with the ground state has an average life time in the order of 10^{-2} *s*, allowing the population inversion to be established. The optical gain can be expressed as a function of the fiber length x and of the seed and pump intensity, respectively I_s and I_p:

$$\frac{I_s(x)}{I_s(0)} = exp\left[\left(\frac{I_p}{I_p^{sat}} - \frac{I_s(x)}{I_s^{sat}} - 1\right)Nx\right] \tag{3.2}$$

being N the population of the laser upper statete and I^{sat} the saturation intensities, given by $I_p^{sat} = \frac{h\nu_p}{\sigma_{pa}\tau}$ and $I_s^{sat} = \frac{h\nu_s}{2\sigma_{se}\tau}$. In these latter expressions σ_{pa} represents the pump absorption cross-section, σ_{se} the one associated to the stimulated emission process, while τ is the laser transition lifetime[1]. As it can be seen, the optical gain cannot be indefinetly enhanced simply by increasing the length of the fiber, because the upper laser level is depleted by stimulated emission processes. This contribution, expressed by the ratio $I_s(x)/I_s^{sat}$, can only be compensated by confining also the pump radiation within the active fiber, with a consequent increasing of the amplification length. For our purpouse, the width of the gain curve represents another crucial parameter, as it sets the upper limit for the tunability range of the THz source. In an Er-doped active medium the gain curve tipically ranges from 1430 *nm* up to 1640 *nm*. This broadband response is determined by the stark splitting due to the interaction of the Er ions with the electric field produced by the atoms of the material in which they are embedded. As a consequence, the energy levels involved in the laser transition split in many sub-levels spaced by about 10 *meV*, each one being broadened by the lattice vibrations. In other words, at room temperature the discrete structure of each multiplet turns into a continuous energy band, permitting the optical amplification of a tunable seeding source.

The optical parameters characterizing the three EDFAs employed in our setup are resumed in the following table:

---

[1] In the case of erbium-doped fiber these parameters assume the typical values $\sigma_{pa} = 3.1 \cdot 10^{-25}$ m^2, $\sigma_{se} = 4.64 \cdot 10^{-25}$ m^2 and $\tau = 12$ *ms*, leading to saturation intensities of the same order (10^7 W/m^2) for both the seed and the pump fields.

LABEL	OPERATIONAL WAVELENGTH BW	MAXIMUM OUTPUT POWER	MAXIMUM MEASURED GAIN
A1	1540 – 1565 nm	11 W	38.6 dB
A2	1573 – 1577 nm	7 W	35.4 dB
A3	1603 – 1607 nm	3 W	31.8 dB

As it will be shown in the next chapter of this work, this equipment allows us to implement a CW THz source spanning a spectral window potentially ranging from 1 to 8 THz.

Femtosecond laser

As already stressed, the main goal of this experimental thesis is to design and implement a DFG setup for synthesys of monochromatic THz radiation for high precision frequency spectroscopy and frequency metrology. To this purpose the narrow-linewidth telecom laser diodes and the fiber amplifiers are not the only indispensable ingredients. Indeed, absolute frequency measurements can only be accomplished by referring the seeding sources to the primary standard taking advantage of a frequency ruler. For this reason, a mode-locked laser (Menlo systems C-fiber HP), operating around 1.56 μm wavelength, is included in our setup. Similarly to the case of EDFAs, even in this device the active medium is constituted by a Er-doped fiber pumped at 980 nm. Here, the fiber is closed in a loop, being the pump radiation injected by a coupler. Passive mode locking is accomplished by a nonlinear optical loop mirror (NOLM [90]) mechanism, in which the round-trip time is stabilized by a second pulse circulating in the opposite direction within the same fiber ring. The spectral coverage of such a pulsed source, measured with a calibrated wavelength meter and visible in figure (3.3), matches with the tunability range of the CW laser diodes. Roughly $15 \cdot 10^4$ teeth, spaced by $\nu_{rep} = 100\ MHz$, are contained within this range, ensuring capability for IR (and therefore THz) frequency stabilization in the whole spectral region of interest.

Pulses duration is another key parameter, whose knowledge is of crucial importance in order to estimate the expected nonlinear efficiency of the optical rectification experiments. Performing an accurate measurement of the temporal width of an ultrashort laser pulse is not a trivial issue. Indeed, all the techniques based on direct electronic sampling are limited by the detector bandwidth. For example, measurements below the picosecond time scale are hard to be accomlished using a commercial fast photodiode, while temporal resolution below 200 fs can be achieved using a streak-camera [91]. Coherent techniques based on the quadratic response of a nonlinear medium are the most suited ones for pulse

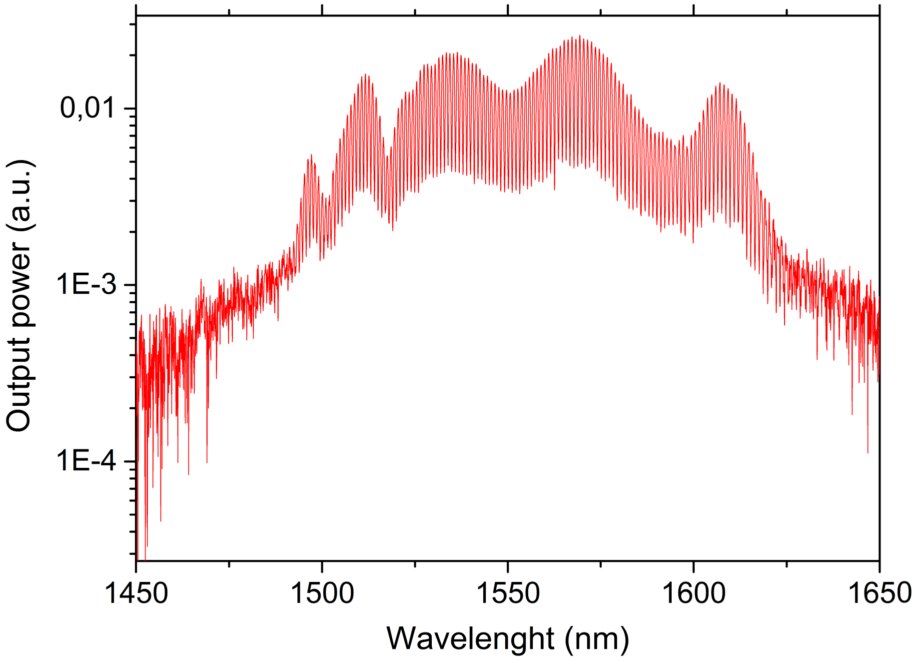

Figure 3.3: Optical spectrum of the mode-locked source.

durations of $< 100\ fs$. A largely adopted method consists, for example, in realizing a Michelson interferometer with an adjustable delay (τ) of an arm respect to the other and recombining the two pulses on a SHG crystal. Since the amplitude of the outcoming field will be proportional to the product of the single pulses amplitudes, a linear detector will provide a signal proportional to the so-called intensity autocorrelation S_{intAC}

$$S_{intAC} = \int I(t)I(t-\tau)\, dt. \tag{3.3}$$

SHG is not the only second order interaction suitable for autocorrelation measurements. The same information about the temporal pulse shape can, for example, be retrieved by exploiting the two-photon absorption (TPA) in a semiconductor photodiode [92]. This latter strategy is the one we choose to follow in this work. Indeed, being the silicon energy bang gap about twice the energy if of the IR photons at 1.55 μm, a commercial silicon photodiode (costing EUR 2) has been succesfully employed as a nonlinear signal generator. When the IR light is properly focalized on such a detector, while the linear absorption cross-section is negligible, the TPA occurrences provide a signal proportional to the square of the overall intensity, i.e.

$$\begin{aligned} S_{TPA}(\tau) &= \int [|E(t) + E(t-\tau)|^2]^2 dt = 2\int I^2(t)dt + 4\int I(t)I(t-\tau)dt + \\ &+ \quad 2\int \Re[E^2(t)E^{*2}(t-\tau)]dt + 4\int [I(t) + I(t-\tau)]\Re[E(t)E^*(t-\tau)]dt. \end{aligned} \tag{3.4}$$

The first integral on the right side of this equation does not depends on the delay and represents the measurement background while the second is, once again, the intensity autocorrelation. Note that, regardless of the pulse shape, for $\tau = 0$ the signal reaches its maximum, in a ratio 8:1 respect to the background. Anyway, in order to provide an explicit relation for the autocorrelation signal, a specific temporal profile has to be assumed. Since the mode-locked laser employed in our setup emitts, nominally, gaussian shaped identical pulses, we can substitute in the previous integral equation a complex electric field of the form

$$E(t) = A\ exp\left(-\frac{t^2}{2\tau_p^2} + i\omega t\right) \tag{3.5}$$

obtaining for the expected signal (normalized to the background)

$$S_{TPA}(\tau) = 1 + k\ (2 + cos(2\omega\tau))e^{-\tau^2/2\tau_p^2} + 4k^{3/4}\ cos(\omega\tau)e^{-3\tau^2/8\tau_p^2} \tag{3.6}$$

where ω is the carrier frequency of the pulse and the parameter τ_p is related to the full width at half maximum of its intensity profile by $\tau_{FWHM} = 2\sqrt{ln2}\ \tau_p$. The adimentional parameter k, whose value is 1 in the ideal case of perfect superposition of the two pulses on the detector surface, has been introduced to take into account slight misaglinment effects.

A schematic of the experimental setup has been depicted in figure (3.4). It basically consists of a Michelson interferometer in which, thanks to a motorized traslation stage (Thorlabs LTS300), the length of one arm can be adjusted with a resolution of 150 nm, corresponding to 1 fs delay. The transmitted pulse and its delayed replica are then recombined and focused on a reversely biased commercial silicon photodiode. In order to get an optimal spatial overlap on the detection area (4 mm^2 large) and an optical intensity sufficient to trigger the TPA process, a 25 mm focal length has been chosen. A variable attenuator (not shown in figure) has been used to adjust the pulse power, in order to avoid the saturation effect occurring beyond 10 mW of average power and visible in the non-linear photodiode response shown in figure (3.5 a). The upper envelope of the acquired auto-correlation signal $S_{TPS}(\tau)$, shown in figure (3.5 b), corresponds to relative delays

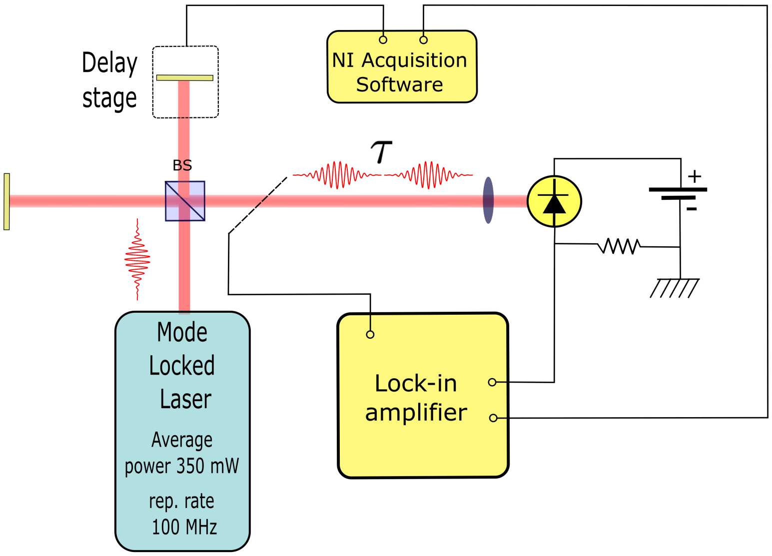

Figure 3.4: Schematic of the autocorrelation setup.

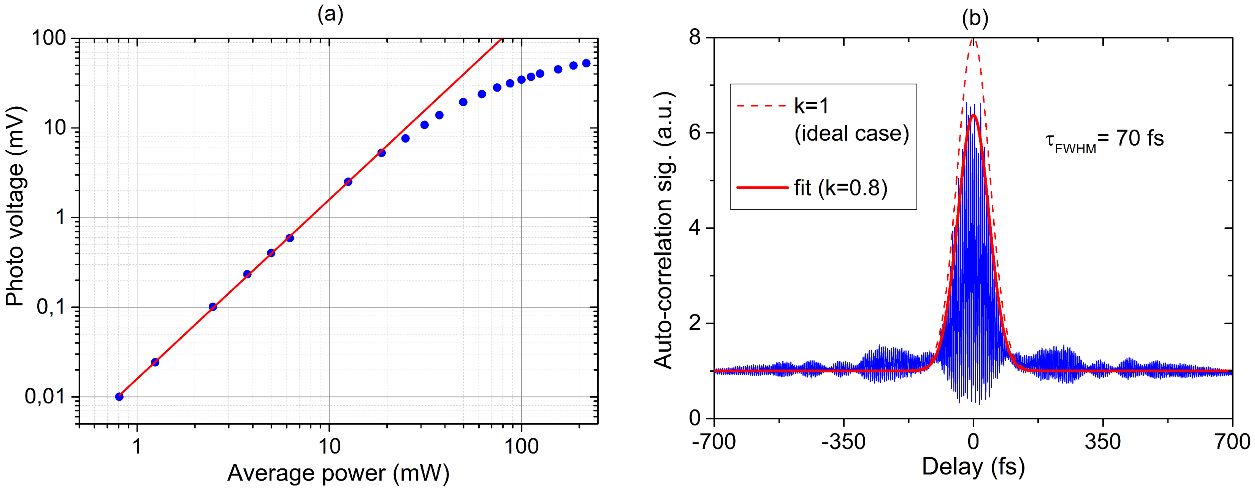

Figure 3.5: (a) Photo-conductive response in two-photon absorption regime. Saturation effect is visible beyond 10 mW of pulses average power. (b) Auto-correlation signal as a function of the relative delay.

equals to an integer number of the optical period. In perfect alignement conditions it should reach a signal-to-background ratio of 8 at zero delay. In more realistic situation the full-width at half-maximum of the intensity temporal profile can retrieved by fitting the envelope with the modified autocorrelation function (3.6), and provides for our laser a value of $\tau_{FWHM} = (70 \pm 4) fs$. It is worth to stress out that such a value, although in agreement with the nonminal one, coul be slightly underestimated because of the presence of a frequency chirp. This effect is also responsible for the background amplitude modulation, visible in the experimental trace. More importantly, we would also underline that an analogous measurement has been carried out for pulses after having passed through the nonlinear waveguide. Remarkabely, within the experimental uncertainty, no pulse spreading has been revealed.

3.2 The Lithium Niobate waveguide

Lithium Niobate ($LiNbO_3$, indicated as LN in the following) is an artificially grown ferroelectric crystal. Its optical properties, including uniaxial negative birefringence, pyroelectricity, piezoelectricity, electro-optic effect and optical nonlinearity [93], confer it a primary role in the optical communication technology. Indeed, starting from the early 80s years, plenty of LN-based integrated devices, as modulators, switches and ring resonators became more and more diffused [94]. Because of its ferroelectricity, LN, whose structure is shown in fig , is a non-centrosymmetrical crystal below the Curie temperature ($T_C = 1338\ K$). By virtue of this fact, it is largely employed in setups for frequency up- and down-conversion, particularly in combination with pump fields in the telecom range, where LN exhibits strong nonlinearities and a extaordinarily smallabsorption coefficient. This latter statement has a dramatic importance for those applications, such as the case of the present work, in which high optical intensities are required. Indeed, the absorption arising from impurities and intrinsic crystal defects in undoped LN [95]-[96] produces unwanted effects, such as limiting the nonlinear efficiency of the material or lowering the damage threshold. For example, in commercial congruent Lithium Niobate (CLN), whose concentration ratio is $[Li]/[Nb] = 0.94$, about $6 mol\ \%$ of Li sites are left empty. Despite the vacancies do not imply the opening of absorption channells, these can arise when an empty site is filled, for example, by a Nb^{5+} ion (Nb antisite defects). In this case, the excitation channell is called ”small bound polaron”and leads to a resonance at 775 nm [97]. Similarly, other intrinsic defects and/or extrinsic impurities cause absorbption bands but, remarkabily, none of these effects has a dramatic impact in the telecom bandwidth. Anyway, even at wavelengths close to 1.55 μm the optical resistance and the

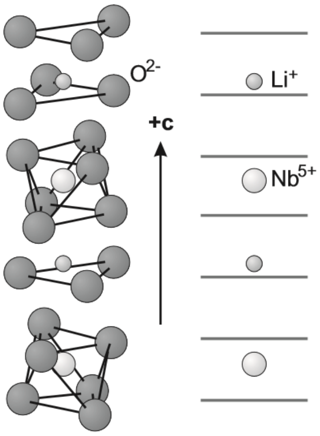

Figure 3.6: Crystalline structure of LN with indicated the extraordinary axis direction **c**. Image reprinted from [93]

transparency of LN are increased by the implantation of certain doping species within the bulk material. Among the different methods so far adopted to reduce absorption and photo-refractive damage, including thermo-electrically oxidizing [98] and crystal heating [99], the most suited one is to dope the LN with magnesium oxide (MgO). While for near-stochiometric (i.e. $[Li]/[Nb]$ = 0.98) LN doping concentration of 1.8 *mol%* are sufficient, for CLN the ”optical damage threshold”, meant as the minimum doping level needed in order to suppres photo-refractive damage, is of about 5 *mol%* [100]-[101]. In a way, the MgO doping has the effect to bring the material close to the stochiometric behaviour. Indeed, the Mg occupies the *Li* vacancies, inhibiting hence the formation of *Nb* antisites. The residual absorption mechanisms are mainly due to the presence of transition metal impurities [102]-[103], in particular *Ni* ions. In the telecom wavelength range, the absorption coefficient of optical-grade MgO:LN results to be in the order of $10^{-3}\ cm^{-1}$ for ordinary-polarized light and almost one order of magnitude smaller for extraordinary polarized light.

As well as providing better optical quality, the MgO doping can also change both the ordinary and the extraordinary refractive index of LN, proving to be a fundamental tool in nonlinear waveguides fabrication. Several experimental investigation have been carried out in years in order to provide accurate measurements of refractive index of doped and undoped LN. In the mostly adopted techniques, the IR dispersion curve is retrieved by mesuring the tuning range of a PPLN based OPO by varying the temperature or the incidence angle. The ordinary (n_o) and extraordinary (n_e) refractive index can be calculated on the basis of a semi-empirical relation, known as the Selmeier equation (SE). For ex-

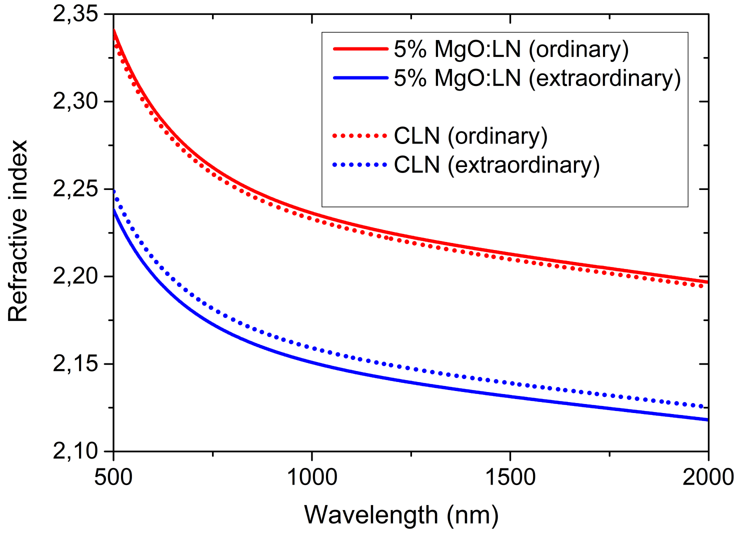

Figure 3.7: Dispersion curves for ordinary (red) and extraordinary (blue) refractive index of congruent (dotted lines) and 5%MgO-doped LN.

ample, experimental values for the Sellmeier parameters provided by Zelmon et al. [104] are available online in the open-access database refractiveindex.info. While these values well reproduce the optical behaviour of doped and undoped LN at room temperature, more recent measurements, performed for instance by Gayer et al. [105], allow to take into account also the temperature dependence of n. Let us take this opportunity to point out to the reader that, as these autors have noted (and we suspected), the parameter for n_o and n_e reported by Zelmon for 5%MgO:LN have been mistakenly exchanged. The (correct) room temperature dispersion curves for ordinary and extraordinary refractive index of both the materials have been plotted in figure (3.7). Note that the doping level affects the two refractive index values in opposite way, n_o being increased and n_e being reduced. For this reason, a waveguide can be accomplished in principle simply by doping the material in the region in which light confinement is intended to be achieved. In this case, anyway, it should be considered that only ordinary polarized radiation will be matched with the guided mode. In any case, other technique exist, leading to the opposite situation. Among the several waveguides fabrication techniques so far developed, two revealed to be suitable in the case of MgO:LN. These are ion implantation and proton exchange. Depending on the fabrication process, not necessarily ordinary polarized radiation will be held. For example, in the case of the waveguide used in our setup the opposite situation occurs, being such a structure only capable for extraordinary polarized light confinement.
In our setup, a 5% MgO:LN crystal plate (HCP Photonics), whose dimensions are $5x8x10\ mm^3$,

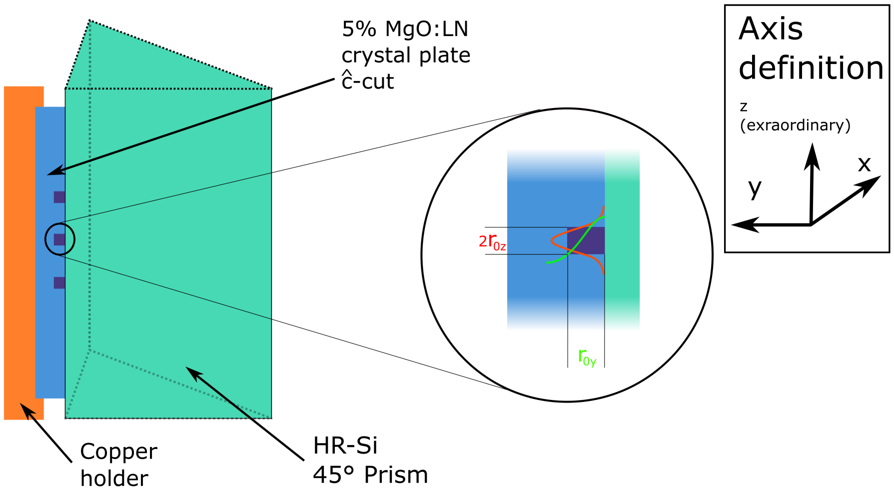

Figure 3.8: Pictorial reperesentation of the 5% MgO:LN crystal plate containing the channel and the planar waveguides.

contains two planar waveguides and nine channel waveguides extended along the whole 1 cm long side of the crystal. All of them are realized just beneath the crystal surface. The crystallographic axis $\hat{c}$ lies in the plane containing the waveguides and is orthogonal to them. In the following, and coherently with the notation adopted in the previous chapter it will be indicated as z, while the waveguides orientation will be indicated with x (see figure (3.8) for details). The incoming radiation, propagating along x, must be confined in the TE_{00} mode, with the electric field orientated along z. This particular crystal cut has been chosen in order maximize its nonlinear response by involving in the DFG process the highest component of the second order susceptibility, i.e. $d_{33} = 33 pm/V$ [106]. Unfortunately, we do not havr enough information about the fabrication process to allow us to retrieve the effective refractive index n_{eff} characterizing the waveguide neither the one of bulk crystal. Anyway, in the following we will assume as a valid one the extraordinary refractive index provided by the Sellmeier equation [104]

$$n^2_{eff} - 1 = \frac{2.2454\lambda^2}{(\lambda^2 - 0.01242\,\mu m^2)} + \frac{1.3005\lambda^2}{(\lambda^2 - 0.05313\,\mu m^2)} + \frac{6.8972\lambda^2}{(\lambda^2 - 331.33\,\mu m^2)}, \tag{3.7}$$

providing, this latter, a value for the waveguide reflectivity of 0.135 at 980 nm wavelength, in good agreement with the nominal one.

As we have seen in the pages dedicated to the theory of the Cherenkov generation, the guided mode dimensions are crucial parameters to provide an a priori extimation of the THz source performances. For this reason, we decided to spend some experimental efforts to characterize our waveguide.

Mode size measurement

Since the tipical dimensions of guiding optical structures usually are in the order of few microns, the waveguide geometrical properties are commonly inspected with the help of high resolution microscopes having, at least, x1000 magnification. Potentially, a different approach consists in collimating the outcoming light with a lens having a large numerical aperture and performing a waist measurement with the knife-edge method. Anyway, since the resolution of such a technique is limited to 10 μm with a commercial mechanical translator (ThorlabsXR25C), a precise measurement cannot be accomplished without a further magnification stage. Moreover, being the latter limited by the numerical aperture of the available optical elements, additional magnifying systems (e.g. telescopes) have to be introduced, leading to an unavoidable worsening of the measurement accuracy. For these reasons, we decided to try a different (and simple) approach. At this point, before to explain our method, is worth to briefly describe how the nonlinear crystal is positioned in our setup.

The crystal plate containing the surface waveguides, held by a metallic support, is mounted on a 3-axis plarform (Thorlabs MAX313D). Referring to figure (3.8), we will indicate, coherently with what we did in the first chapter of this thesis, as x-axis the propagation direction, coinciding with the 1 cm long side of the crystal. The plane containing the input facet will be indicated as yz, being the vertical z axis parallel to the extraordinary crystallographic axis $\hat{c}$. The lateral side of the crystal has been placed within a 0.3 mm deep housing carved on a copper plate surface. A thin Indium film is used to match the crystal-copper contact. In this way the crystal is protected from any damage arising from an excessive mechanical stress and the thermal contact, needed for a proper heat dissipation, is maximized. The surface containing the waveguide is in contact with the lateral side of an hi-resistivity silicon prism, needed to allow the extraction of the THz radiation. In this manner no glue has to be applied, being the crystal held by the pressure. The IR pumping light is coupled with the guided mode by a lens having a 4 mm focal length and is re-collimated at the output of the waveguide by another lens having a 7 mm focal length and a numerical aperture large enough to collect all the transmitted IR power. Both the lenses are coated by an anti-reflection multi-layer (transmittance $> 98\%$) and their position respect to the waveguide facets can be adjusted thanks to three mechanical translation stages having an accuracy of 1 μm. This resolution is sufficient to accomplish the measurement of guided mode size, as it will be now described.

When the IR light is focused on the waveguide facet, if we measure the transmitted optical power as a function of the relative distance between the optimal and the real position of the waveguide respect to the light spot, the expected intensity profile will be proportional to the convolution integral

$$T(y,z) = \iint I_f(\tilde{y},\tilde{z}) I_g(\tilde{y}-y,\tilde{z}-z) d\tilde{y} d\tilde{z}\,, \tag{3.8}$$

being I_f and I_g respectively the intensity profile of the incoming field and of the guided mode. Since the intensity profile of a focused gaussian beam is given by

$$I_f = I_{f0}\; exp[-2(y^2+z^2)/w_0^2], \tag{3.9}$$

if we assume also for the guided mode a shape in the form

$$I_g = I_{g0}\; exp[-2(y^2/r_{0y}^2 + z^2/r_{0z}^2)] \tag{3.10}$$

where r_{0y} and r_{0z} are the radius of the guided modes at the $1/e^2$ level, already defined in the first chapter, and w_0 is the beam waist or, in other words, the radius of the spot. With this assumption (to be experimentally verified), by measuring the transmitted intensity profile we will expect to observe a gaussan shape with radius at the $1/e$ level

$$\sigma_T^y = \frac{1}{2}\sqrt{w_0^2 + r_{0y}^2} \tag{3.11a}$$

$$\sigma_T^z = \frac{1}{2}\sqrt{w_0^2 + r_{0z}^2}. \tag{3.11b}$$

The most critical aspect of such a method consists in the determination of w_0. Since, in order to achieve an optimal mode matching, it would be in the order of few microns (ideally equal to the mode size) a direct measurement with the knife-edge method is practically impossible. A different strategy could be to calculate it by the ABCD formalism once the geometrical parameters of the beam propagating through the short focal lens are known. Unfortunately, even if this approach has been effectively tried, in our experimental conditions the ABCD formalism, entirely based on a paraxial approximation, provides unphysical results. On the other hand, a direct measurement of the beam waist can be accomplished by repeating the measurement of the transmission profile for different position of the wavegide facet respect to the focal point. Indeed, as the crystal is shifted away from the optimal position of a length Δx, the measured profile broadening scales as

$$\sigma_T^2 = a + b \cdot (\Delta x)^2 \tag{3.12}$$

where

$$a = \frac{1}{4}(w_0^2 + r_0^2) \tag{3.13a}$$

$$b = \frac{\lambda^2}{4\pi^2 w_0^2}. \tag{3.13b}$$

This broadening effect can be clearly observed in the different coloured traces of figure (3.9 a and b), correspondingly to transmitted intensity profiles acquired for different positions of the waveguide input, for both the vertical (a) and the horizontal (b) direction. Interestingly, while the gaussian shapes obtained along the z direction (a) are symmetric for every value of Δx, in the orthogonal direction an asymmetry is clearly visible. This reflects the fact that, while in the vertical direction the index distribution is symmetric, in the horyzontal direction the guiding medium interfaces with two different materials: on the left side ($y < 0$) with the bulk LN, on the right ($y > 0$) with the cladding material constituted by the HR-Si prism. For both the interfaces, the intensity decay can be well reproduced by fitting the experimental data with a gaussian profile but, regarding to the y direction, only the left half is of our interest as the volume corresponding to $y > 0$ is not involved in the generation process. For this reason, only the data corresponding to negative values of y has been fitted. In figure (3.9 c and d) the sigma-parameter of the transmitted intensity profiles have been plotted as a function of the waveguide shift Δx. The experimental data show, as expected, a linear dependence on Δx, even if a sensible worsening in the measurement accuracy is visible regarding figure (3.9 d). This effect is a consequence of the multiple fit performed to take into account of the just described asymmetry. The size of the beam spot w_0 and the radius of the guided mode have been retrieved from the fitting parameter by inverting equations (3.13) and the corresponding uncertainty have been calculated with the standard propagation formula. It also must be noted that, while the achieved values for mode dimensions (resumed in TAB) are in good agreement with the nominal ones, the measurements provide for the laser spot radius two different values in the y and z directions. In our opinion, this could be probably ascribed to a geometrical distortion of the focal area introduced by the 4 mm focal lens.

The last point to be discussed regards the extimation of refractive index gap Δn between the guiding region and the substrate, which will result to be usefull in the following. This parameter can be retrieved on the basis of the mode shape by applying the inverse WKB

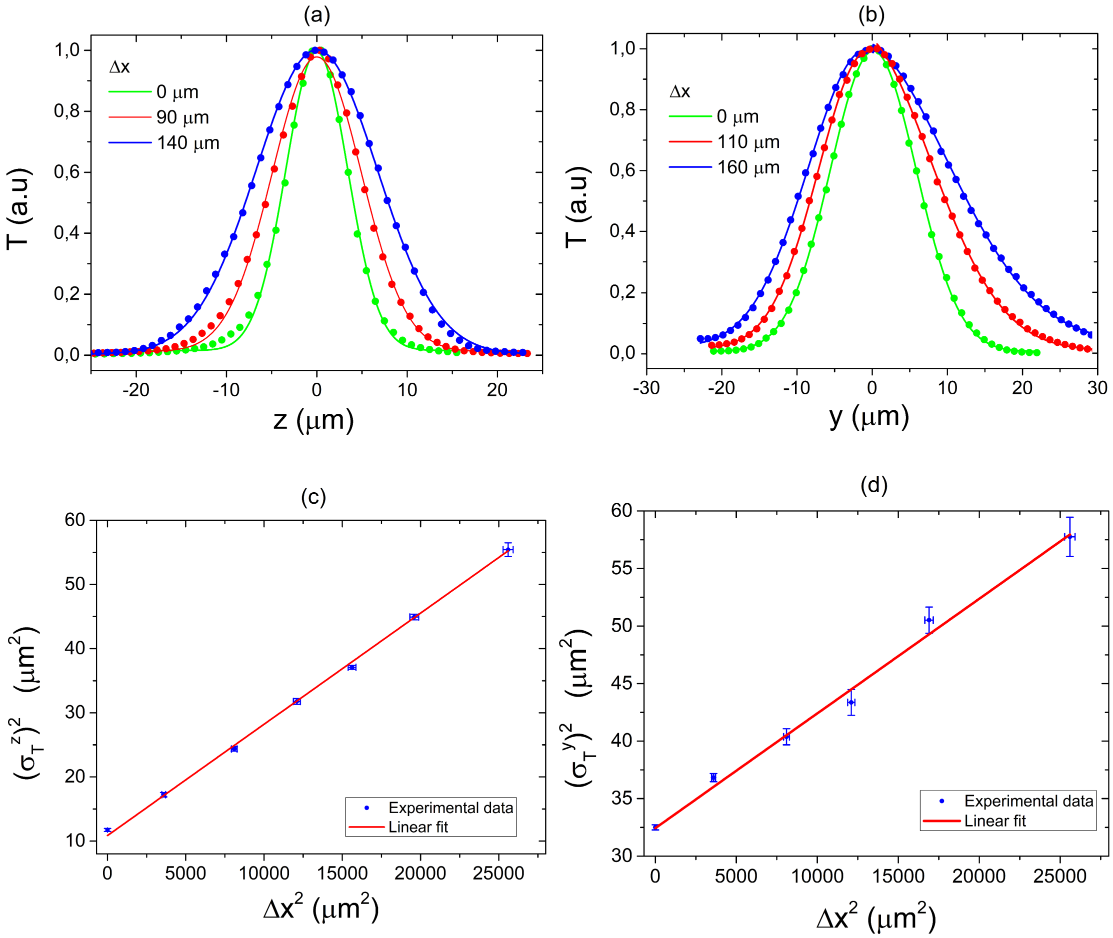

Figure 3.9: (a)-(b) Measured transmission profiles for different waist displacement Δx. Transmission profile width as a function of Δx^2 for vertical (c) and horyzontal (d) direction.

method [107]. In the weak guidance approximation (i.e. for $\Delta n << n_{eff}$), it can be calculated evaluating the expression

$$\Delta n(y,z) = -\frac{\nabla^2 \sqrt{I_g(y,z)}}{2n_{eff}k_0^2 \sqrt{I_g(y,z)}} \tag{3.14}$$

in $y = z = 0$. In the previous equation k_0 represent the free space wavevector, while for n_{eff} will be used the value provided by the Sellmeier equation (3.7). Furthermore, once the index gap is known, also the waveguide numerical aperture can be retrieved. It is defined as $NA = sin\theta_i^{(max)}$, where $\theta_i^{(max)}$ is the maximum acceptance angle at the waveguide input, and in our case can be approximated as

$$NA = \sqrt{n_{eff}^2 - n_{substrate}^2} \simeq \sqrt{2n_{eff}\,\Delta n}. \tag{3.15}$$

All the geometrical parameters characterizing our waveguide have been resumed in the following table.

r_{0y}	r_{0z}	n_{eff}	Δn	NA (angular acceptance)
$(8.3 \pm 0.2)\ \mu m$	$(2.95 \pm 0.27)\ \mu m$	2.13	$(4 \pm 1) \cdot 10^{-3}$	0.13 ($\pm 7.5^o$)

Optical losses measurement

In order to give, in the following, an accurate experimental measurement of the non-linear efficiency, interesting informations can be provided by the measurement of the optical lossess occurring during the IR light propagation. Indeed, while at 1.55 μm wavelength absorption losses can be neglected in 1 cm propagation length in 5% $MgO : LN$, other effects are involved, limiting the amount of power available in the guided mode. Another important effect is, for example, the energy conversion between the fundamental mode to other excited guided modes. However, since we work with a single mode waveguide, the contribution of this mechanism should be even less important than absorption. More serious effects are expected from the scattering lossess by surface roughness or defects that were present in the bulk material or that have been introduced by the fabrication process. These effects, particularly affecting semiconductor waveguides, are ineradicable in practice in any kind of integrated optical device. One more factor to be taken into account is represented by the tunneling losses. These occurs when the optical barrier between the guiding film and the cladding material is not sufficiently high for some reasons. In our case, this effect will be produced by the presence of the silicon prism, needed to extract the THz radiation. Indeed, its refractive index at the telecom wavelengths is higher than the LN one and, even if a small air gap (whose thickness is expected to be in the order of few μm) will be inevitably present, a non negligible fraction of the IR light will be extracted as well.

In order to measure the optical lossess, several experimental techniques has been so far adopted. One of these is the socalled cut-back method [108], consisting in comparing the transmitted power of identical waveguides having different lengths. Since is hard to replicate many devices with the same quality, this method is usually implemented by reducing progressively the length of a single sample by cutting it. Another non-destructive method is to measure the scattered light with a local probe or by near-field imaging [109]. This technique has the drawback to be strongly dependent on the quality of the output facet. Furthermore, in the case of surface waveguides, another possibility consists to couple the light by a prism placed in various positions along the propagation direction and measuring the output power any time (sliding prism method [110]).

Even if this latter approach would be suitable in our case, we have choosen to adopt a different one, proposed for the first time by Regener et al. [111]. It is based on the etalon behaviour of the nonlinear crystal, due to the fact that the input and output facettes possess a non-zero reflectivity. For a single mode waveguide and for a monochromatic input, the transmission can be treated analogously to that of a Fabry-Perot resonator in a plane wave approximation, resulting in an Airy function of the form

$$T_{FP}(\Phi) = \frac{(1-R)^2 e^{-\alpha L}}{(1-R')^2 + 4R' sin^2(\Phi/2)} \xi \tag{3.16}$$

where $R' = Re^{-\alpha L}$, being R the reflectivity of the input and output facetes (that we are supposing to be equal), α the absorption coefficient, L the crystal length and ξ the input efficiency. As it is shown in figure (3.10 a) , T_{FP} is a periodic function of the round trip dephasing $\Phi = \Phi_0 + 4\pi n_{eff} L/\lambda_0$, where λ_0 is the free space wavelength. The quantity of experimental interest is the contrast K between the interference fringes that characterize the transmitted power as the wavelength is continuously varied. It is defined as

$$K = \frac{T_{max}/T_{min} - 1}{T_{max}/T_{min} + 1}, \tag{3.17}$$

where T_{max} and T_{min} are respectively the maximum and the minimum transmitted power. It is worth to notice that this quantity does not depends on the precise knowledge of the refractive index neither on the overall coupling efficiency but only on R'. This can be retrieved by the relation

$$R' = \frac{1}{K}(1 - \sqrt{1-K^2}) \tag{3.18}$$

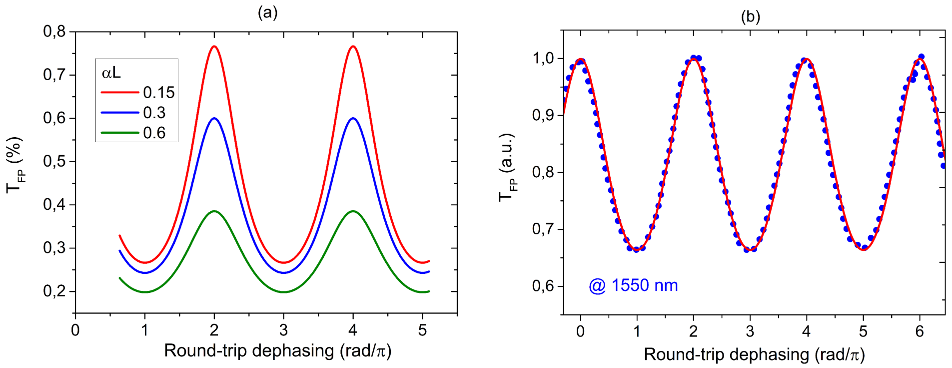

Figure 3.10: (a) Simulated waguide transmission fringes for $R = 0.3$, 100% input efficiency and $\alpha L = 0.15$ (red line), 0.3 (blue line) and 0.6 (green line). (b) Example of experimental transmission fringes (blue dots, normalized) and fit (red line).

and, once the reflectivity is known, the fraction of IR power that has been lost can be calculated as the ratio $\Sigma = 1 - R'/R$. The value of the reflectivity has been extimated exploiting the Fresnel equation

$$R = \left[\frac{cos\theta_i - \sqrt{n_{eff}^2 - sin^2\theta_i}}{cos\theta_i + \sqrt{n_{eff}^2 - sin^2\theta_i}} \right]^2, \tag{3.19}$$

being θ_i incidence angle, and n_{eff} to be retrieved by the Sellmeier equation (3.7). Regarding to the associated uncertainty, the main contribution arises from the uncertainty on the In principle, the input angle θ_i, which can range between zero and the maximum value allowed accordingly with the waveguide numerical aperture. Considering this as the only non-negligible contribution, the reflectivity, calculated to be 0.13 for normal incidence, may result under-estimated of about 1.54 % of its value.

In figure (3.10 b), for example, the experimental etalon profile, acquired for 1550 nm wavelength, is shown. These measurements have been performed by continuously changing the frequency of the seeding radiation in a range of about 40 GHz. The frequency adjustment is made possible by controlling the laser diodes external cavity with a piezo actuator driven by a continuous voltage signal. The ratio between the maximum and minimum transmitted intensity has been obtained by fitting the (normalized) experimental data with the function

$$T_{FP}(\Phi) = \frac{A}{1 + (B-1)sin^2(\Phi/2)}, \tag{3.20}$$

in which the fit parameters represent $A = T_{max}\Sigma\ \xi$ (and for normalized data is unitary, within the experimental uncertainty) and $B = T_{max}/T_{min}$ is the desired ratio. The lost energy fraction can thus retrieved by inserting this latter parameter in the relations previously given and propagating the fit error as usual.
The measured values for Σ have not shown any wavelength dependence within the considered range and all of them result to be compatible within the measurement accuracy. In conclusion, the amount of energy lost has been extimated to range between $20 - 21\%$ of the incoming one. Notably, this implies that, even considering a 100% input efficiency (i.e. $\xi = 1$ in eq. (3.16)), the maximum transmitted power may not exceed the 61% of the incoming one.

3.3 Nonlinear efficiency in the pulsed regime

Before we focus on the synthesis of single frequency THz radiation, the nonlinear waveguide has been tested in the generation of THz pulses by OR. At this stage, our main goal was to choose an optical setup ensuring an optimal collection of the produced radiation, an operation made considerably more easy by the high generation efficiency available in the pulsed regime. Indeed, the mode-locked source at our disposal provides 70 fs pulses with up to 50 kW peak power, leading, accordingly with calculations, to a THz spectral coverage extended to about 8.5 THz and an amount of THz power that allows, not only the room temperature detection, but also the visualization of its beam shape with an appropriate imaging system, namely a THz real-time camera (INO IRXCAM-THZ). Collecting a THz field is not an easy task, because phonon resonances and losses by extrinsic impurities in glasses make the common lenses unsuitable for applications in the THz range. Parabolic mirrors and polymeric lenses are, instead, optical elements largelly used for collimation and focalization of THz beams. Furthermore, the expected spatial profile for the surface emission is, in our case, strongly asymmetric. In the xy plane the angular distribution is sharply picked around the Cherenkov angle, because of the high value of the L/λ ratio contained in the phase mismatch term. Oppositelly, since the guided mode in the z is much smaller than the THz wavelength, the generated radiation undergoes strong angular dispersion in the xz plane. Different optical systems have been tested in order to optimize the THz collection, beginning with parabolic mirror. Therefore, even if these are the most appropriate choice to focalize a paraxial THz beam, a more axis-indipendent optical element is needed for the initial collimation. For this purpose, both a cylindrical lens (made of TPX and fabricated by Tydex company) and a cylindrical mirror have been tested. Finally, since the 1 cm thick TPX lens introduced unacceptably high absorption losses (about the 80%) the reflection geometry has been prefered. A cylindrical mirror having 2.54 cm diameter and 2.54 cm focal length has been placed along the THz optical path. For a good initial positioning, the emission angle with respect to the pump propagation direction x has been estimated by taking into account the deflection introduced by the presence of the silicon prism. As we already seen, the presence of a prism-shaped cladding material is unavoidable in order to prevent total internal reflection. The prism used in our setup, made of high-resistivity silicon and having $n_{Si} = 3.416$ refractive index in the THz range [112], has 1 cm thickness and two acute angles of 45^o. Note that, despite the Cherenkov angle is affected by the nonlinear medium dispersion, no appretiable variation occurs in the propagation direction for the different spectral components of the THz pulse. Indeed, as it immediately follows from the Snell law, the angle θ_{cladd} respect to the normal to the LN/Si interface is determed by

$$sin\theta_{cladd} = \frac{n_{LN}^{THz}}{n_{Si}} cos\theta_c = \frac{n_{LN}^{IR}}{n_{Si}}, \tag{3.21}$$

showing how the cladding angle could be affected only by the dispersion of the IR spectral components. However, such an effect is negligible for our scopes, and the collection angle can be safely considered to be constant at about 62^o with respect to the x direction. Clearly, it does not exclude the fact that the different spectral components of the THz pulse generally undergo different transmission at the interface. To this regard, it is worth to say that is not easy to quantify how this affects the power spectrum of the extracted radiation, because a Sellmeier equation providing the MgO:LN dispersion curve beyond 3 THz has not yet be reported in litterature [113].

Experimentally, the collection efficiency has been estimated by measuring, with a calibrated pyroelectric detector, the power carried by the THz beam progressively obscuring the mirror collection area. This measurement demonstrates more than 98% of the outgoing radiation to be contained in a rectangular area of $1.0x2.1\ cm^2$ lying in the cylindrical mirror plane, being this latter one oriented alongside the emitting surface.

As it has been said in section (3.1), no appretiable pulse spreading seems to be introduced by the nonlinear medium. As a consequence, the whole crystal length is expected to be uniformly involved in the generation process. This fact has been experimentally confirmed by performing a knife-edge measurement on the THz spot, namely by obscuring the mirror surface with an opaque plane (in this case, several paper layers) progressively shifted along the x direction. Under the assumption of an uniform generation, a linear decay of the collected power is expected. Within the measurement accuracy, such a linear decreasing is actually visible in the experimental data reported in figure (3.11 a), in which the collected power is shown as a function of the knife-edge position.

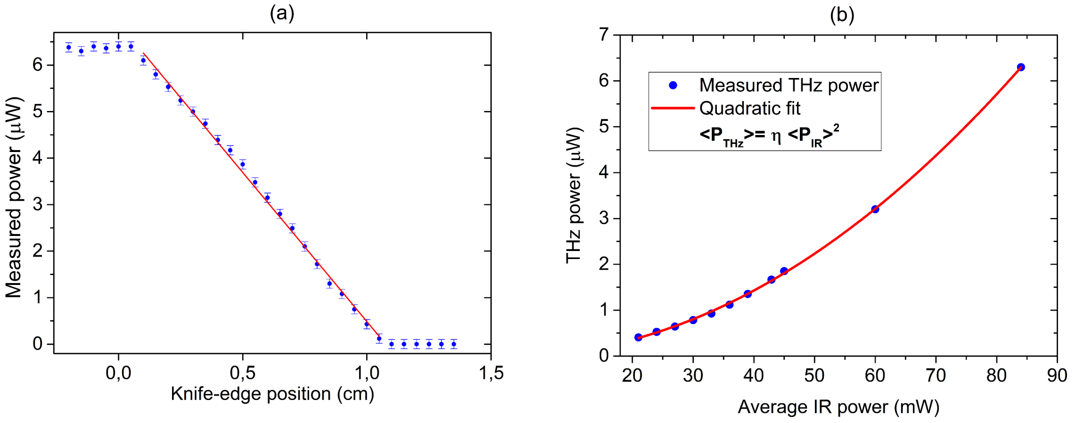

Figure 3.11: a) Knife-edge measurement of the THz power intensity distribution in the x direction. The linear scaling observed suggests the whole waveguide length to be uniformly involved in the DFG process. b) Average power of the generated THz pulses as a function of the average IR pump power.

The collimated THz beam, amplitude-modulated at 30 Hz by a mechanical chopper-weel placed along the IR pulse path, has been focalized on a pyroelectric detector. The produced signal has been measured by means of a lock-in amplifier. A variable attenuator, placed along the IR beam, allowed us to measure the available average power of the THz pulses as a function of the pump average power couped with the waveguide. This latter one has been measured collimating the IR light outcoming from the waveguide with a short focal lens (placed on a removable stage) and focusing it on an IR power-meter. The expected quadratic power scaling is visible in figure (3.11 b), with a nonlinear efficiency, retrieved from the fit, of $\eta = 8.9 \cdot 10^{-4}$ W^{-1} and a maximum measured power of 6.3 μW, corresponding to 84 mW average pump power. Considered the 100 MHz ML laser repetition rate, the generated THz pulses have 0.063 pJ energy, correspondingly to $7.5 \cdot 10^{-5}$ conversion efficiency. If compared with similar experimental studies (see, for example S. Fan et al. [114]), we must conclude that further improvements in the generation efficiency are actually possible. Anyway, it must be said that a precise quantitative estimation of the improvements to be expected is not easy, because in order to compare accurately our results with the other published ones several other parameters should be known. For example, since the THz windows is characterized by the presence of plenty water absorption resonances, we should compare THz power levels recorded after the same optical path in air. In any case, as we wil discuss also in the chapter dedicated to the generation of CW THz radiation, it seems reasonable that higher amount of power

available for experiments can be obtained by properly shaping the silicon prism surface in order to minimize the reflection losses inside it.
Finally, further useful informations could be retrieved from the measurement of the spectral profile of the generated THz pulses. This can be accomplished by taking advantage of the polarization gate induced by the THz pulses on a GsAs crystal by means of the electro-optic effect [115]. Such a measurement, currently in progress at our THz lab, will allow to get the informations required in order to compare our experimental results with the predictions provided by the theoretical model described in the previous chapter.

3.4 Waveguide coupling and power handling

In principle, the design of a DFG experimental setup for CW THz radiation is not hard to be carried out. Indeed, the only indispensable optical elements are a beam splitter, to ensure co-propagation of the IR laser beams, and a simple lenses system, to match them with the guided mode. This is even more simple in pulsed regime, in which the frequencies to be nonlinearly mixed are naturally contained in the pulsed laser beam. As we mentioned in the first chapter, waveguided generation of THz pulses by OR in MgO:LN has been already accomplished by K. Kawase and co-workers [83]. In that work the authors refer specifically to the opportunity to realize an analogous setup in CW regime. On the other hand, despite its undoubted usefulness, to the best of our knowledge no attempts to accomplish a such a setup have been reported to date. On the contrary, the goal to confine several watts of IR power in the tiny volume of a channel waveguide constituted one of the main challenges of the present work. For this reason, we consider appropriate to describe the principal technical criticalities and the experimental countermeasures adopted in order to overcome them.

Power losses minimization

At first, two mutually correlated aspects have to be discussed. These regard the power losses occurring along the path from the EDFAs to the LN crystal and the polarization costrains imposed by the waveguide. Indeed, given the poor conversion efficiency of any nonlinear process, it is important that as much optical power as possible effectively reaches the crystal input. At the same time we know that, in order to take full advantage from LN nonlinear features, the waveguide has been designed to transmit only vertically polarized light. As a consequence, the polarization selectivity implies that at least half of the available IR power has to be wasted, being a non-polarizing beam splitter (NP-BS)

the only suitable optical element[2] to achieve the spatial overlap of the pumping beams. This scenario is further complicated by the need to prevent the amplifiers damage arising from optical feedback. Indeed, as the light coming from each EDFA is focused on the crystal facet, a considerable amount of power is back reflected also on the other one, resulting in seeding radiation out of the operational wavelength bandwidth. this could actually lead to a permanent damage of the amplifying medium. For this, reason two optical isolators (Thorlabs IO-5-1550-HP) have been placed after the NP-BS, i.e. along the path of the co-propagating beams. On the whole, they transmit about the 87% of the incoming power and provide a 60 dB attenuation of the feedback signal. Since each isolator, adjusted to provide to the waveguide a vertically polarized beam, introduces a 45^o rotation in the field polarization, the transmission is maximized for horizontally polarized input. This configuration is accomplished thanks to two fiber polarizers placed before each amplification stage.
The need to fully control the beams polarization arises even from another detail. Despite its nominal characteristics, for high power levels the NP-BS exhibits a polarization dependent behaviour. In particular, for horizontally polarized light we observed a transmission coefficient of about 65% while about 35% of the incoming light is reflected. Since in a second order optical process the generated THz power will scale as the product of the IR beams powers, we decided to use for nonlinear generation the reflected part of the more intense beam (provided by A1) and the transmitted part of the weaker one (A2 or A3, depending on the adopted configuration). Thanks to this approach we can remarkably reduce the amount of power to be confined in the guided mode, keeping the THz intensity unchanged. For example, in the high frequencies configuration (A1+A3) this choice allows us to get the same result dealing with 5.8 W to be coupled with the waveguide instead of 8.2 W.

Mode stability and shaping

Another difficulty is represented by the modal stability of the amplified radiation. It is coupled out from the EDFAs by a 1 m long high-power single mode fiber, and collimated to get a TEM_{00} gaussian mode. For such a single mode fiber, the geometrical features of the laser beam can be fully described in terms of the sizeof the beam waist (w_0) and its distance from a designated point. On the basis of these parameters, the optical setup has been designed by performing numerical simulation based on the ABCD formalism. In order to maximize the waveguide coupling, both the IR beams have to be

---

[2] Different wavelength-selective optical elements, as dichroic mirrors or notch filters, have also been considered. However, none of these items are capable of superimposing fields whose wavelength differs

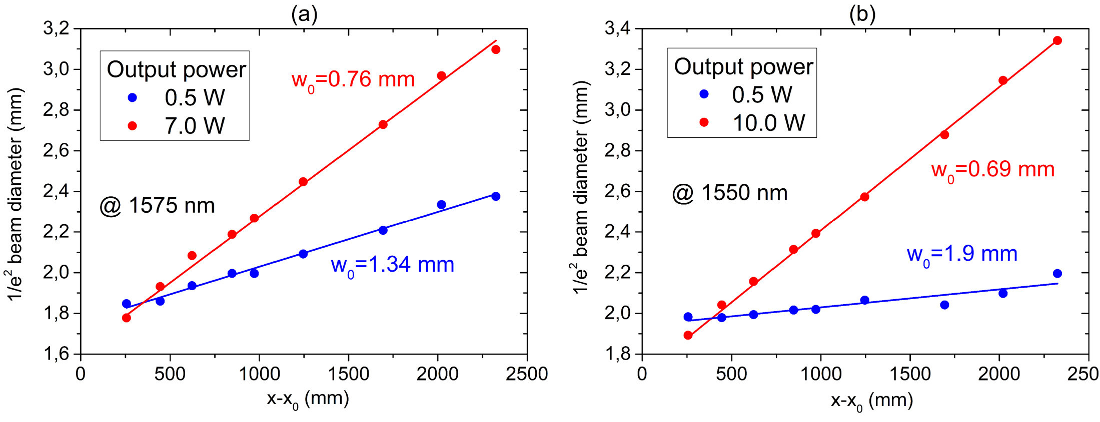

Figure 3.12: Amplified beams divergence measured for different ampligication gain. A clear instability of the geometrical parameters is visible for both amplifier A2 (a) and A1 (b).

properly shaped in size and divergence. Since such a pre-shaping system acts on both the laser beams simultaneously, the geometrical parameters of the amplified beams should be stable in time and independent on the amplifier gain. For this reason, we carried out an accurate geometrical characterization,for both low and high optical power, using the knife-edge method[3]. Unfortunately, while the waist size and position result to be constant in time, they undergo dramatic variations as the optical gain is changed. In figure (3.12) the measured profiles of the laser modes provided by the amplifiers A2 ans A1 are reported for low and high power regimes. In this picture, the beam diameters at the $1/e^2$ level have been measured at different position respect to the NP-BS. The laser propagation exhibits, in the considered region, a linear divergence and, for this reason, accurate measurements of the beams positions cannot be retrieved. Anyway, the data show a considerable decreasing of the waist, and therefore of the collimation length. In particular, switching from low to maximum available power, the beam waist decreases by a factor 1.76 for amplifier A2 and by a factor 2.75 in the case of A1. In order to compensate this effect, an adjustable telescope has been realized on each of the pumping beams, before the NP-BS. This configuration, combined with a continuous monitoring of

---

for only few nanometers.

[3] The knife-edge method consists in measuring the laser beam power while its transversal section is progressively obscured by a razor blade. If the transverse intensity distribution is assumed to be gaussian, its radius at $1/e^2$ level (w) can be retrieved by fitting the experimental data with a complementary error function, i.e. $P(z) = A \cdot erfc(\sqrt{2}z/w)$. Repeating such a procedure at different distances from a fixed point x_0 along the beam propagation, the waist w_0 can be obtaining fitting the data with the usual function $w(x) = w_0\sqrt{1-(\frac{\lambda(x-x_0)}{\pi w_0^2})^2}$.

the IR power coupled to the guided mode (allowed by the optical system described in the following chapter), ensures the whole system to be fully controlled and any perturbation in the experimental conditions promptly corrected.

High-power coupling efficiency

In the present experimental setup, we have to consider the intreating condition of focusing and guiding a considerable amount of power in a few square μm waveguide section. The main difficulties we expect arise from the material undergoing a local perturbation in the optical properties. This leads to a refractive index decreasing Δn (< 0), spatially modulate according to the intensity profile. Thus, the center of the incoming beam undergoes a larger phase delay respect to the periferic rays, which implies a wavefront distortion and, consequently, a self-defocusing of the IR light. This behaviour can be traced back to two distinct effects: the thermo-optic effect and the photo-refractive effect. For our purpose, we care about quantify Δn and verify to be smaller than the index gap providing the light confinement.
Let us start considering the thermo-optic effect (often named also thermal-lensing). This argument can be easily treated thinking at the refractive index as a thermodynamic quantity and expressing it as a linear function of the absolute temperature, i.e.

$$n = n^0 + \left(\frac{dn}{dT}\right) T \tag{3.22}$$

where n^0 represent the unperturbed value and the first derivative can be positive or negative, depending on the material. For MgO:LN a conservative estimate is given by the value $dn/dT = -3 \cdot 10^{-5}\ K^{-1}$ [106]. The temperature depending term can be related to the intensity profile by the heat-tramsport equation

$$(\rho C)\frac{\partial T}{\partial t} - k\nabla^2 T = \alpha I(r) \tag{3.23}$$

where (ρC) is the thermal capacity per unit volume, k is the thermal conductivity (for Mgo:LN we can take $k = 5\ W\ m^{-1}K^{-1}$) and α the absorption coefficient. For CW operation a steady state solution (i.e. for $\partial T/\partial t = 0$) could be exactly retrieved once the intensity distribution is known. By the way, in order to calculate the order of magnitude of Δn is sufficient to approximate $\nabla^2 T \simeq -T^{(max)}/R^2$, where $T^{(max)}$ represent the temperature at the center of the spot and R is the spot radius. Under this assumption the refractive

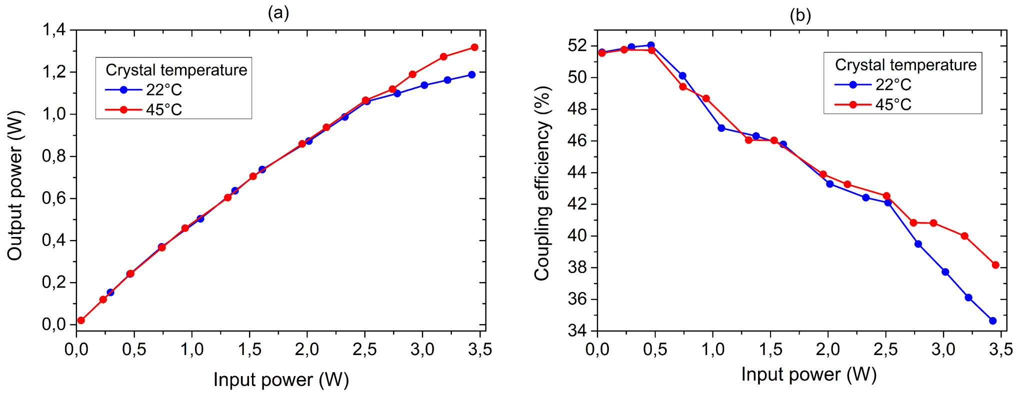

Figure 3.13: (a) Transmitted Vs incoming power and coupling efficiency (b) in planar waveguide geometry for different crystal temperature.

index variation can be extimated by the relation

$$\Delta n = \left(\frac{dn}{dT}\right)\frac{\alpha R^2 I^{(max)}}{k}. \tag{3.24}$$

It is worth to notice that this modification is proportional to the beam intensity, accordingly to the fact that thermal lensing effect is a third order nonlinear effect. Assuming an absorption coefficient of about 0.0001 cm^{-1}, a spot radius of about 3 μm and an optical power of 10 W we obtain as an order of magnitude $\Delta n \simeq 10^{-6}$.

The second phenomenon affecting the LN optical proerties is the photo-refractive effect (PRE). Unlike the thermo-optic effect, it doesn't emerges as a consequence of the nonlinear susceptibility, but rather of LN photo-voltaic and electro-optic properties. Indeed, PRE can be described as follow: when a LN crystal is illuminated by a light intensity I, it induces a charge migration resulting in a photocurrent proportional to I and directed along the extraordinary axis z. The electrons, moving to the darker areas, lead to a static electric field **E** and, as a consequence, to an Ohmic drift current compensating the charge migration. The overall current density can be written as

$$\mathbf{j} = \beta I \mathbf{e}_z + \sigma \mathbf{E} \tag{3.25}$$

where β is the photovoltaic constant of LN and σ its conductivity. In this case, the refractive index change appears as a consequence of the electro-optic effect, accordingly to

$$\Delta n = -\frac{1}{2}n^3 r_{33} E_z \tag{3.26}$$

where r_{33} is an element of the electro-optic tensor (30 pm/V) and E_z is the vertical component of the overall electric field, i.e. the sum of the optical one and the one generated by the photovoltaic effect. The former contribution can be extimated assuming again an infrared power in the order of 10 W and a mode radius of 5 μm. With these parameters the optical electric field results to be $E_z^{opt} \simeq 3.5 \cdot 10^6 V/m$, leading to an extimated change in the refractive index in the order of $\Delta n = -5 \cdot 10^{-4}$. Regarding to the photovoltaic contribution to the electric field, an a-priori calculation is not trivial to be accomplished, requiring to take into account the contribution of different photoactive centers. A similar theoretical effort have been carried out by J. Villaroel et al. [116]. In that work the autors pointed out that the number of impure ionic species to be considered grows with increasing intensity, and develop a model applicable up to an optical power density of about 10^3 W/cm^2. Unfortunately, being the intensity expected in our setup in the order of 10^7 W/cm^2, such a model is not able to provide reassuring informations for our experimental conditions. Anyway, in the same paper, the authors proposed to preserve at least part of the coupling efficiency in a planar waveguide by submitting the material to several heating cycles. Inspired by this suggestion, before to attemp to confine the high power beams into the channel waveguide, we decided to perform a preliminary test on one of the planar waveguides present in our crystal plate[4]. For such a measurement, a cylindrical lenses system has been used in order to realize an elliptic spot having, in the horizontal direction y, about 5 μm diameter and ensure an optimal mode-matching. Regarding to the vertical direction z, in this planar structure the beam propagates mantaining unchainged its gaussian shape. An analogous optical system has been used to collect the IR light at the waveguide output and send it to a power-meter to measure the tramsmitted power. A waist of about 150 μm has been chosen in order to keep the beam collimated for the whole crystal length and to reach an optical intensity of about $3.5 \cdot 10^5$ W/cm^2, i.e. an intermediate value between the maximum one reported in litterature and the one needed to be reached in our setup. In order to heat the waveguide, an electric resistance has been put in thermal contact with the crystal metallic holder. In figure (3.13) the output Vs input power is plotted: for room temperature operation a worsening of the coupling efficiency

---

[4] Its worth to underline that our efforts to achieve CW THz generation in a planar geometry has been carried on for two different reasons. On one hand the need to preserve a good coupling effciency at high-power by increasing the spot area, on the other side, regarding the THz radiation, a better collection efficiency was expected by reducing the emission divergence.

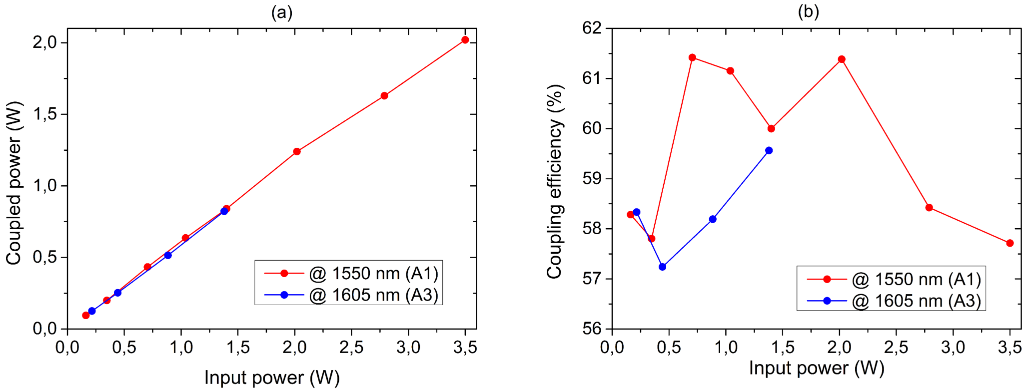

Figure 3.14: (a) Transmitted Vs incoming power and coupling efficiency (b) in channel waveguide geometry.

is clearly visible beyond about 2 W of input power (blue trace), while a slight increasing of the confinament capability seems to be evident for a crystal temperature of $45^o C$ (red trace in figure). Despite this results has been reproduced by subsequent measurements, no further improvement has been observed bringing the material to higher temperatures (up to $60^o C$). In any case, the observed trend for the coupling efficiency is far to be satisfactory and the planar waveguide approach has been abandoned. On the other hand, this set of measurements has allowed us to notice an intresting fact: the modal shape collected at the output of the planar waveguide (that we are not able to show for lack of imaging instrumentation on our disposal) seems exhibits no photo-induced divergence in the horyzontall plane. In other words, we experimentally checked that the refractive index change electro-optically induced by the photo-voltaic field is very much smaller than the typical waveguide index gap (i.e. $\Delta n << 0.004$) even at $10^5\ W/cm^2$ of optical intensity.

As a final step, we switched back to the channel waveguide configuration. The experimental curves reported in figure (3.14) stand to demonstrate that, even in this case, the guiding structure allows to compensate the photo-induced beam defocusing. Indeed, as it can be seen, the transmitted intensity is stable varying the input power, up to the maximum values available with our amplifiers. The measured the coupling efficiency for the curves exposed in figure is of about 57% for all the used amplifiers and, what is more important, the same efficiency is preserved in the dual frequency configuration, in which both the signal and the pump beams are coupled with the guided mode. The coupling efficiency reproducibility and the stability of the realized apparatus have been put to the test by several hours of high-power operation per day, for a period mesurable in some hundreds of days during this PhD course. Slight day-by-day fluctuation have been observed but, however, the system stability is such as to ensure an high-power coupling efficiency always bounded to the range 55 – 60 %. We care to point out that, remembering the waveguide losses being about the 20% of the incoming power, no further improvement in the coupling efficiency can be reasonably expected.

4

CW THz radiation for high precision spectroscopy

The previous chapter has been devoted to the main technicalities related to the building of the experimental setup for the generation of coherent THz radiation. From here on, we will focus our attention on the obtained results regarding the main goal of this work, namely the realization of a CW THz spectrometer potentially capable for frequency metrology.

The millimeter/submillimeter spectral region is fully recognised as one of the most suitable ones for studies of fundamental importance, particularly regarding the physics of atmospheric and interstellar gases [117]. Until the present moment, anyway, because of the difficulties hystorically accompanying the development of THz technology, the experimental efforts have been mostly focused in the microwave region. On the other hand, since the transition probability for the rotational transitions increase with the frequency, the accomplishment of new spectroscopic tools in the THz spectral region could significatively improve the capability of detecting molecules.

As we have seen at the beginning of this work, the challenge to realize a metrological-grade, CW source spanning the whole THz region dates back to the the days of TuFIR technology, almost 30 years ago. This kind of source had proven performances able to challenge the most advanced present-day CW THz sources, performing high resolution spectroscopy up to 6 THz, with two examples at frequencies as high as 7.9 and 9 THz [64]-[66]. However, the low reliability and very low emitted powers of that very bulky instrumentation, hampered for decades its widespread use.

More recently, more compact designs, basically QCLs, photomixers and frequency multipliers, have been sucessfully employed for absolute frequency measurements in the low frequency part of the THz spectrum, e.g. at 0.29 THz [118], 0.62 THz [119], 1.1 THz [26], 2.5 THz [120]-[122] and 3.3 THz [123]. Anyway, a proper figure of merit of the existing scenario must be better given considering, not only the spectroscopic performances, but also few other crucial parameters as the output power, the spectral coverage and the mode-hop-free tunability range.

The following table resumes, for each the aforementioned technologies, the record accuracy[1] achieved in spectroscopic measurements as well as the other characteristic parameters.

	OUTPUT POWER LEVEL	GENERATION BW AND MODE-HOP-FREE TUNUNG (MHFT)	FREQUENCY ACCURACY IN SPECTROSCOPY ($\Delta\nu_c/\nu_c$)
QCLs [120]	1 mW	2.5 THz (MHFT= 300 MHz)	$4{\cdot}10^{-9}$
Frequency Multipliers [26]	1 μW	0.9-1.2 THz (MHFT= 200 GHz)	$<1{\cdot}10^{-9}$
Photomixer Synthesyzers [121]	3 μW	0.2-1.5 THz (MHFT= 120 GHz)	$8{\cdot}10^{-8}$

All the values reported in this table refer to the specific device used in the considered spectroscopy experiment and are not necessarily indicative of the whole devices family, especially regarding to the THz QCLs. Indeed, remembering the discussion carried out in the first chapter of this thesis, it must be stressed that the direct lasing action up to 4.47 THz or with mode-hop-free tunability range up to 330 GHz has already been demonstrated. Anyway, is a matter of fact that the accomplishment of a single device possessing all the desired features seems to be still far to come.

In the present chapter (and in the following one) we will provide a full characterization of the CW THz source realized in this work, in order to frame it in the existing scenario.

4.1 Characteristics of the CW radiation

Let us start discussing the features of achieved CW THz emission in terms of absolute output power, conversion efficiency and spectral coverage.

---

[1] Tipically the parameter qualifying the performances of a certain source in spectral frequencies measurements is the ratio $\Delta\nu_c/\nu_c$, where ν_c is the measured line center and $\Delta\nu_c$ the associated uncertainty. Following the usual convention, in this work such a parameter will be called ‘’accuracy” or ‘’relative precision” depending if the source is refered to a frequency standard or not.

A schematic of the experimental setup is shown in figure (4.1). A fiber splitter takes the emission provided by each one of the CW laser diodes D1 and D2 (linewidth $\simeq 30\ kHz$ on a millisecond time scale, see section 3.1 for details). While 10% of the out-coupled IR radiation (about 2 mW) is amplified and matched with the nonlinear waveguide, the 90% is sent to a wavelength meter (Bristol model 721), having 1 GHz resolution, for frequency scans calibration. The THz spectral window potentially accessible with our CW source is limited by the operational bandwidth of the employed fiber amplifiers (EDFAs). In our setup, the involved parameters allow a spectral coverage ranging from 0.97 THz to 8.12 THz, given by the union of two distinct spans, corresponding to the possible arrangiaments of the EDFAs. More precisely, since the amplifiers A2 and A3 are characterized by a relatively small operational bandwidth (< 0.5 THz), they are preferibly used to amplify IR radiation at a fixed frequency provided by laser diode D2. Oppositelly, amplifier A1 operates between 1540 nm and 1565 nm wavelength, corresponding to a tunability range of more than 3 THz. This amplifier, seeded by the laser diode D1 can be used in combination with A2 or A3 to generate in the 0.97-4.57 THz range or in the 4.54-8.12 THz range, respectively. The amplified beams are spatially overlapped in a non polarizing beam splitter and, taking advantage of the technical measures described in section 3.4, about $55-60\%$ of the available power is coupled with the guided mode within the nonlinear crystal.

The optical setup used to collect the emitted power is analogous to the one employed in the case of THz pulses detection and consists of a cylindrical mirror of 2.54 cm focal length and having a diameter of 2.54 cm. The collimated radiation, 10 Hz amplitude modulated by a mechanical chopper wheel positioned along one of the IR beams, is adapted to be employed in the spectroscopy setup or directly focalized on a Golay-detector and measured with a lock-in amplifier (Stanford Research Systems SR-830).

A Golay cell is the most sensitive device capable for room temperature THz detection and, in order to measure the amount of CW power produced in a nonlinear process, represents the only viable alternative to bolometric detectors, operating at the liquid helium temperature. Basically, it consists in a pneumatic chamber filled with gaseous Xenon, limited one one side by an absorbing film and, on the opposite one, by a flexible mirror. When the incoming radiation is absorbed by the film, it induces a thermal expansion of the gas medium deforming the flexible mirror on the backside of the chamber. This deformation is revealed by a optical beam focused on the mirror and backward reflected on a photodetector. A Golay-type detector is capable for revealing radiation in a broad spectral range, going from 0.1 THz to the near-IR. Calibration measurements, performed on our detector (Tydex GC-1P) by measuring the power radiated by a QCL operating at 2.5 THz, provided a responsivity of 20 kV/W for 10 Hz amplitude modulation fre-

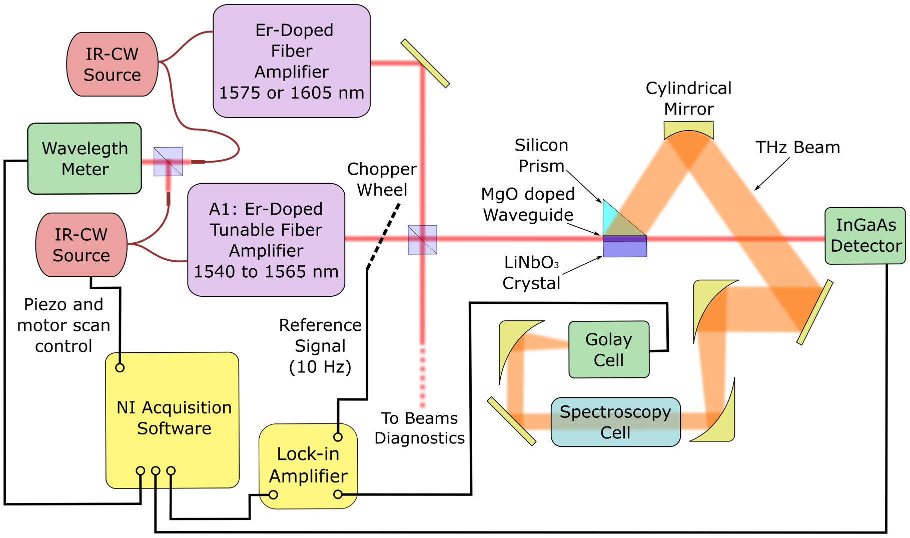

Figure 4.1: Schematic of the experimental setup for CW THz generation and spectroscopy.

quency. Such a value has been assumed to be valid for the whole THz spectral window, because of the flat response expected from the absorbing film. This assumption is supported by the fact that the responsivity we measured differs just for a factor 2 respect to the value provided by the manufacturer, being this latter one measured in the near-IR spectral region. On the other hand, the comparable response in the IR and THz ranges implies the need to filter out unwanted residuals of IR ligth coming from diffusion by the crystal facetes or extracted by tunneling from the guided mode. Such a spurious IR radiation could not only affect the measurement results, but also irreversibly damage the absorbing film, whose breaking threshold is of about 10 μW. For these reasons, a 1 mm thick black polypropylene (BPP) sheet has been used to screen the entrance window of the Golay-cell. Among the different materials, BPP is probably the one ensuring the best performances in filtering the IR radiation (measured attenuation of about 60 dB at 1.55 wavelength), showing at the same time a good transparency in the most of the THz spectral window. Indeed, the absorbtion profile of 1 mm thick PP filter was known from previous TDS measurements performed in the $0.1-4\ THz$ range, showing a flat transmittivity of 47% and an absobtion peak centered at 3.3 THz. For frequencies beyond 4 THz, to the best of our knowledge, no detailed spectral measurement have been performed yet. Anyway, as we will see soon, an estimation of the BPP filter transmission in the high frequency part of the THz spectrum has been possible by exploiting the CW radiation provided by our source itself.

Another technical difficulty arises from the strong power attenuation due to the absorption by atmospheric humidity. Indeed, more than fifty rotational transitions of water molecule lies in the 1-8 THz range, having, in some cases, a sufficient line-strenght to make, at the atmospheric pressure, the generated radiation practically undetectable. For example, the blue dotted trace of figure (4.2 a), acquired with a resolution of about 10 GHz/step, shows the power generated in the 5.2-6.5 THz frequency range and detected after 25 cm air propagation. As it can be seen, the water absorption line at about 6.15 THz reduces the measured power down to the nanowatt level, i.e. the minimum amount of power detectable by the Golay cell (having noise-equivalent-power of 10^{-10} W/Hz$^{1/2}$). In order to increase the amount of generated radiation available for spectroscopic applications, we have enclosed the LN crystal, the spectroscopic setup and the detector inside an isolated environment, consisting of a 100x60x40 cm^3 polyetylene box completely sealed except for two holes, which allow the pump beams propagation. A forced air flux, dried by a membrane filter, is injected within the box establishing a slight pressure gradient which vents out part of the wet air, leading to an significant reduction of the water absorption linewidth and intensity, visible in the red trace of figure (4.2 a).

The DFG process ensures the generated THz radiation to be coherent, spectrally pure (the THz linewidth is roughly twice the linewidth of the IR lasers, i.e. $< 100kHz$) and continuously tunable over a frequency range as large as allowed by the telecom sources. In order to continuously scan the whole accessible THz window, the laser diode D1 has been equipped of a motorized tilt of the external cavity grating, providing a nominal accuracy of 0.05 nm/step (6.2 GHz/step) during the wavelength scans. An automated system for wavelength adjustment and power recording has been implemented with a National Instruments DAQ and a LabView routine for remote control. Within the program, the parameters required for wavelength calibration are initialized at every restart by a subroutine containing a calibration data set, provided by the laser manufacturer.

Clearly, since the frequency scale calibration is a very delicate operation, an independent wavelength acquisition, performed by means of a wavelength meter, would be preferable. On the other hand, the wavelength meter acquisition time, required for this purpose, generally exceeds the scan temporization (tipically 3 s) fixed by the lock-in integration time. In order to define a correct measurement procedure, being compatible with reasonable acquisition times, we have compared the calibration dataset with an independent wavelength measurement. While this independent wavelength calibration confirmed the nominal value for the frequency-per-step coefficient to be sufficiently reliable for our purpose, the uncertainty on the initial positioning results to be larger than 10 GHz. In conclusion, this experimental check confirms the validity of the wavelength scale provided by the factory data-set, under the condition to correct the starting frequency by the value obtained

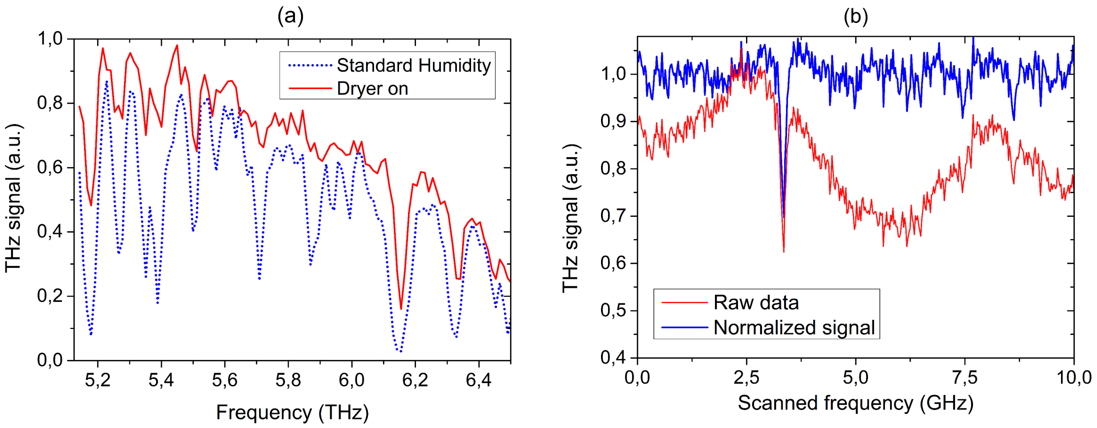

Figure 4.2: a) The effect of the atmospheric water absorption in two low-resolution frequency scans. Here the THz radiation has been collected after about 25 cm air propagation. b) Raw and normalized THz signal obtained in a 10 GHz high-resolution scan, performed adjusting the laser diode external cavity by means of a piezo actuator. In this example, the THz power has been recorded after pass through a spectroscopic cell filled with methanol vapours, responsible for the visible absorption dips.

with a direct measurement. Such a working hypothesis has been validated afterwards by comparing the the performed scans with the natural ruler provided by the water absorption lines.

In order to retrieve the nonlinear efficiency achieved by our CW source, the measured THz power has to be normalized to the product of the amount of IR power confined in the waveguide for each pump beam. In principle, one might think to get these two values independently by coupling one beam at the time with the waveguide and measuring the transmitted power. Unfortunately, such a procedure cannot be considered appropriate because, in an high energy confinament regime, the coupled power levels are not sufficiently stable in time, in particular during a frequency scan. Indeed, as discussed in section (3.2), the non zero reflectivity of the input and output facetes make the nonlinear crystal to behave as a Fabry-Perot interferometer. Now, despite the absorption losses can be considered negligible for the IR light that is coupled with the waveguide, the uncoupled power undergoes multiple reflections within the bulk crystal, leading, at these power levels, to a considerable amount of energy to be absorbed, slightly increasing the crystal temperature. Since the amount of time required for a full scan of the accessible THz windows is, typically, in the order of 15-20 minutes, a decreasing of the confined power due to the thermally induced crystal elongation appreciably affects the power of the generated THz radiation. Similarly, the etalon effect leads to uncontrolled, dramatic[2] power fluctuations as the pump laser frequency is continuously tuned. In order to avoid a step-by-step optimization of the coupled power, achievable with a fine adjustment of the voltage signal controlling the diodes external cavity length, we chose to implement a simple optical system providing a real-time monitoring of the pump power. For this purpose, a lens (5 cm focal length) is placed at the waveguide output, sufficiently far to not hamper the THz beam propagation but close enough to collect a small (but known) fraction of the transmitted IR power. Hence, a low reflectivity mirror is used to furtherly attenuate the collimated light and send it onto a fast detector, namely an InGaAs photodiode with 150 MHz bandwidth (Thorlabs PDA10CF-EC). If the chopper wheel is placed along a single pump beam, the photodiode detects a squared-wave signal representing the overall coupled power ($P_1 + P_2$) and the power of the unmodulated beam (for example P_2). For each step of the frequency scan, this signal is sampled by the DAQ system and the storaged data numerically elaborated in order to retrieve the single beams powers[3]. The normalization procedure has been applied both for the motor-controlled scans and the high resolution ones, performed by finelly adjust the external cavity length and described in details later in this chapter. An example of such a scan[4] is shown in figure (4.2 b). The red trace represents the raw THz signal, directly measured by the lock-in amplifier, and exhibits an evident periodical modulation (with about 5 GHz period) due to the Fabry-Perot transmission profile. The blue trace in figure, instead, shows the normalized THz power retrieved through the numerical elaboration of the of the photodiode signal measured at the waveguide output.

Spectral coverage, output power and nonlinear efficiency

The generation bandwidth achieved by our CW THz source has been investigated by varying the D1 wavelength along the whole operational bandwidth of the A1 amplifier. Remarkably, this can be done with a single scan for each one of the two possible arrangement of the fiber amplifiers. Indeed, no variation in the optical alignament is needed as the frequency is changed, because the Cherenkov PM scheme requires collinear prop-

---

[2] Here we remind that the transmission fringes are characterized by a T_{max}/T_{min} ratio of about 1.6 .

[3] The first part of the numerical array, correspondingly to the first 1s acquisition time, is excluded to the data analysis in order to avoid transient effects affecting the measurement. The remaining data are ordered by value and splitted in two halfs, each one deprived of the first and of the last points and averaged in order to get the values of $P_1 + P_2$ and P_2. This second elimination is done in order to exclude the spurious data accidentaly acquired during the square-wave commutation.

[4] This scan, presented by way of example, refers to a measurement performed on a low pressure methanol gas sample. For this reason the absorption dips, visible in figure, may not be attributed to the atmospheric vapours absorption but to rotational transition of the methanol molecule.

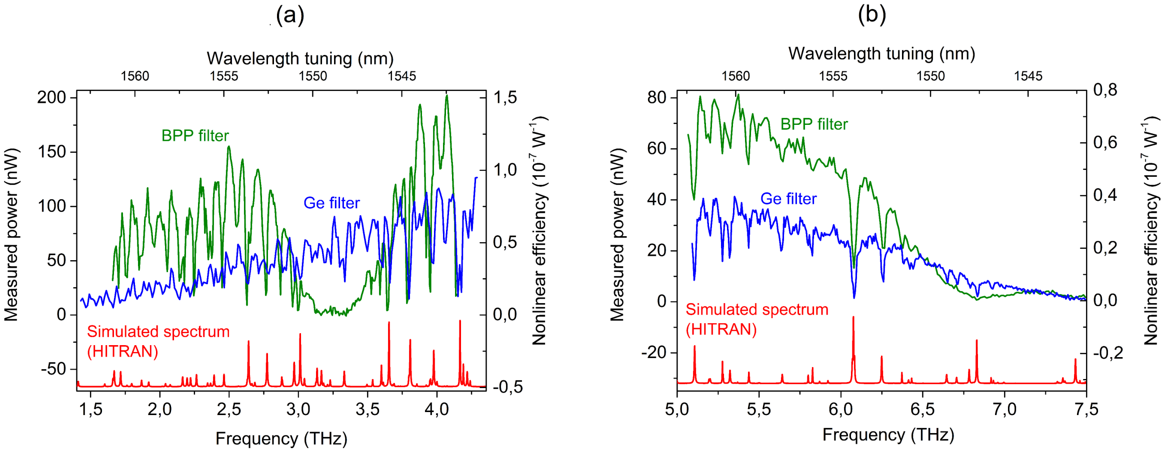

Figure 4.3: Long range scan in the low-frequency part of the THz spectral window compared with the calculated water spectrum (red). This measurements has been obtained by varying the wavelength of the D1 laser diode within the 1540-1563 nm range. The wavelength of the D2 laser diode, seeding the A2 (a) or the A3 (b) amplifier has been fixed at 1575 nm and 1605 nm respectivrly. The green and the blue traces coreespond to the different filters used to protect the detector, being made of black polypropylene and germanium respectively.

agation for the IR beams. Regarding to the low frequency part of the acievable THz spectrum, an example of such a long run scan is given in figure (4.3 a). Green trace have been obtained varying the D1 wavelength between 1563 nm and 1542 nm with a 0.1 nm step, while the laser diode D1, seeding the A2 amplifier, has been fixed at 1575 nm. A comparison between the experimental data set and the water absorption spectrum, calculated on the basis of the parameters available on HITRAN database (the red trace in figure) provides a further countercheck of the frequency calibration. As previously explained, in a single-shot frequency scans the acquisition system normalizes the measured THz power to the product P_1P_2 so, stricktly speaking, the experimental curve represents the efficiency spectrum. In order to convert the vertical scale to power units, we acquired the emitted power for different selected points along the whole frequency range of interest. These frequency values have been chosen to be far away from the water absorption resonances, while the IR coupled power, and therefore the THz power, has been point-by-point optimized by a fine frequency adjustment. The generation mechanism is not responsible for the dramatic power drop visible between 2.5 THz and 3.6 THz. Oppositely, it has to be attributed to the BPP filter used for IR filtration, having an absorption resonance at 3.3 THz, as already known from TDS measurements performed by R. Torre and co-workers (unpublished results). Taking into account of the 47% transmission co-

efficient in the rest of the considered bandwidth, a maximum of 200 nW of THz power available for applications has been measured at about 4.1 THz. This value, corresponding to 2.4 W of IR power confined in the waveguide, distributed in 1.5 W from A1 and 1 W at 1575 nm, leads to a nonlinear efficiency of $1.5 \cdot 10^{-7}$ W^{-1}. A further frequency scan, performed substituting the BPP film with a 1 mm thick germanium filter, is shown in figure (4.3 a) in order to demonstrate CW THz radiation to be continuously generated along the whole spectral region of interest. Moreover, since germanium has a flat transmission coefficient in this range (about 0.25%), negligible distortion in the generation spectrum have been introduced in this measurement.
If the achieved efficiency is surely one of the most satisfactory results of our experimental work, the achieved spectral coverage is even more so, demonstrating a wide region of the THz spectral window, currently precluded to the most diffused CW emitters, to be accessible thanks to the waveguided approach. In order to demonstrate this, a frequency scan obtained by substituting the A2 amplifier with A3, operating at 1605 nm wavelength, is shown in the green trace of figure (4.3 b). Also in this case the IR radiation seeding the A1 amplifier has been tuned in the 1542-1563 nm wavelength range (with a 0.05 nm/step) and the Golay cell has been screened with the 1 mm thick BPP filter. For this amplifiers arrangiament, the overall optical power coupled with the waveguide is 2.27 W, being distributed in 1.5 W from A1 and 0.7 W at 1605 nm, a maximum power of 80 nW at 5 THz has been measured, corresponding to $0.8 \cdot 10^{-7}$ W^{-1} nonlinear efficiency. Since we do not dispose of the BPP absorption spectrum for this spectral range, the filter transmission has been measured simply by acqiring the THz signal with a further identical one placed before the sensor. Anyway, such a procedure provides valid results only up to 6 THz, confirming about the 47% of the THz radiation to be transmitted, while for higher frequencies an accurate extimation is hampered by the poor signal to noise ratio. The slight reprise of the THz signal at about 6.9 THz, barely visible in the green line of figure (4.3 b) suggested us the power falling to be ascribed to the filtration mechanism. Indeed, as it can be seen in the blue trace in figure, an identical scan performed with a germanium filter definetly clarifies that CW THz generation is accomplished up to 7.3 THz.

The experimental realization of a CW source, capable for room temperature generation of THz radiadiation in a 3 octave frequency span, is undoubtebly a remarkable result. Nevertheless, the absolute power levels we have so far recorded, although sufficient for room temperature detection and corresponding to nonlinear efficiencies uncommonly high, seem to be almost one order of magnitude lower than the ones required in modern spectroscopic technique. Power levels being, at least, in the microwatt range, could be possible in principle by tripling the power of the IR pump source. By the way, even if we are not able to exclude such an approach to be sucessfull, the prospect of indefinitely up-scaling the pump beams intensity seems to be fairly unrealistic in the waveguided scheme. A much more reasonable strategy could be, instead, to triple the propagation length within the nonlinear material. Such an approach has already been demonstrated to be usefull in the pulsed regime, in which K. Kawase et al. have been implemented Cherenkov generation of optically rectified THz pulses by exploiting a 7 cm long LN crystal [83]. In any case, in order to get some advices about the possible room for improvements, we owe to compare our experimental results with the expected ones. For this purpose, nonlinear efficiency has been calculated as a function of the THz frequency by numerical integration of the relation provided in the second chapter of this thesis over the emission angles. The angular dependence of the emitted power has been included in the transverse components of the THz wavevector, in the Fresnel losses occurring at both the interfaces and in a multiplicative term $sin^2\phi$, assumed for analogy with a linear dipole emission. The angular integration has been performed within the range allowed for transmission across the prism-air interface, being this limited by the critical angle determed by the Snell law for the LN-air surface. In order to correctly reproduce the spectral profile of the measured efficiency, frequency dependence of several important parameters has been taken into account. In particular dispersion curve for MgO:LN has been obtained assuming the Sellmeier equation to be valid in the whole 1-8 THz spectral window, while the absorption spectrum of both silicon and germanium have been retrieved from experimental data available in litterature[5]. Anyway, silicon absorption spectrum, available on THz-bridge spectral database, suggests the prism not to be responsible for the high frequency limitations of our source, because the absorbption coefficient is practically constant at the value of 0.35 cm^{-1} in the whole 5-8 THz range. Oppositely, a dramatic decreasing of the germanium trasmittivity in the considered range is expected [124] and, hence, it has been considered in simulations. Regarding to the guided mode dimensions, the measured parameters of section (3.2) have been used for calculations but, given the asymmetric profile in the y direction, we have assumed for simplicity the IR light to be confined in a symmetric gaussian distribution having the same area. The numerical results of such a calculation is reresented by the red dashed line in figure (4.4). Despite the abundance of the considered parameters, a significative gap between the predicted values and the measured one can noticed. Such a discrepancy cannot be explained by an accidental mistake in the adimensional multiplicative constants (although it is possible). Indeed, as can

---

[5] Particularly regarding to the THz propagation within the silicon prism, we have taken into account the different path length l for waves generated at different point along the waveguide. For this purpose, we have assumed the generation efficiency to be uniform along the x direction and the attenuation factor has been calculated as $\Sigma_{Si}(\omega) = \frac{1}{L}\int_0^L exp(-\alpha(\omega)l(x))dx$.

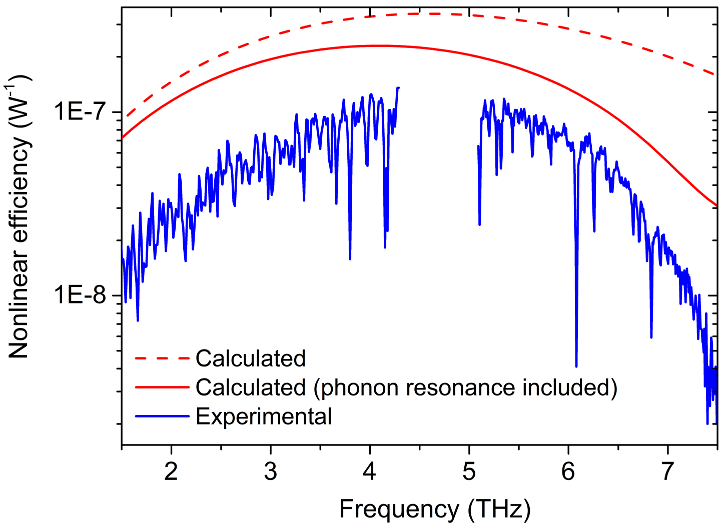

Figure 4.4: In blue the experimental nonlinear efficiency curve compared with the theoretical predictions. The dashed red line represents the simulation performed neglecting the absorption contribution due to the TO phonon resonance at 7.6 THz. This effect, included in a second time, is visible in the solid red curve.

be seen in figure (4.5), while the mesured efficiency peak positon is in good agreement with the calculations, unexpected cut-off frequency is visible in particular in the high part of the generation bandwidth. In order to understand the observed behaviour, THz absorption by LN crystal, neglected at first because of the very small thickness crossed by the generated radiation, has been taken into account in the simulation, leading to a significative approach between the predicted and the observed efficiency, visible in the solid red line of figure (4.4). Remarkabely, the absorption profile of LN is dominated by a transverse optical (TO) phonon resonance centered at 7.6 THz, being strongly dependent on crystal temperature and doping concentration. In order to give a reliable extimation of such effect, the absorption coefficient has been calculated following the approach suggested by H. J. Bakker et al. [125] and interpolating the numerical data with the measured values provided by M. Unferdorben et al. for 6.1 %MgO-doped congruent LN at room temperature [126]. Anyway, numerical results, still underestimating the observed cut-off, are probably affected by the lack of information about the local temperature and, ence, have to be prudently considered. For completeness, we would to stress out that another factor could be responsible both for the overall efficiency and the high frequency damping. Indeed, in case the optical contact between the waveguide surface and the silicon prism is not perfectly estabilished, and a thin air gap Δ is present, requirements for THz estraction are no more fullfilled. In such a condition, however, an evanescent THz wave can be outcoupled but it results attenuated by an exponential factor $e^{-\Delta/\Lambda}$, depending on wavelength through the term

$$\Lambda = \frac{\lambda}{2\pi n_T}\sqrt{cos^2\theta_c - (1/n_T^2)}. \tag{4.1}$$

For this reason, despite the THz wavelengths are typically very much larger than a reasonable gap, the elevate difference in the refractive index make the 1/e attenuation length Λ to be smaller than 1 μm just beyond 3.5 THz. It must be said, however, that an air gap as wide to justify the observed high frequency cut, i.e. few hundereds nanometers, would imply an appretiable red-shift of the efficiency peak, making the experimental results hard to be interpreted.

In conclusion, the previous analysis suggests the desired improvements, both in terms of absolute THz power and spectral coverage, to be possible by a further optimization of few different parameters. Noteworthely, in our opinion the most of them regards, not the generation mechanism itself, but the THz estraction. In particular, it would appear from the available informations that thermo-electric cooling, needed to reduce the phonon induced absorption, and a proper optimization both in the shape and the optical contact of the silicon prism to be indicated as the main factors to be optimized. Working on these parameters we can reasonably hope, for the next future, to reach a significative broadening of the generation bandwidth and output power levels approaching the microwatt range.

4.2 High resolution spectroscopy

As we have just seen, the THz source we have implemented allows access to a THz spectral range usually precluded to the CW emitters commonly employed in spectroscopy. Moreover, the fact that it is entirely based on robust and reliable telecom technology, and it is potentially scalable to relatively compact dimensions, leads us to hope it will plays a key role for THz frequency measurements, particularly beyond 5 THz. However, before we can aspire it, we need to demonstrate that the spectroscopic performances of the source are competitive with the existing ones. For this purpose, we carried out several tests on a gaseous methanol sample.
Methanol (CH_3OH) is a simple asymmetric molecule possessing internal rotational degrees of freedom, namely hindered rotations (torsion) of the OH group respect to the CH_3 group. Its Hamiltonian, described extensively by M. R. Lees and J. G. Baker [127], can

be separed into the sum of three terms, two of them corresponding to the symmetric and asymmetric rotor contribution and the third representing the torsional part. The energetic levels can be labeled by six quantum numbers, corresponding to the symmetry group, the vibrational state (v), the torsional state (n) and the three quantum numbers associated to the angular momentum J, M and K. J is the quantum number associated to the total angular momentum, while M and K represent the its components respectively along a fixed direction and along the methyl axis.

Since methanol belongs to the C_8 symmetry group, the quantum number representing the symmetry group can be labeled as A, E_1 and E_2. Anyway, since no transitions are allowed betwen different symmetry species, these labels will be omitted in the state notation. Similarly, M will not be considered because, in absence of external applied field, the energy levels are completely degenerate respect to it. Furthermore, all the molecular transitions lying in the THz spectral range occur between rotational sublevels of the vibrational ground state or, in few cases, of the first excited state of the $C-O$ stretch vibrational mode. In any case, none of them involves variations in the quantum number v. For these reasons, in the following the molecular states to be considered we will be indicated as (J, K, n).

A wide catalogue of calculated and measured THz transitions of the methanol molecule is currently available at the Jet Propulsion Laboratory (JPL) molecular database as well as in several papers [128]-[130]. The measured transition frequencies have been mostly measured by means of Fourier transform spectrometers and TuFIR lasers, while for the <4 THz range a significative contribution has been provided by QCLs based messurements, allowing, in some cases, to show evidence of saturation effects [131]. Since we do not dispose yet of an absolute frequency scale, in the following we will extensively take advantages of the available data to retrieve a figure of merit of the spectroscopic capabilities of our source. Two aspects in particular will be stressed, i.e. the mode-hop free tunability range and the relative precision in the line-center determination.

Mode-hop free tunability range and relative precision

A simple direct-absorption spectroscoy setup has been implemented. For this purpose, the shape of the collimated THz beam, having about 1x2.5 cm^2 dimensions, has been adapted in order to fit the cell containing the methanol gas, constituted by a 12 cm long aluminium cylinder having a clear aperture of 1.5 cm diameter. A couple of parabolic mirrors, having respectivelly 7.62 cm and 2.54 cm focal length and placed after the cylindrical mirror, reduce by a factor of 3 the transverse dimensions, while a third parabolic mirror focuses the transmitted radiation on the Golay detector. In such experimental conditions the optical path in air was about 40 cm and, therfore, the power losses due to the water absorption is sensibly increased with respect to the previously described measurements.

Since further unavoidable absorption is introduced by the spectroscopy cell windows, we decided to avoid the usage of germanium as a protective filter and focus our attention on few selected spectral regions, being reasonabely far from both water and BPP absorption resonances. Precisely, the spectroscopy cell has been sealed with two different windows, respectively constituted by BPP (1 mm thickness) and TPX (2 mm thikness), having 37% overall transmission. By doing so and by isolating in an opaque box the THz path from the cell to the detector, no additional protection has been placed before the sensor.

When a laser beam of a given intensity I_0 passes through an absorbing material, the optical power density I, measured after a path L within the sample, is reduced according to the Lambert-Beer law:

$$I = I_0 e^{-\alpha(\nu,p,T)L} \tag{4.2}$$

where $\alpha(\nu, p, T)$ represents the absorption coefficient and, for a gas sample, results from the convolution of a temperature-determined Gaussian profile (the Doppler contribution) with a Lorentzian term that takes into account the collisional broadening.

Pressure in the order of 10^{-6} Pa have been obtained by connecting a turbo-rotative pump (Pfeiffer vacuum) at one end of the spectroscopy cell while, on the opposite side, a needle valve allows to regulate the exact amount of methanol vapour to be inflated. The pressure stability, continuously monitored by a thermocouple gauge tube, have been measured in time, demonstrating the pressure drifts to be less than 1% in an hour.

Since the typical frequency separation between the different methanol rotational transitions is in the order of hundereds of MHz, high resolution measurements cannot be accomplished by the motor-controlled system used for the long range scans. For this reason, in this set of measurements the continuous adjustment of the pump beam frequency, and therefore of the THz emission, has been achieved by using a piezoelectric control of the diode external cavity. The temporized DC signal, driving the piezo actuator, is generated by the NI-DAQ system and can be adjusted with a 25 mV /step resolution within the 0-150 V range.

In order to determ the contunuous tunability range of our source, several long-run scans have been performed along the whole generation span. An example of such scans, performed with a resolution of 0.1 V/step with a methanol vapor pressure of 200 Pa, is shown in figure (4.5 a). Here, a precise line pattern has been identified by retrieving the transitions frequencies from the measurements of the pump beam frequencies provided by

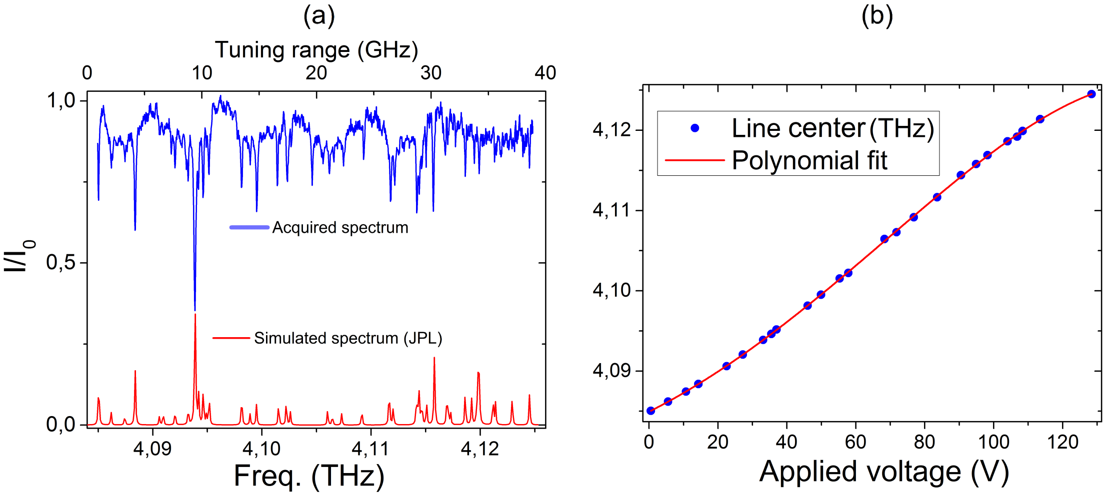

Figure 4.5: a) 40 GHz continuous mode-hop-free scan performed on 200 Pa methanol vapors around 4 THz. b) Polynomial fit of the line center positions (available on JPL molecular database) as a function of the applied DC voltage signal driving the piezo scan.

the wave meter. The measured values have been confirmed by a one-to-one comparison between the experimental data and the methanol spectrum, calculated on the basis of the parameters available from the JPL molecular database (red line in figure 4.5 a).
Similar measurements have been performed along the whole generation bandwidth. Anyway, the spectral region around about 4.1 THz, being sufficiently far from water resonances and characterized of plenty methanol transitions, is particularly suited to demonstrate 40 GHz mode-hop free operation provided by the source. Indeed, the first and the last absorption dips, visible in the blue trace of figure (4.6 a), respectively correspond to the transition $(J, K, n) = (18, -7, 1 \rightarrow 19, -8, 2)$ at 4.085 THz and $(J, K) = (15, -5, 1 \rightarrow 15, -4, 2)$ at 4.125 THz. All the line centers have been assigned and related to the amplitude of the DC signal used to tune the diode external cavity, allowing a precise calibration of the frequency/voltage curve, as shown in figure (4.5 b).

In order to retrieve the calibration coefficient to be used in the single-line frequency measurements, the DC signal steps has been reduced to 25 mV/step, providing an overview on different line groups with higher resolution. For example, in figure (4.6) two different line groups, respectivelly at about 2.5 THz (a) and 4.1 THz (c), have been resolved for a gas pressure of 200 Pa and compared with the calculated spectrum. The graphs of figure (4.6 b and d) demonstrate that a linear frequency tuning can be safely assumed in scans wide up to 5 GHz. The measured linear calibration coefficient results to be (245 ± 1)

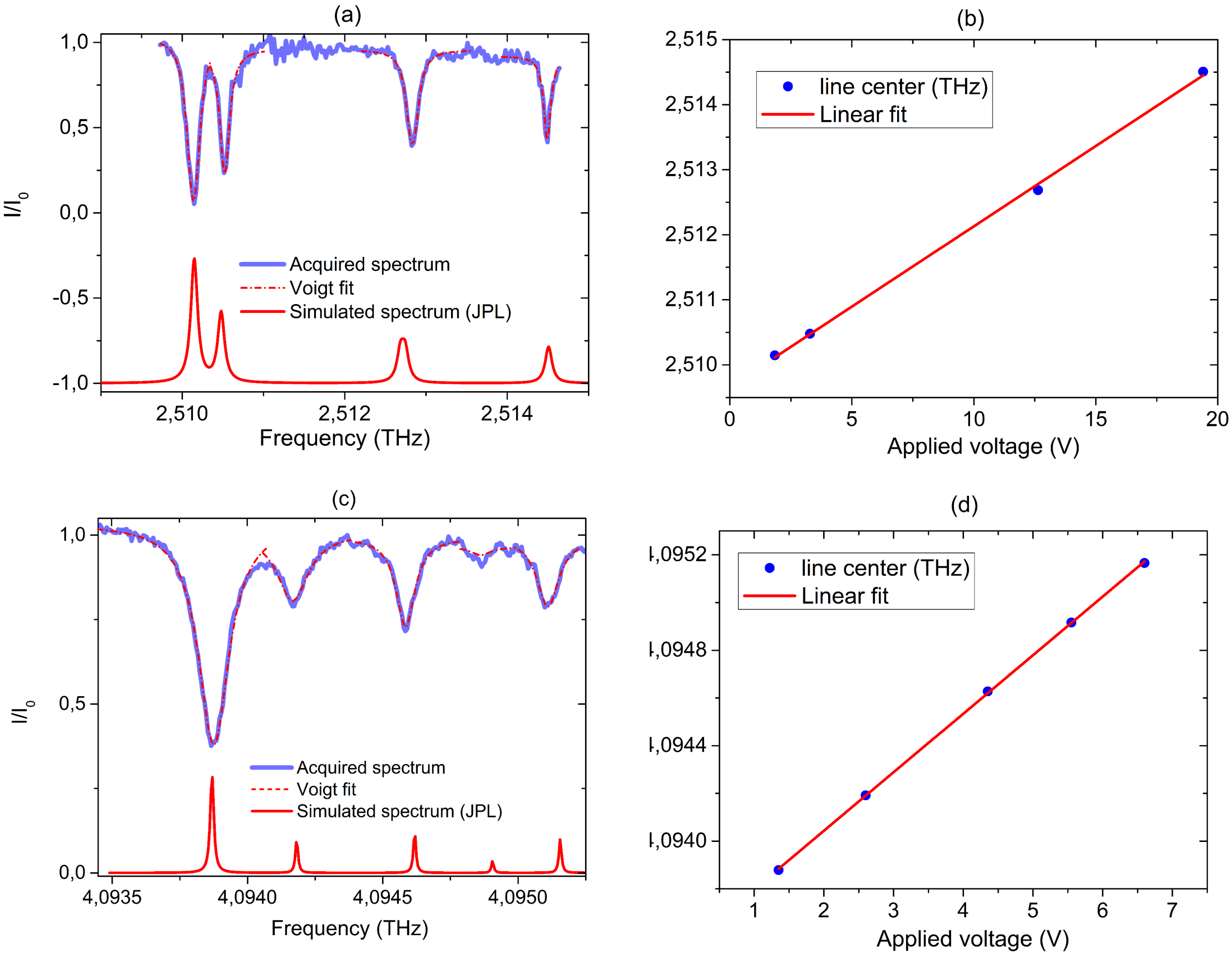

Figure 4.6: 0.025 V/step resolution scan at 2.5097 THz (a) and 4.0935 THz (c) compared with the simulated spectrum (from JPL molecular database). Linear calibration of the piezo scan between 2.5097 and 2.5146 THz (b) and between 4.0935 and 4.0955 THz (d). In both the cases the calibration coefficient results 245 MHz/V.

MHz/V for all the considered line patterns.

In order to investigate the spectroscopic capabilities of our CW source, different lineshapes have been acquired as a function of the sample pressure. Here we will focus our attention on the $(14, 6, 1) \rightarrow (15, 7, 1)$ transition at 4.094 THz, whose profile has been measured at 295 K temperature for different pressure values, from 230 Pa down to 20 Pa, with a 2.45 MHz/step resolution. In these experimental conditions the transmission profile, shown in figure (4.7 a) as a function of the frequency displacement respect to the line centre ν_c, is the result of two distinct contributions. On one hand, the inhomogeneous line broadening due to the Doppler effect leads to a gaussian-shaped profile, with full width at half maximum W_D depending on the gas temperature according to the relation

$$W_D = \frac{\nu_c}{c}\sqrt{\frac{8ln2\ k_B T}{m}}, \tag{4.3}$$

where k_B is the Boltzman constant and m is the molecule mass. Doppler line-width calculation, performed with the actual parameters, provide in our case the value of $W_D = 8.89$ MHz. On the other side, collisional broadening, whose contrubution is expected to be proportional to the gas pressure, is dominant in almost all the considered measurement. For these reasons, in the data analysis we have generally considered a Voigt profile, resulting from the convolution of the Doppler line-shape and the Lorentzian one resulting from the collisional contribution. The experimental traces of figure (4.7 a) have been fitted with the function

$$\alpha L = C - \frac{A\ 2ln2\ W_L}{\pi^{3/2} W_D^2} \int \frac{e^{t^2}\ dt}{\left[\frac{2\sqrt{ln2}(\nu-\nu_c)}{W_D} - t\right]^2 + \left(\frac{\sqrt{ln2}W_L}{W_D}\right)^2}, \tag{4.4}$$

where W_L is the full width at half maximum of the Lorentzian profile, while C is an adimensional constant and A, expressed in MHz, represents the area within the absorption dip. The tail of a second absorption line, centered about 366 MHz apart from the considered line is responsible for the asymmetric profile of the measurement at 230 Pa (orange line in figure). In this case, a multiple-peak Voigt fit has been used in order to retrieve the parameters.

Except for the measurement at 20 Pa, the collisional broadening is largely dominant and the Voigt fit results are fully compatible with the values provided by a lorentzian fit. The linear dependence of the W_L parameter on the sample pressure is shown in figure (4.8 b). As it can be seen from the graph, the collisional contribution to the absorption linewidth is, as expected, proportional to the gas pressure, being the coefficient (517 ± 13) kHz/Pa.

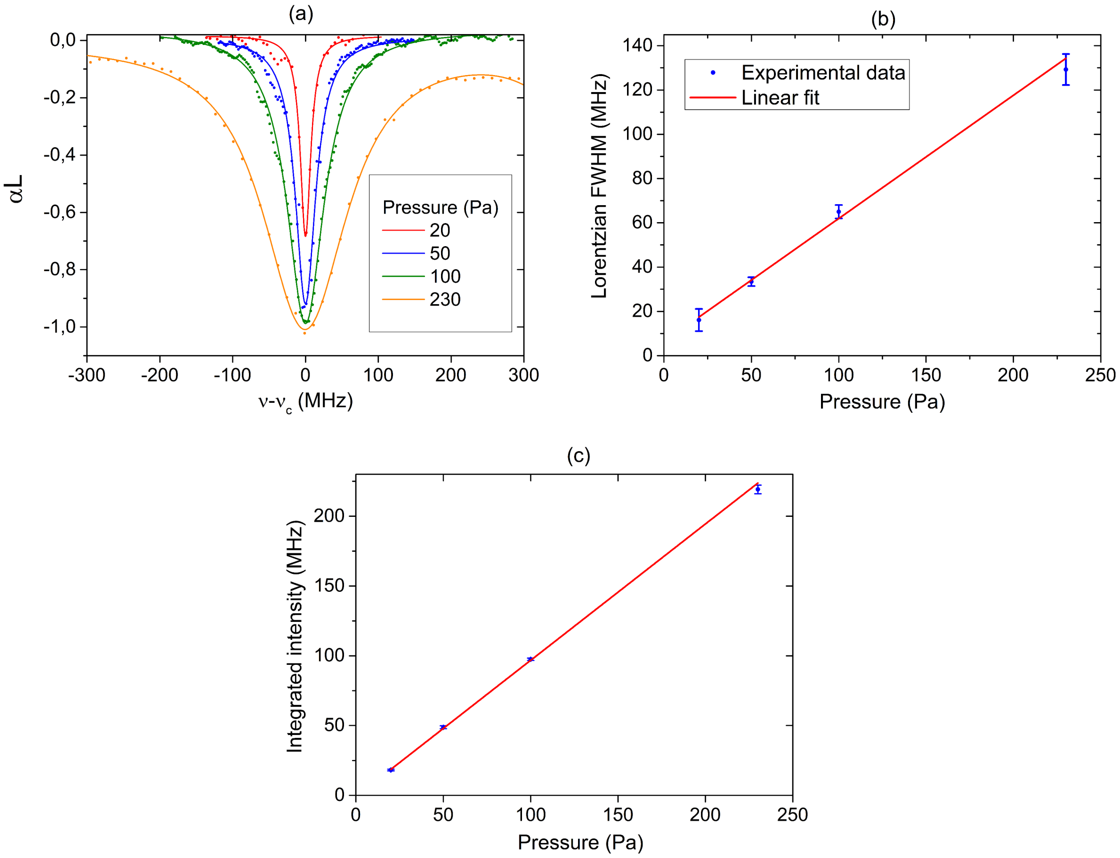

Figure 4.7: a) Transmission profiles as a function of the frequency displacement respect to 4.094 THz. The experimental data, acquired for different values of the methanol gas pressure, have been fitted with a Voigt function. Figures b) and c) represent respectively the full width at half maximum of the Lorentzian contributions and the integrated area within the absorption profiles as a function of the gas pressure. All the measurements refers to a gas temperature of 295 K.

Regarding to the Doppler linewidth, it has been retrieved by the vanishing pressure extrapolation of the linear trend, resulting to be (8.2 ± 1.3) MHz, being compatible with the expected value.

The transition linestrength S, defined in terms of the transition cross section by the relation

$$\sigma_{ki}(\nu, P, T) = S_{ki}(T)\, g(\nu, P, T), \tag{4.5}$$

has been obtained on the basis of the fit parameters. In the previous equation the labels k and i refer respectively to the lower and the upper level involved in the transition, while $g(\nu)$ represents the normalized line profile. Accordingly to this definition, the linestrength can be retrieved on the basis of the integrated cross section, i.e. dividing the integrated area A by nL, where n represents the number of molecules in the unitary volume. The proportional scaling of the integrated intensity with the increasing gas pressure is shown in figure (4.7 c). The linestrength, obtained by multiplicating the slope of the linear fit by $k_B T/L$, results to be, for the considered transition, $(32.6 \pm 0.7) \cdot 10^{-3}$ MHz nm^2.

The final and most significative aspect we want to discuss regards the achieved relative precision of the spectrometer. Since the primary IR lasers has not yet been refered to a frequency standard, at this stage the source is not capable for providing absolute frequency measurements. However, the spectroscopic tests we are going to discuss demonstrate that the relative precision on the line center determination is of the order of few part in 10^{-8}, that is comparable with the performances of some of the most precise currently available spectrometers. In these tests, the methanol vapor pressure has been reduced down to few tens Pa, thus approaching the Doppler limit condition for methanol's profile width. At the same time the scan resolution has been increased by reducing with a 1:100 voltage divider the DC signal driving the piezo actuator.

Figure (4.8) shows two methanol transitions, the first at 4.094 THz, the second at 5.573 THz, lying in the two distinct bands covered by the two different fiber laser amplifiers combinations. An integration time of 3 seconds has been chosen as the best compromise between a reasonable signal-to-noise ratio and an overall measurement time short enough to neglect the thermal drifts of the nonlinear crystal and the variations in the molecular gas sample pressure. In both cases, the normalized transmitted intensity I/I_0 is plotted as a function of the frequency displacement with respect to the central frequency ν_C. Even in this low pressure regime, collisional broadening cannot be neglected, and it was retrieved by fitting the experimental points with the Voigt profile. The absorption profile shown in figure (4.8 a) refers to the same rotational transition at 4.094 THz just described . Here, in the fitting procedure we have taken into account a second weak absorption, provid-

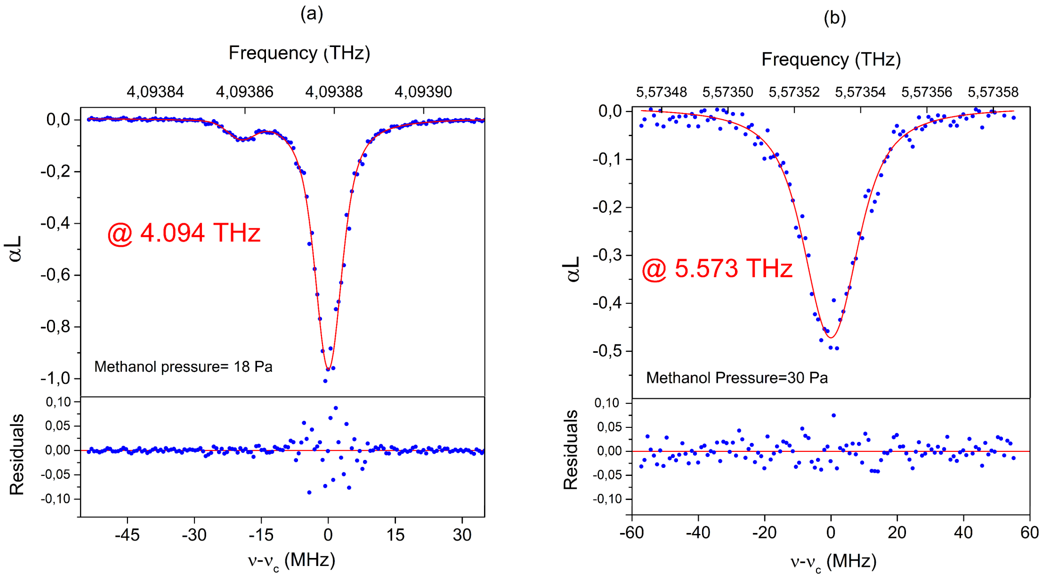

Figure 4.8: Absorption profiles at a) 4.0939 THz and b) 5.5735 THz are reported, together with the Voigt fit profiles and residuals (lower panels).

ing an uncertainty on the line center frequency $\Delta\nu_C = 33$ kHz and a relative precision $\Delta\nu_C/\nu_C = 8.06 \cdot 10^{-9}$. The second absorption profile, presented in figure (4.8 b), refers to the transition $(J, K, n) = (4, 4, 2) \rightarrow (5, 5, 1)$ at 5.573 THz. The slightly worse signal-to-noise ratio achieved attributed to the larger residual water vapor absorption present at this frequency. The uncertainty on the line center determination results to be $\Delta\nu_C = 178$ kHz, giving a relative precision of $\Delta\nu_C/\nu_C = 3.10 \cdot 10^{-8}$.

Despite constituting a preliminary result, some important conclusion can be drawn from the measurements discussed in this chapter. Indeed, if compared with the performances of the commonly used THz devices, they demonstrate our source to possess an extraordinary flexibility, being able to provide ultra-wide frequency scans as well as very high precision in spectroscopic mesurements. In particular, the capability to generate THz radiation well beyond 4.5 THz, currently limiting the achevable bandwidth of the CW THz QCLs, has been demonstrated. On the opposite limit the DFG approach, transferring in the THz range the tuning accuracy available in the IR spectral region, leads to extremely high resolution performances in spectroscopic measurements, demonstrating the relative precision on the line center identification to be of the same order of magnitude of the most accurate spectroscopic measurements so far performed.

Remarkably, at this stage two distinct contributions seem to limit the signal to noise ratio of our experimental data, namely the detection noise and the frequency fluctuations of the IR sources. For this reason, the final part of this work has been dedicated to the frequency stabilization of our spectrometer obtained, as it will be discussed in the next chapter, by phase locking the primary IR lasers to a stable radio frequency oscillator. As we will see, similar spectroscopic tests will demonstrate considerable improvements arising from this further upgrade, leading to the highest possible precision achevable in a Doppler limited spectroscopic measurement. Furthermore, the accomplishment of a frequency locking setup represents also a fundamental step towards absolute frequency measurements.

5

Source stabilization

5.1 Frequency locking scheme

Typically, the frequency stabilization of a laser source is achieved by an active control loop formed by two consecutive steps. At first the free-running frequency must be compared with a much more stable reference signal. Then the frequency fluctuations have to be properly corrected through a feedback signal driving the laser emission. In order to make these fluctuation to be detectable, the IR radiation emitted by our laser diodes must be converted into a radio frequency (RF) signal that is then compared with a local oscillator (LO) provided, for instance, by a 10 MHz quartz oscillator. Such a frequency conversion can be accomplished by generating a beating, whose frequency will be indicated as ν_{beat} in the following text, between the CW radiation and one of the teeth of a mode-locked (ML) laser. The two frequencies, hence, will be related by the simple equation

$$\nu_{CW} = \nu_{ceo} + N\nu_{rep} + \nu_{beat}, \tag{5.1}$$

where N is an integer number labeling the tooth of the ML laser being closest to the CW frequency. Since in our case $\nu_{rep} = 100$ MHz, the frequency of the beat note will be comprised within the 0-50 MHz frequency span. It must also be noted that, unlike the other terms of the previous equation, ν_{beat} may assume both positive and negative values depending on the frequency of the free running source, which can be larger or smaller than the one of the nearest tooth.

From this equation it can also be seen that, once the beating frequency will be locked to the local oscillator, the stability of the IR sources will still be limited by the slight frequency jitter affecting both the repetition rate and the carrier-envelope offset. By the way, it is also clear that, regarding to the THz frequency to be generated, the repetition rate is the only parameter really requiring a further stablilization, being the ceo frequency perfectly cancelled by the DFG process:

$$\nu_T = \nu_{Cw1} - \nu_{CW2} = (N_1 - N_2)\nu_{rep} + (\nu_{beat1} - \nu_{beat2}). \tag{5.2}$$

Note that also the term containing the difference of the beat notes frequencies can be cancelled by locking both of them to the same reference signal, while the quantity $N_1 - N_2$, being constrained to integer values, can be unambiguously be assigned by calibrating the THz frequency with a molecular transition whose frequency is known with a <100 MHz accuracy.

Despite remarkable increasing in the relative precision of spectroscopic measurements can be demonstrated even with a free running repetition rate (see section 5.2), the natural evolution of the present experimental work will be referencing of ν_{rep} to a primary frequency standard. By so doing, not only the stability of the THz spectrometer will be increased, but also also open the way to absolute frequency measurements. Unfortunately, at the present moment this final step has not been taken yet. A brief discussion of the improvements we plane to make in the near future in order to give a fully metrological capability to the presented spectrometer will be given in section (5.3). In the following sections, instead, we will describe the experimental setup designed to produce the beat note signal and the electronic loop processing it and generating the feedback signal.

Optical setup

A schematic picture of the optical setup implemented for the stabilization of the primary IR radiation is given in figure (5.1). A train of equally spaced IR pulses is provided by the ML laser, described in the third chapter of this thesis. The s-polarized beam is divided by a non-polarizing beam splitter (NP-BS). The CW radiation provided by each one of the seeding laser diodes is divided by a 90-10 fiber splitter. While the 10% is sent to the erbium-doped fiber amplifiers to be employed in the DFG generation process, the 90% is properly collimated, sent to a polarizing beam splitter (P-BS), and overlapped to the ML laser emision. An half-wave plate, positioned before the P-BS, ensures that the CW beams are mainly p-polarized, with only a small s-component that is reflected and sent to a wavelength meter (not shown in figure) for an accurate monitoring of the emitted frequency. In this way, we obtain two distinct optical paths, each one being composed by the single frequency radiation to be stabilized and one half of the pulsed one.

Among the several teeth composing the ML laser spectrum, only the closest to the CW laser frequency has to be detected in order to generate a RF signal. All the remaining

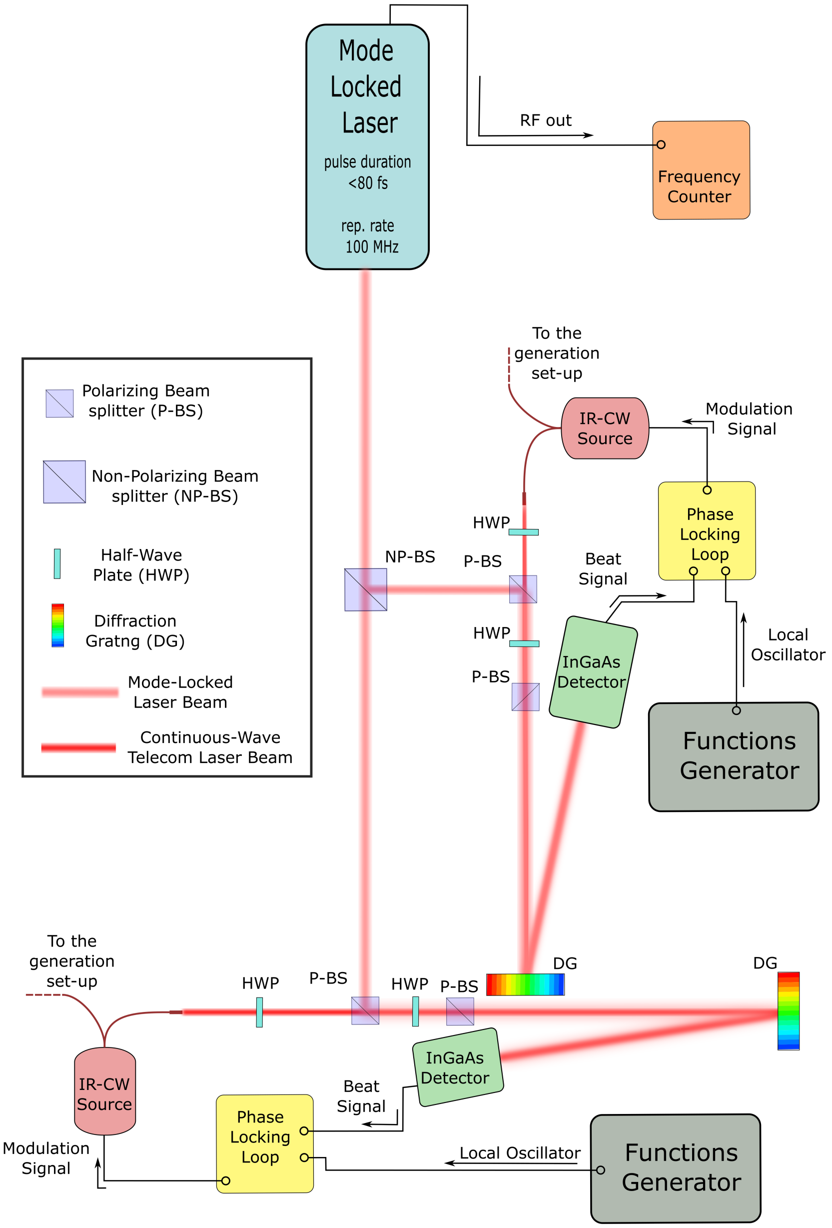

Figure 5.1: Schematic of the experimental setup for the stabilization of the pump and signal frequencies.

ones, each one generating a unusefull replicas of the beat note signal beyond 50 MHz, have to be filtered out as much as possible. Indeed, if the whole spectral content would be revealed, an overall attenuation of the optical intensity, compromising the desired RF signal, would be needed in order to prevent the saturation of the detector. In order to avoid this, each of the two optical branches are sent to a diffraction grating, mounted in Littrow configuration in order to maximize the power transferred into the first diffraction order. The back reflected beams is therefore spatially dispersed and, hence, the undesired spectral components can be blocked by an adjustable aperture.

Before to be focused on a fast InGaAs photodiode (Thorlabs DET10C), the beams pass through a polarizer, selecting the p-polarized component of both the CW and the pulsed radiation. A half-wave plate, placed before the polarizer, allows the power in the p-modes to be properly balanced and, hence, the beating signal to be maximized.

The beat note signal has been measured with a Fourier-transform (FT) spectrum analyzer and resulting in a 20 dBm signal-to-noise ratio on a 1 kHz bandwidth for both the two CW emissions.

Electronic setup

The beat note is then processed by an electronic chain, generating a correction signal driving the laser diode current. Two identical electronic setups, for which a schematic picture is given in figure (5.2), have been implemented for the two laser diodes. In order to optimize the phase locking mechanism, the electric signal produced by the photodiode undergoes series of filtering and amplifying processes that aim to eliminate the residual Fourier components at >50 MHz frequency and furtherly increase the signal-to-noise ratio. All the electronic components have been purchased by Mini-circuits company.

At first the RF signal, deprived of the higher frequency components by a 10 MHz wide band-pass filter centered at 30 MHz, is amplified by two cascading low-noise amplifiers. Beforethe actual locking circuit, a second 50 MHz low-pass filter ensures the higher harmonics eventually produced by the amplification process to be cutted off. A small fraction of the RF signal (about 20 dB, not shown in figure) is withdrawn to be sent to a spectrum analyzer for continuous monitoring of the laser frequency.

The hearth of the electronic setup, namely the phase-locked-loop (PLL), is composed of a digital phase-detector (PD), comparing the frequency and the phase of the beat note with a stable LO and generating a DC signal proportional to the phase difference, and a proportional-integral (PI) loop. Basically, the PD is based on an exclusive or (XOR) gate followed by an integrating circuit. Supposing both the beat note and the LO being square waves at the same frequency, the XOR gate provides a non-zero (and constant)

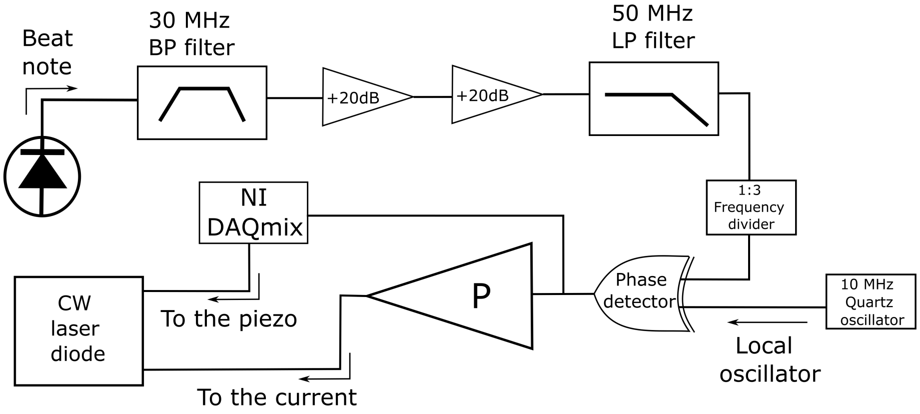

Figure 5.2: Schematic of the electronic setup.

voltage only in those temporal intervals Δt in which the upper half-wave of one signal is overlapped to the lower half-wave of the other one. In other words, a positive output voltage indicates a phase mismatch between the signal and the reference, resulting into a periodic digital signal whose duty-cycle is proportional to the relative phase. As a consequence, the integrator following the logic port transforms the digital signal into a DC voltage being proportional to Δt and, hence, to the phase difference. In the case of our setup, the error signal maps the $\pm 2\pi$ phase range into the 0-5 V voltage. The LO is provided by a low-noise function generator (Keysigth 33500 B) driven by a 10 MHz quartz oscillator. A 1:3 frequency divider, inserted before the XOR port, adjust the $\simeq$30 MHz beat note frequency and allows the iso-frequency condition to be fullfilled.

The signal generated by the PD is then multiplied for a constant factor (adjustable in sign) by a proportional controller and sent to the laser diode current actuator closing the feedback loop. In the phase locking regime, the PD output is, in general, the sum of a constant contribution and a small, rapidly varying term (the error signal), istantaneously adjusted at zero by the feedback signal. Now, the finite constant component may seriously hamper limit the tunability of the locked frequency. Under these circumstances indeed, once the LO frequency or the repetition rate is varied, the PD signal drifts (accordingly to the actual gain) untill it reaches the limit of the allowed voltage range, leading to the laser unlocking. In order to avoid this possibility, a secondary loop has been implemented by acting on the piezo actuator that controls the diode external cavity. In particular, a labview routine compares the PD signal, acquired by a NI DAQ mix, with the voltage corresponding to the zero phase mismatch (i.e. 2.5 V). A generated DC signal, proportional to the measured difference, is sent to the piezo actuator in order to compensate

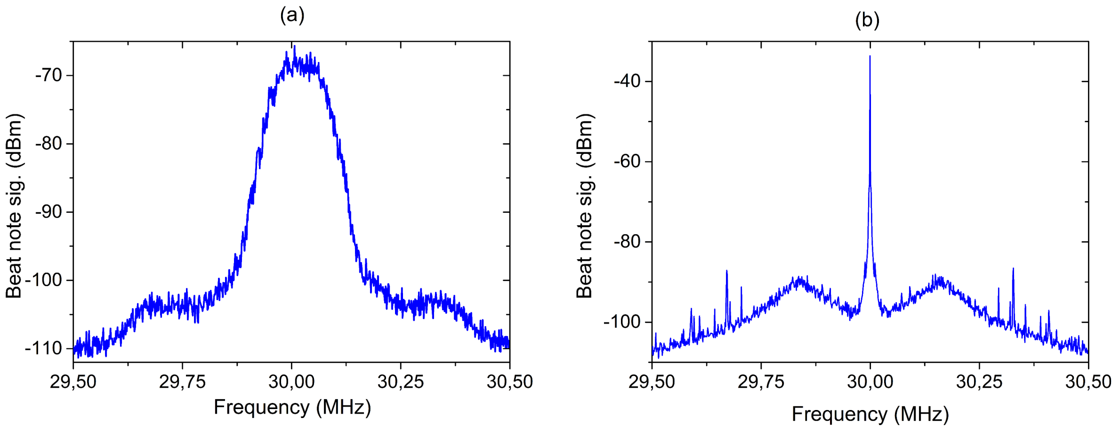

Figure 5.3: Beat note signal between the mode-locked laser and the phase-locked CW laser diodes, respectively (a) D1 at 1550 nm wavelength and (b) D2 at 1605 nm wavelength. Both the spectrum have been acquired with 10 Hz resolution bandwidth.

slow drifts and to recenter the PD output signal.
The achieved results in terms of frequency stability can be seen in figure (5.3) in which, for example, the line profiles of the free-running (a) and the phase-locked (b) laser diode D1, emitting at 1550 nm wavelength are compared. The two traces in figure show the 30 MHz beat note between the ML laser and the D1 emission at 1550 nm wavelength. Both the measurements have been performed for 10 Hz resolution bandwidth and -10 dBm reference level. As can be immediately seen, the PLL makes most of the optical power squeezed at 30 MHz, with dramatic linewidth narrowing and a corresponding increasing (more than 30 dBm) of the central peak. Being the power scale expressed in dBm, the beat note FWHM must be retrieved by considering the full width at -6 dBm. In the third chapter of this thesis the free-running laser linewidth has already been extimated to be in the order of few tens of kHz. The two side bands (usually called servo bumps), at about 200 kHz from the central peak, individuate the PLL bandwidth, namely the inverse of the typical time scale for which the frequency fluctuations can be compensated by the feedback signal.

5.2 Spectroscopic tests

Respect to the spectroscopic measurements discussed in the previous chapter, the frequency locking chain acting on the laser diodes implies a completely different tuning mechanism. In principle, the easiest way to adjust the THz frequency could be to exploit the 1 mHz accuracy ensured by the function generator and change the frequency of one or both the LO signals. Following this approach, the frequency of the IR laser should undergoe the same shift required for the THz frequency, exactly as it happened in the case of the piezo-driven scans. By the way, as we have seen in the previous chapter, when the gas pressure is in the order of tens or hundreds of Pa, the THz tuning range required to acquire the full line profile generally exceeds 100 MHz. Unfortunately, such a frequency range is too wide to be covered in a single scan, because the tunability range of the LO is actually limited to few tens of MHz by the different pre-filtering stages, and in particular the 10 MHz wide band-pass filter. In order to overcome this inconvenient, a different approach has been choosen, consisting in tuning the two IR sources, and therefore the THz frequency, by adjusting directly the repetition rate of the ML laser source. For this purpose, the motorized actuator of the repetition rate has been interfaced with the acquisition program, integrating a dedicated commercial software (provided by the laser manufacturer) within our authomatyzed labview routine. The motorized actuator provides a nominal resolution of $\Delta\nu_{rep} = 10$ Hz/step, corresponding to a $(N_1 - N_2)\Delta\nu_{rep}$ resolution on the generated THz frequency, of the order of hundred of kHz per step and generally depending on the THz frequency to be generated. Note that, despite the DFG process ensures that this strategy will provide the desired accuracy in THz frequency adjustment, the single IR emissions undergoes tens of MHz frequency shift at each step and several GHz in the whole scan. As a consequence, differently from the former tuning methods, in this case the etalon effect, due to the crystal facets reflectivity and potentially distorting the absorption profile, cannot be neglected and the normalization procedure must be applied.

A preliminary calibration, performed by observing with a spectrum analyzer the shift of the 100 MHz beat note produced by the nearest neighbours ML lasr teeth, pointed out that the nominal resolution value is not sufficiently reliable to be adopted for the frequency scale of the scans. For this reason, we decided to use the laser RF ouptut, i.e. an electric signal synchronized to the optical pulses, and for directly measuring the repetition rate with a frequency counter, disciplined by the quartz oscillator driving the LO.

In order to demonstrate the quality enanchement achieved by our spectrometer thanks to the frequency stabilization, a new set of spectroscopic measurements has been performed. Once again, we focused on the $(J = 4, K = 4, n = 2) \rightarrow (5, 5, 2)$ methanol transition at 5.573 THz. Such measurements have been carried out in almost the same experimental conditions of the ones discussed in the previous chapter. To this regards, the main difference lies in the fact that, in order to make the IR background completely negligible, two 1 mm thick black polypropilene filters, one in place of one window of the spectroscopy cell and one placed just before the detector, have been applied. In these conditions the overall

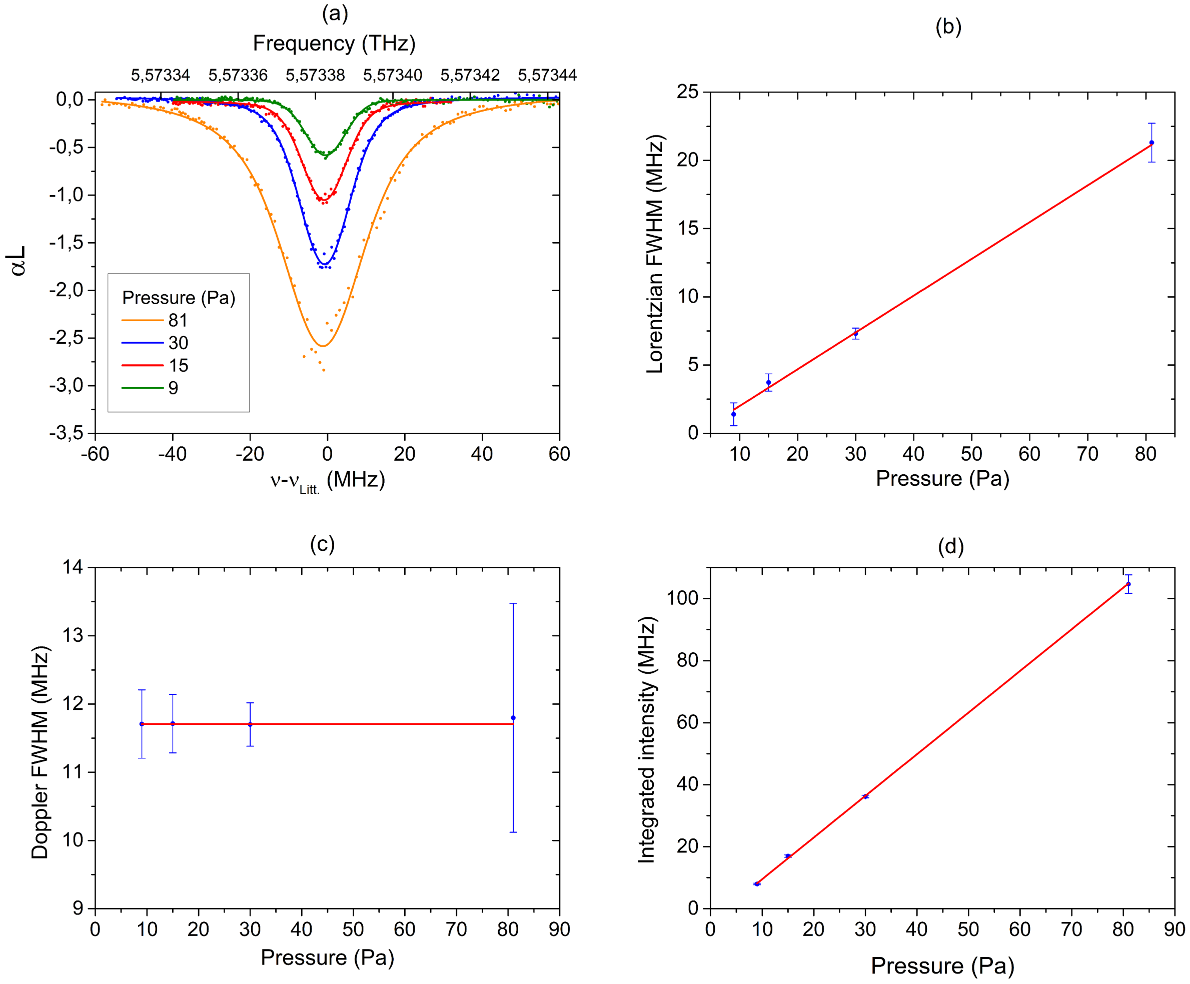

Figure 5.4: a) Absorption profiles as a function of the frequency displacement respect to 5.5733831 THz (from Moruzzi et al.). The experimental data, acquired for different values of the methanol gas pressure, have been fitted with a Voigt function. Full width at half maximum of the lorentzian contribution (b), Doppler linewidth (c) and integrated intensity (d) as a function of the gas pressure. All the measurements refers to a gas temperature of 295 K.

system, composed of the empty spectroscopy cell and the additional filter, attenuates the THz power of about the 63%, so that the 17.5 nW measured power corresponds to about 47 nW of generated power in this spectral region.
A precise determination of the $(N_1 - N_2)$ factor, needed to define our frequency scale, can be achieved by means of a reference value for the expected THz frequency, chosen among the ones available in litterature (in the following we will indicate this number as ν_{Lit}). For the considered methanol transition, beside the 5.573531104 THz (±439 kHz) provided by the JPL database, only another frequency measurement has been so far reported, being measured by G. Moruzzi et al. (5.5733831 THz (±10 MHz) [128]) by means of a Fourier spectrometer. Remarkably, the two values are not compatible each other, with a discrepancy of about 150 MHz, largely exceeding the experimental uncertainties. For this reason, we tried the calibration procedure basing on both these reference values.
For this purpose, the first thing to do is the determination of the integer number of teeth separating the pumping and the signal frequencies.The beat notes have been preliminary analyzed in order to retrieve thier center frequency. Subsequently, the obtained values have been used to determine the teeth spacing, accordingly to the relation

$$N_1 - N_2 = \frac{\nu_{Lit} - \nu_{b1} + \nu_{b2}}{\nu_{rep}}, \tag{5.3}$$

where the sign of the beat notes must be carefully considered. Regarding the calibration based on the measurement by Moruzzi et al., once the N1-N2 integer is obtained a THz frequency scale has been assigned to the spectroscopic measurement according to Eq. 5.2. In figure 5.4 four acquisitions have been reported, for different gas pressures. as a function of the frequency displacement with respect to the frequency reported in [128]. As it can be seen, the line centers retrieved by our fit are in a notable agreement with the previous measurements, with a difference of the order of few hundred of kHz in all the considered measurements. A similar discrepancy is considerably smaller than the typical uncertainties affecting the measurements based on the FT spectrometer, and is consistent with the absolute frequency uncertainty expected from the unreferenced quartz oscillator of the frequency counter.
On the contrary, using as calibration reference the value of ν_{Lit} provided by the JPL catalog, we obtain a different frequency scale, where the retrieved line center fall 10MHz apart from the reference value. This result is not compatible with the precision of our measurement, and suggests a significant error in the reference value. The former calibration has been repeated several times, in different days, intentionally varying both the repetition rate (so that different values of $N_1 - N_2$ are obtained) and the beat note signs. Regarding to the measurement shown here, the beating signal frequencies are $\nu_{b1} = -30.6$

MHz, $\nu_{b2} = -29.4$ MHz and the two IR frequencies result to be spaced of 55733 teeth.
In all the traces reported here the signal has been acquired with a 3 sec/point sampling rate, corresponding to 1 s integration time. At each step the secondary, software-controlled frequency locking, is disabled just before to change the ML laser repetition rate, and immediately restored. This delicate procedure has been necessary in order to perturbate as little as possible the CW lasers frequency during the scan. Indeed, the repetition rate tuning necessarly implies a transient time, of the order of few milliseconds, in which the two CW frequency are unlocked. During this period the error signal undergoes uncontrollable fluctuations that, in some cases, can be amplified by the secondary locking mechanism. The temporary disabling is required to avoid that, as it may happen, the PLL restores the locking of one or both the two frequencies to a different tooth, resulting in a 100 MHz shift in the THz frequency.

All the absorption lines shown in figure (5.4 a) have been fitted with a Voigt profile (4.4). Unlike the test performed with the free-running source, the higher signal-to-noise ratio due to the frequency stability allowed us to investigate a significantly lower pressure range and a progressive reduction of the absorption peak is visible as the linewidth approaches the Doppler limit. As a further consequence, the width of the Gaussian contribution to the linewidth is evident in all the acquired profiles and can be retrieved directly from the fit. As it can be seen from the experimental data in figure (5.4 c), the four measurements are largely compatible within the experimental error and the Doppler width can be cosidered constant at the value (11.70 ± 0.02) MHz, different of about the 3% respect to the expected value.

The plot in figure (5.4 b) shows the linear scaling of the Lorentzian contribution with pressure. In this case, the intercept value is compatible with zero within the experimental uncertainty, as expected since the experimental data do not include the Doppler term. Regarding to the linestrength, it has been retrieved accordingly to the procedure described in the previous chapter, i.e. by fitting the areas subtended by the absorption profile (see figure (5.4 d)) and multiplying the linear coefficient by a factor $k_B T/L$. As a result, we obtained a linestrength of (3.39 ± 0.08) MHz nm^2, differing of about the 11.8% with respect to the value 2.99 MHz nm^2 reported in the JPL database.

In order to achieve a closer comparison with the measurements performed in the free-running regime, the measurement at 30 Pa pressure has been reported again in figure (5.5 a), including the Voigt fit and the residuals plot. At first, a remarkable discrepancy in the absorption line depth, visible to the naked eye, is noted. In our opinion, this effect has to be ascribed to the presence, in the previous measurement, of a residual IR background. Indeed, despite in that case one of the spectroscopic cell windows was made of polypropylene just to avoid this, we are not able to exclude a spurious IR radiation of the

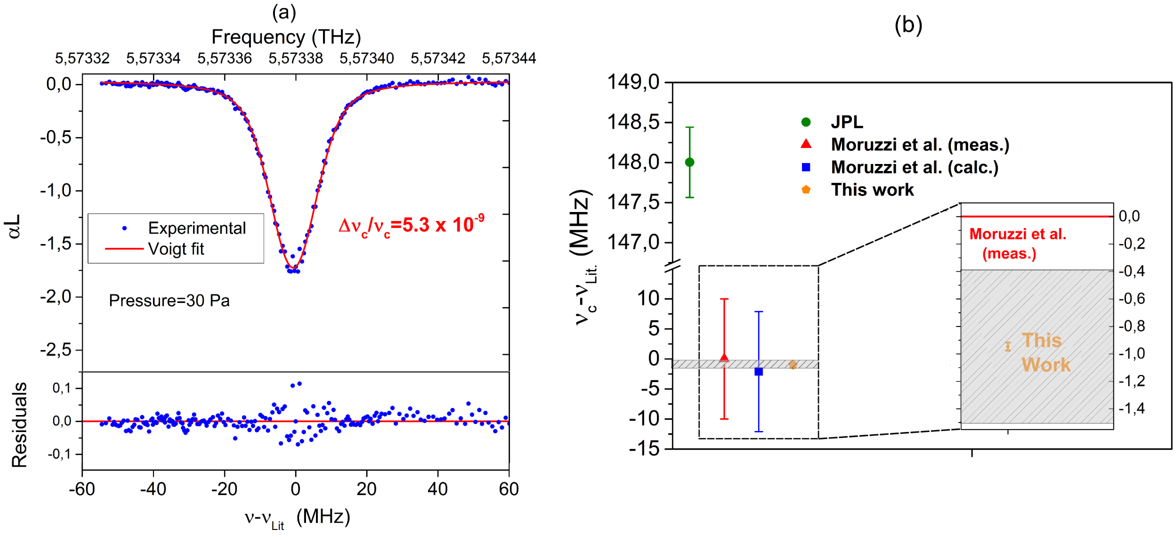

Figure 5.5: a) Absorption profile at 30 Pa pressure as a function of the frequency displacement respect to 5.5733831 THz (from Moruzzi et al.) with Voigt fit and residuals. b) Schematic summary of the state of the art measurements relatively to the considered methanol transition. The experimental error relative to our measurement (in orange) refers exclusively to the uncertainty provided by the fit and does not represent the absolute accuracy. The grey area represents the confidence interval in which we are sure that the true absolute frequency will fall once provided the metrological reference.

order of 1-10 nW collected by the detector. This occurrence can be safely be excluded in the present measurements because of the second filter placed before the sensor.
The present measurement points out a really notable result. Indeed, it gives in this case a frequency uncertainty of 29.8 kHz, more than one order of magnitude smaller with respect to the one provided by the JPL database and three order of magnitudes smaller than the FT spectrometer based measurements. Such a value corresponds to a $\Delta\nu_c/\nu_c = 5.3 \cdot 10^{-9}$ relative precision on the line center determination, demonstrating an improvement of about one order of magnitude with respect to the measurements performed with the free-running source. In the present case, the measurement precision is mainly limited by the signal-to-noise ratio and the Doppler-limited spectroscopic resolution. Is therefore important to stress out that a further improvement in the precision, for example to a level of 10^{-10} - 10^{-11}, will be possible only enabling sub-Doppler spectroscopy by means of more sophysticated techniques. In the previous chapter a preliminary analysis has been carried out to this regards, in an attempt to outline the technical efforts required to reach THz power levels is sufficient for this future purpose.
Finally, the effects on the measurement results of the missing metrological reference to a primary standard deserve here a specific comment. The lab in Arcetri is not yet served by the metrological link, at present provided by INRIM only to the Sesto Fiorentino research area. as a consequence, the frequency counter measuring the ML laser repetition rate, and thus determining the frequency value of the THz radiation, is not asolutely referenced, and relies on its unstabilized quartz oscillator. In order to measure the performances of this unstabilized quartz oscillator, we moved the counter to another lab in Sesto Fiorentino, served by the 10 MHz absolute reference. We have then measured a 100 MHz frequency generated by an absolutely-referenced synthesizer, obtaining a 10 Hz day-by-day maximum instability for our counter. In our case, this slow effect can be considered as a drifting systematic error, eventualy affecting the final accuracy, rather than the spectroscopic precision. Indeed we are more than confident that, once provided the absolute frequency reference, this error source will become negligible. That is why, in the following discussion, we will treat this last error differently from the statistical error affecting the measurement precision.

A final overview of the measured and calculated values for the considered transition frequency is reported in figure (5.5 b). The blue dot refers to the theoretical prediction of the line frequency made by Moruzzi et al. in the same work of the experimental measurement [128]. For the sake of clarity, together with the final result of our frequency measurement and its statistical error (orange dot and error bar), an intentionally overestimated confidence interval in which we are sure that the ”true” absolute frequency will fall once provided the metrological reference, is highlighted in grey. Anyway, as already explained, the 29.8 kHz here can be safely considered as the order of magnitude of the frequency accuracy that our setup will be able to provide once it will be referred to the primary standard. In any case the framework emerging from the graph of figure (5.5 b), and in particular the discrepancy between the two numbers present in literature, is an indication of how the high frequency part of the THz spectrum still requires more extensive studies. We add the fact that other experimental works, carried out by means of TuFIR spectrometers, do not report the considered transition at all, although observing largely weaker transitions in the considered range [129]-[130]. We can conclude that, at the state of the art, further updates to the parameters available in the different databases are far to be excluded. At the same time, we are equally confident that relevant contribution will be provided in the next future thanks to the approach followed in this work.

In conclusion, the room-temperature CW THz spectrometer here presented deserves, in our opinion, a really important role within the present scenario (as summarized in the table below). Its major strength lies in the combination, in a single source, of an ultra-broad spectral coverage, spanning from 0.97 to 7.3 THz (about 3 octaves), and the ability of measuring molecular transition frequencies with arelative precision of few parts in 10^{-9}. Compared to the metrological performance of other state-of-the-art spectrometers, our precision is one order of magnitude better than that achieved with photo-mixing-based synthesizers [119], and comparable to that of the best QCL-based systems [120], needing however liquid-He cryogenic temperatures to operate. The demonstrated capability for spectral measurement in the THz range exceeding 4.7 THz, completely precluded to the most diffused CW THz sources, almost reaches the preformances of the TuFIR technology. Anyway, the source we implemented differs substantially from this latter one for two different reasons. On one hand, the fact to be entirely based on compact and reliable telecom fiber laser technology, making our setup potentially scalable to a relatively compact design. On the other side, the emitted power, surely its major drawback (but further improvements can reasonably be made), is however sufficiently high to allow room-temperature detection of the produced radiation where a cryogenic-cooled bolometer was usually employed.

	OUTPUT POWER LEVEL	GENERATION BW AND MODE-HOP-FREE TUNUNG (MHFT)	FREQUENCY ACCURACY IN SPECTROSCOPY ($\Delta\nu_c/\nu_c$)
QCLs [120]	1 mW	2.5 THz (MHFT= 300 MHz)	$4{\cdot}10^{-9}$
Frequency Multipliers [26]	1 μW	0.9-1.2 THz (MHFT= 200 GHz)	$<1{\cdot}10^{-9}$
Photomixer Synthesyzers [121]	3 μW	0.2-1.5 THz (MHFT= 120 GHz)	$8{\cdot}10^{-8}$
Waveguided Cherenkov DFG	200 nW	0.97-7.3 THz (MHFT= 40 GHz)	$5.3{\cdot}10^{-9}$

5.3 Towards metrological-grade THz spectroscopy

The experimental results discussed in the previous paragreaph actually conclude the work carried out in this PhD thesis. In particular, the spectroscopic measurements presented above underline, once more, that the high frequency part of the THz spectum is relatively little-known. As we have seen in the case of the $(4,4,2) \rightarrow (5,5,2)$ methanol transition, this fact can make the experimental data hard to be interpreted. On the other hand, it shoul be equally clear that, if combined with an absolute frequency reference, the very high precision of our source would lead any possible ambiguity to be removed.
Unfortunately, the referencing of the THz spectrometer to the primary frequency standard did not get far with this work and will be matter for further developments in the next future. Anyway, we consider appropriate to spend the few remaining lines to describe the experimental strategy we plan to follow, as well as the available technologies being useful for our purposes.
Currently, time and frequency standard are provided by a Global Positioning System (GPS) dissemination, practically transferring to a local (disciplined) oscillator the accuracy of an external reference signal. This result is commonly achieved by means of the common-view technique, in which the time difference between two clocks located in different places is measured by comparing them with a common signal provided by a GPS satellite [132]. At the moment, these systems, providing frequency reference with a frac-

tional uncertainty of $5 \cdot 10^{-14}$ on a day average [140], can be considered to be more than enough for THz experiments, which accuracy is limited to the 10^{-9} order. Anyway, it must also be said that this remarkable accuracy is several order of magnitude worse than the primary reference ones, particularly regarding to the case of optical atomic clocks, for which fractional accuracy up to 10^{-18} has been demonstrated [133].

For this reason, in the last few years new distibution networks, mainly microwave satellite link and long-haul optical fiber links (OFLs), have been considered. In particular OFL infrastructures have been demonstrated to be capable for overcoming the intrinsic limitations implied by the common-view GPS technique, providing effective comparison of atotomic clocks [134]-[137] and improving the achieved accuracy in molecular spectroscopy [138]-[139].

As already mentioned in the third chapter, the choice to build a DFG setup being based on IR fields lying in the telecom bandwidth has been mainly driven by the perspective to refer the THz spectrometer to the ultra-stable reference signal at 1542 nm provided by the Italian Institute for Mertological Research (INRIM), and presently available at European Laboratory for Nonlinear Spectroscopy in Sesto Fiorentino (Florence). Such a frequency reference is generated by stabilizng the 1542 nm radiation, provided by a commercial fiber laser, to an ultra-low-expansion glass (ULE) Fabry-Perot cavity, having $5 \cdot 10^{-15}$ relative frequency instability at 1 s and a residual drift of $5 \cdot 10^{-15}$/s [139]-[141]. The long term stability is achieved by phase-locking, thanks to a fiber frequency comb, the laser to a hydrogen-maser referenced to a Cs fountain primary frequency standard. The reference signal, whose frequency is known with a $2 \cdot 10^{-16}$ relative accuracy, is delivered from INRIM to LENS through a 642 Km fiber link, with 171 dB losses compensated by nine bidirectional erbium doped fiber amplifiers [142]. A Doppler noise cancellation scheme, used in order to compensate the frequency shift in the delivered signal arising from vibrational and thermal perturbation occurring along the fiber path, ensures undesired frequency offset to be $< 10^{-16}$. For this purpose, at INRIM part of the fiber laser signal is taken to be exploited as a reference for phase noise detection. Similarly, at LENS part of the recvieved signal, frequency shifted with a 40 MHz acusto-optic modulator, is sent back to Turin to be compared with the local radiarion, in order to reveal the accumulated phase noise and correct it by means of a PLL.

At LENS the incoming 40 nW link signal is regenerated and distributed in a point-to-star configuration to the different end user labs. The regeneration is achieved by amplifying the narrow-line emission provided by a laser diode driven by a low-noise current driver and phase-locked to the reference signal. Finally, after a further filtering process required in order to eliminate the amplified spontaneous emission (ASE) noise due to the nine amplification stages placed along the fiber propagation, the available reference signal is

characterized by a 50 dB signal-to-noise ratio on a 10 MHz bandwidth and a power level > 5 mW.
A further characteristic of the reference radiation, of crucial importance for our purposes, is the presence of two additional sidebands at 10 MHz respect to the carrier frequency. According to our plans, once the fiber link will deliver the frequency reference from LENS to the THz laboratory located at CNR-INO in Arcetri, the absolute frequency accuracy will be tranfered to the generated CW THz radiation by locking the repetition rate of the pulsed source we used for frequency stabilization to these RF sidebands. Moreover, despite this operation could be in principle sufficient in a DFG setup, the relative phase noise between the two involved frequencies generally contributes in a non negligible way, as it scales as the teeth separation. This difficulty can be effectively overcomed by locking the single laser tooth to the 1542 nm primary radiation.

Conclusions

In this thesis, a room-temperature continuous-wave (CW) terahertz (THz) source, based on robust and potentially scalable telecom technology, has been implemented and its application to high-precision molecular spectroscopy has been demonstrated. The generation mechanism, based on difference frequency generation (DFG) in a MgO-doped lithium niobate waveguide, has allowed us to synthesize both THz pulses and single frequency radiation, continuously tunable within the 0.97-7.3 THz spectral range. Furthermore, the surface emission scheme, achieved by taking advantages of the non-collinear Cherenkov phase-matching, has enabled us to minimize the absorption losses and reach power levels being sufficient for both room-temperature detection and high-precision spectroscopy.
The acheved tunability range, of almost three octaves, is by far the widest reported to date and enables us to investigate the spectral region extended beyond 4.5 THz, currently precluded to the most diffused CW THz emitters, as frequency-multipliers, photo-mixers and QCLs. On the physical point of view, the key aspect lying on the basis of this remarkable result is the dramatic increasing pf the phase-matching bandwidth arising from the strong light confinement, achieved by employing a nonlinear channel waveguide. Despite such an approach has already been proposed and applied to the generation of THz pulses generation [114], here the experimental accomlpishment of a single frequency THz source by means of an unprecedented IR power confinement of $\simeq 10^7$ W/cm^2 has been shown for the first time. We sincerely hope the present work to motivate a more diffused employment of the Cherenkov-DFG approach for generation broadly tunable CW THz radiation. In our opinion, this can contribute to fill the lack of information available nowadays in the different THz databases, regarding both molecular physics and materials optics.
Beside such a broad spectral coverage, the realized source has been also demonstrated to be capable for state of the art level spectroscopic measurements on gasseous molecular samples. In particular, mode-hop-free high-resolution tunablity has been demonstrated in a 40 GHz frequency range. This has enabled us to unambigously recognize a complex

absorption pattern, being composed of several tens of lines of a low pressure methanol gas, and suggesting the effectiveness of our spectrometer for gas sensing application in the whole THz molecular fingerprint region.

Moreover, the high spectral purity and frequency stabilitiy, obtained by referring the pump and signal IR fields to a stable local oscillator and transferred to the THz linewidth by the DFG process, allowed us to measure the line center of the $(J, K, n) = (4, 4, 2) \rightarrow (5, 5, 2)$ Doppler-limited methanol transition with a relative precision of few parts in 10^{-9}, namely one order of magnitude better than the one achieved with THz photo-mixers [119], and comparable to that of the THz QCLs [120]. At this stage, further improvements in our precision are hamperd by the Doppler-limited resolution of our measurements. For this reason, in the next future, additional experimental efforts will be devoted to the increasing of the produced THz power in order to implement more sophisticated sub-Doppler techniques.

Finally, the single frequency IR sources will be referred, through a stabilized femtosecond pulsed telecom laser, to the primary frequency standard to get the ultimate metrological performance from this setup.

List of publications

- L. Consolino, S. Jung, A. Campa, M. De Regis, S. Pal, J. H. Kim, K. Fujita, A. Ito, M. Hitaka, S. Bartalini, P. De Natale, M. A. Belkin and M. S. Vitiello
  ‘’Spectral purity and tunability of terahertz quantum cascade laser sources based on intracavity difference-frequency generation”
  Sci. Adv. 3, e1603317 (2017)
- M. De Regis, L. Consolino, S. Bartalini, M. Ravaro and P. De Natale
  ‘’Room-Temperature Source of Continuous-Wave Radiation up to 7.5 THz based on Telecom Technology for High Precision Spectroscopy”
  Submitted for publication to Science Advances

References

[1] C. Sirtori, *"Bridge for the terahertz gap"*. Nature 417, 132 (2002)

[2] B.B. Hu, and M.C. Nuss, *"Imaging with terahertz waves"*. Opt. Lett. 20, 1716 (1995)

[3] T. Kleine-Ostmann, P. Knobloch, M. Koch, S. Hoffmann, M. Breede, M. Hofmann, G. Hein, K. Pierz, M. Sperling and K. Donhuijsen, *"Continuous-wave terahertz imaging"*. Electron. Lett. 37, 1461 (2001)

[4] D. Mittleman, M. Gupta, R. Neelamani, R.G. Baraniuk, J.V. Rudd and M. Koch, *"Recent advances in terahertz imaging"*. Appl. Phys. B 68, 1085 (1999)

[5] V.P. Wallace, A.J. Fitzgerald, S. Shankar, N. Flanagan, R. Pye, J. Cluff and D.D. Arnone *"Terahertz pulsed imaging of basal cell carcinoma ex vivo and in vivo"*. Br. J. Dermatol. 151, 424 (2004)

[6] E. Pickwell and V.P. Wallace *"Biomedical applications of terahertz technology"*. J. Phys. 39, R301 (2006)

[7] D. Mittleman, R.H. Jacobsen and M.C. Nuss *"T-ray imaging"*. IEEE J. Sel. Top. Quantum Electron. 2, 679 (1996)

[8] C. Joerdens, M. Sheller, B. Breitenstein, D. Selmar and M. Koch *"Evaluation of leaf water status by means of permittivity at terahertz frequencies."*. J. Biol. Phys 35, 255 (2009)

[9] D. Zimdars, J.S. White, G. Stuk, A. Chernovsky, G. Fichter and S. Williamson *"Large area terahertz imaging and non-destructive evaluation applications"*. Insight 48, 573 (2006)

[10] C. Joerdens and M. Koch *"Detection of foreign bodies in chocolate with pulsed terahertz spectroscopy"*. Opt. Eng. 47, 037003 (2008)

[11] M. Herrmann, M. Tani, M. Watanabe and K. Sakai *"Terahertz imaging of objects in powders"*. IEEE Proc. Optoelectron. 149, 116 (2002)

[12] N. Krumbholz, T. Hochrein, N. Vieweg, T. Hasek, K. Kretschmer, M. Bastian, M. Mikulics and M. Koch, *"Monitoring polymeric compounding processes inline with THz time-domain spectroscopy"*. Polym. Testing 28, 30 (2009)

[13] D. Banerjee, W. von Spiegel, M. D. Thomson, S. Schabel, and H. G. Roskos *"Diagnosing water content in paper by terahertz radiation"*. Opt. Express 16, 9060 (2008)

[14] A. I. Hernandez-Serrano, S. C. Corzo-Garcia, E. Garcia-Sanchez, M. Alfaro, and E. Castro-Camus, *"Quality control of leather by terahertz time-domain spectroscopy"*. Appl. Opt. 53, 7872 (2014)

[15] F. C. De Lucia, P. Helminger, and W. Gordy, *"Submillimeter-Wave Spectra and Equilibrium Structures of the Hydrogen Halides"*. Phys. Rev. A 3, 1849 (1971)

[16] G. Di Lonardo, L. Fusina, P. De Natale, M. Inguscio and M. Prevedelli, *"The Pure Rotation Spectrum of HBr in the Submillimeter-Wave Region"*. J. Mol. Spectrosc. 148, 86 (1991)

[17] G. Cazzoli and C. Puzzarini, *'The Lamb-dip spectrum of the* $J = 1 \leftarrow 0$ *transition of DF: Crossing resonances and hyperfine components"*.J. Mol. Spectrosc. 231, 124 (2005)

[18] F. C. De Lucia, P. Helminger, R. L. Cook and W. Gordy, *"Millimeter and Submillimeter Wave Rotational Spectrum and Centrifugal Distortion Effects of HDO"*. J. Chem. Phys. 55, 5334 (1971)

[19] F. C. De Lucia, P. Helminger, R. L. Cook and W. Gordy, *"Submillimeter Microwave Spectrum of* $H_2\,^{16}O$*"*. Phys. Rev. A 5, 487 (1972)

[20] P. Helminger, R. L. Cook and F. C. De Lucia *"Microwave spectrum and centrifugal distortion effects of HDS"*. J. Chem. Phys. 40, 125 (1971)

[21] P. Helminger, R. L. Cook and F. C. De Lucia, *"Microwave Spectrum and Centrifugal Distortion Effects of H2S "*. J. Chem. Phys. 56, 4581 (1972)

[22] D. Leisawitz, W. Danchi, M. DjPjirro, et al. *"Scientific motivations and technology requirements for the SPIRIT and SPECS far-infrared/submillimeter space interferometers"*. Proc. SPIE 4013, 36 (2000)

[23] P. Thaddeus, *"The prebiotic molecules observed in the interstellar gas"*. Philos. Trans. R. Soc. B 361, 1681 (2006)

[24] M. Bellini, P. De Natale, G. Di Lonardo, L. Fusina, M. Inguscio and M. Prevedelli, *"Tunable far infrared spectroscopy of* $^{16}O_3$ *ozone"*. J. Mol. Spectros. 152 256 (1992)

[25] N. C. Luhmann and W. A. Peebles, *"Instrumentation for magnetically confined fusion plasma diagnostics"*. Rev. Sci. Instrum. 55, 279 (1984)

[26] G. Cazzoli and C. Puzzarini, *"Sub-Doppler Resolution in the THz Frequency Domain: 1 kHz Accuracy at 1 THz by Exploiting the Lamb-Dip Technique"*. J. Phys. Chem. A 117, 13759 (2013)

[27] T. L. Nicholson, S. L. Campbell, R. B. Hutson, G. E. Marti, B. J. Bloom, R. L. McNally, W. Zhang, M. D. Barrett, M. S. Safronova, G. F. Strouse, W. L. Tew, and J. Ye, *"Systematic evaluation of an atomic clock at 21018 total uncertainty"*. Nature Comm. 6, 6896 (2015)

[28] E.R. Hudson, H.J. Lewandowski, B.C. Sawyer and J. Ye, *"Cold molecule spectroscopy for constrain the evolution of the fine structure constant"*, Phys. Rev. Lett. 96, 143004 (2006)

[29] J. Darling, *"Methods for Constraining Fine Structure Constant Evolution with OH Microwave Transitions"*. Phys. Rev. Lett. 91, 100301 (2003)

[30] J. J. Hudson, D. M. Kara, I. J. Smallman, B. E. Sauer, M. R. Tarbutt, and E. A. Hinds, Nature 473 (2011), 493.

[31] J. Baron, W. C. Campbell, D. DeMille, J. M. Doyle, G. Gabrielse, Y. V. Gurevich, P. W. Hess, N. R. Hutzler, E. Kirilov, I. Kozyryev, B. R. O'Leary, C. D. Panda, M. F. Parsons, E. S. Petrik, B. Spaun, A. C. Vutha, and A. D. West, Science 343 (2013), 6168.

[32] C. Daussy, T. Marrel, A. Amy-Klein, C. T. Nguyen, C. J. Borde, and C. Chardonnet, Phys. Rev. Lett. 83 (1999), 1554.

[33] M. Ziskind, C. Daussy, T. Marrel, and C. Chardonnet, Eur. Phys. J. D 20 (2002), 219.

[34] E. J. Salumbides, G. D. Dickenson, T. I. Ivanov, and W. Ubachs, Phys. Rev. Lett. 107 (2011), 043005.

[35] L. Moretti, A. Castrillo, E. Fasci, M. D. D. Vizia, G. Casa, G. Galzerano, A. Merlone, P. Laporta, and L. Gianfrani, *"Determination of the boltzmann constant by means of precision measurements of H18 2 O line shapes at 1.39μm"*. Phys. Rev. Lett. 111, 060803 (2013)

[36] L. Consolino, S. Bartalini and P. De Natale, *"Terahertz frequency metrology for spectroscopic applications, a review"*. J. of Infrared Milli. and terahz waves 38, 1289 (2017)

[37] G. Kolzov and A. Volok, *"Millimeter and submillimeter wave spectroscopy of solids"*. Springer-Verlag, Berlin (1998)

[38] B. Gorshunov, A. Volkov, I. Spektor, A. Prokhorov, A. Mukhin, M. Dressel, S. Uchida and A. Loidl, *"Terahertz BWO-Spectrosopy"*, International Journal of Infrared and Millimeter Waves 26, 1217 (2005)

[39] G. Klapper, F. Lewen, R. Gendriesch, S. P. Belov and G. Winnewisser, *"Sub-Doppler Measurements of the rotational spectrum of* $^{13}C^{16}O$*"*. J. Mol. Spectrosc. 201, 124 (2000)

[40] F. Ciocci, R. Bartolini, A. Doria, G.P. Gallerano, E. Giovenale, M.F. Kimmitt, G. Messina and A. Renieri *"First operation of a compact FEL in the millimeter wave region"*, Nuclear Instruments and Methods in Physics Research A 331 (1993)

[41] T.Y. Chang and T.J. Bridges *"Laser action at 452, 496, and 541 μm in optically pumped CH3F"*. Opt. Comm. 1, 423 (1970)

[42] G.W. Chantry, *"Long-wave Optics: Applications"*. Long-wave Optics: The Science and Technology of Infrared and Near-millimetre Waves, Accademic Press (1984)

[43] M. Jackson, H. Alves, R. Holman, R. Minton L. R. and Zink, *New cw Optically Pumped Far-Infrared Laser Emissions Generated with a Transverse or 'Zig-Zag' Pumping Geometry"*. J. of Infrared, Milli. and Terahz Waves 35, 282 (2014)

[44] R.F. Kazarinov and R.A. Suris, *"Possible amplification of electromagnetic waves in a semiconductor with a superlattice"*. Sov. Phys. Semicond. 5, 707 (1971)

[45] J. Faist, F. Capasso, D. L. Sivco, C. Sirtori A.L. Hutchinson and A. Y. Cho *"Quantum cascade laser"*. Science 264, 553 (1994)

[46] R. Koehler, A. Tredicucci, F. Beltram, H. E. Beere, E. H. Linfield, A. G. Davies, D. A. Ritchie, R. C. Iotti and Fausto Rossi, *"Terahertz semiconductor heterostructure laser"*. Nature 417, 156 (2002)

[47] M. Fischer and G. Scalari and Ch. Walther and J. Faist, *"Terahertz quantum cascade lasers based on* $In_{0.53}Ga_{0.47}As/In_{0.52}Al_{0.48}As/InP$. J. Cryst. Growth 311, 1939 (2009)

[48] C. Deutsch, M. Krall, M. Brandstetter, H. Detz, A. M. Andrews, P. Klang, W. Schrenk, G. Strasser and K. Unterrainer, *High performance InGaAs/GaAsSb terahertz quantum cascade lasers operating up to 142K*, Appl. Phys. Lett. 101, 211117 (2012)

[49] K. Ohtani and M. Beck and G. Scalari and J. Faist, *"Terahertz quantum cascade lasers based on quaternary AlInGaAs barriers"*, Appl. Phys. Lett. 103, 041103 (2013)

[50] H. Luo and S. R. Laframboise and Z. R. Wasilewski and G. C. Aers and H. C. Liu and J. C. Cao, *"Terahertz quantum-cascade lasers based on a three-well active module"*. Appl. Phys. Lett. 90, 041112 (2007)

[51] S. Fathololoumi and E. Dupont and C.W.I. Chan and Z.R. Wasilewski and S.R. Laframboise and D. Ban and A. Matyas and C. Jirauschek and Q. Hu and H. C. Liu, *"Terahertz quantum cascade lasers operating up to ~ 200 K with optimized oscillator strength and improved injection tunneling"*. Opt. Express 20, 3866 (2012)

[52] J. Alton,S. Barbieri, C. Worral, M. Houghton, H. E. Beere, E. L. Linfield and D. A. Ritchie, *"Optimum resonant tunnelling injection and influence of doping density on the performance of THz bound-to-continuum cascade lasers"*. Proc. SPIE 5727 (2005)

[53] L. Schrottke, M. Weinold, R. Sharma, X. Lu, K. Biermann, R. Hey, A. Tahraoui, H. Richter, H.W. Huebers and H.T. Grahn, *"Quantum-cascade lasers as local oscillator for heterodyne spectrometers in the spectral range around 4.745 THz"*. Semicond. Sci. Technol. 28, 035011 (2013)

[54] K. Ohtani, D. Turcinkova, C. Bonzon, I.C.B. Chelmus, M. Beck, J. Faist, M. Justen, U. U Graf, M. Mertens and J. Stutzki, *"High performance 4.7 THz GaAs quantum cascade lasers based on four quantum wells"*. New Jour. Of Phys. 18, 123004 (2016)

[55] Q. Qin, B.S. Williams, S. Kumar, J.L. Reno and Q. Hu, *"Tuning a Terahertz wire laser"*. Nat. Photonics 3, 732 (2009)

[56] Q. Qin, J. L. Reno and Q. Hu, *"MEMS-based tunable terahertz wire-laser over 330GHz"*. Opt. Lett. 36, 692 (2011)

[57] B.J. Rizzi, T. Crowe, N. R Erickson, *"A high-power millimeter-wave frequency doubler using a planar diode array"*. IEEE Microwave and Guided Wave Letters 3, 188 (1993)

[58] J. Tuovinen and N.R. Erickson, *"Analysis of a 170 GHz frequency doubler with an array of planar diodes"*. IEEE Trans. Microwave Theory Tech. 43, 962 (1995)

[59] A. Maestrini, J. S. Ward, H. Javadi, C. Tripon-Canseliet, J. Gill, G. Chattopadhyay, E. Schlecht, and I. Mehdi, *"Local Oscillator Chain for 1.55 to 1.75 THz with 100 μW Peak Power"*. IEEE Microwave and Wireless Components Letters 15, 871 (2005)

[60] J.C. Pearson, B.J. Drouin, A. Maestrini, I. Mehdi, J. Ward, R.H. Lin, et al., *"Demonstration of a room temperature 2.48-2.75 THz coherent spectroscopy source"*. Rev. Sci. Instrum. 82, 093105 (2011)

[61] D.D. Bicanic, B.F.J. Zuidberg and A. Dymanus, *"Generation of continuously tunable laser sidebands in the submillimeter region"*. Appl. Phys. Lett. 32, 367 (1978)

[62] H. R. Fetterman, P. E. Tannenwald, B. J. Clifton, C. D. Parker, W. D. Fitzgerald and N. R. Erickson, *"Far-ir heterodyne radiometric measurements with quasioptical Schottky diode mixers"*. Appl. Phys. Lett. 33, 151 (1978)

[63] K.M. Evenson, D.A. Jennings and F.R. Petersen, *"Tunable far-infrared spectroscopy"*. Appl. Phys. Lett. 44, 576 (1984)

[64] I.G. Nolt, J.V. Radostitz, G. Di Lonardo, K.M. Evenson, D.A. Jennings, K.R. Leopold, M.D. Vanek, L.R. Zink, A. Hinz and K.V. Chance, *"Accurate rotational constants of CO, HCl, and HF: Spectral standards for the 0.3 to 6 THz (10 to 200 cm^1) region"*. J. Mol. Spectrosc. 125, 274 (1987)

[65] H. Odashima, M. Tachikawa, L. R. Zink and K. M. Evenson, *"Extension of tunable far-infrared spectroscopy to 7.9THz"*. Opt. Lett. 11, 822 (1997)

[66] H. Odashima, L. R. Zink and K. M. Evenson, *"unable far-infrared spectroscopy extended to 9.1 THz"*. Opt. Lett. 6, 406 (1999)

[67] S. Verghese, K. A. McIntosh, and E. R. Brown, *"Highly tunable fiber-coupled photomixers with coherent terahertz output power"*. IEEE Trans. Microwave Theory and Tech. 45, 1301 (1997).

[68] S. Matsuura, M. Tani, and K. Sakai, *"Generation of coherent terahertz radiation by photomixing in dipole photoconductive antennas"*. Appl. Phys. Lett. 70, 559 (1997).

[69] M. Kominami, D. M. Pozar, and D. H. Schaubert, *"Dipole and Slot Elements and Arrays on Semi-Infinite Substrates"*. IEEE Trans. Antennas Propag. 33, 600 (1985).

[70] E. R. Brown, F. W. Smith and K. A. McIntosh, *"Coherent millimeter-wave generation by heterodyne conversion in low-temperature-grown GaAs photoconductors"*. J. of Appl. Phys. 73, 1480 (1993)

[71] S. M. Duffy, S. Verghese, K. A. McIntosh, A. Jackson, A. C. Gossard, and S. Matsuura, *"Accurate modeling of dual dipole and slot elements used with photomixers for coherent terahertz output power"*. IEEE Trans. Microwave Theory and Tech. 49, 1032 (2001).

[72] P. A. Franken, A. E. Hill, C. W. Peters and G. Weinreich, *"Generation of Optical Harmonics"*. Phys. Rev. Lett. 7, 118 (1961)

[73] D.A. Kleinman, *"Nonlinear Dielectric Polarization in Optical Media"*. Phys. Rev. 126, 1977 (1962)

[74] W. Shi, Y. J. Ding, N. Fernelius and K. Vodopyanov, *"Efficient, tunable, and coherent 0.18-5.27 THz source based on GaSe crystals"*. Opt. Lett. 16, 1454 (2002)

[75] R. Sowade, I. Breunig, I. Camara Mayorga, J. Kiessling, C. Tulea, V. Dierolf, and K. Buse, *"Continuous-wave optical parametric terahertz source"*. Opt. Express 17, 22303 (2009)

[76] J. Kiessling, F. Fuchs, K. Buse, and I. Breunig, *"Pump-enhanced optical parametric oscillator generating continuous wave tunable terahertz radiation"*. Opt. Lett. 36, 4374 (2011)

[77] J. Kiessling, I. Breunig, P. G. Schunemann, K. Buse and K. L. Vodopyanov, *"High power and spectral purity continuous-wave photonic THz source tunable from 1 to 4.5 THz for nonlinear molecular spectroscopy"*. New Journal of Physics 15, 105014 (2013)

[78] M. A. Belkin,F. Capasso, A. Belyanin,D.L. Sivco, A. Y. Cho, D. C. Oakley, C. J. Vineis and G. W. Turner, *"Terahertz quantum cascade laser source based on intracavity difference frequency generation"*. Nat. Photonics 1, 288 (2007)

[79] M. A. Belkin, F. Capasso, F. Xie, A. Belyanin, M. Fischer, A. Wittmann and J. Faist, *"Room temperature terahertz quantum cascade laser source based on intracavity difference-frequency generation"*. Appl. Phys. Lett. 92, 201101 (2008)

[80] Q. Y. Lu, N. Bandyopadhyay, S. Slivken, Y. Bai and M. Razeghi, *"Room temperature single-mode terahertz sources based on intracavity difference frequency generation in quantum cascade lasers"*. Appl. Phys. Lett. 99, 131106 (2011)

[81] P. Yeh, *"Optical waves in layered media"*. Wiley, New York (1988)

[82] J.A. L'Huiller, G. Torosyan, M. Theuer, Y. Avetisyan and R. Beigang, *"Generation of THz radiation using bulk, periodically and aperiodically poled lithium niobate - Part 1: theory"*. Appl. Phys. B 86, 197 (2007)

[83] K. Suizu, K. Koketsu, T. Shibuya, T. Tsutsui, T. Akiba and K. Kawase, *"Extremely frequency-widened terahertz wave generation using Cherenkov-type radiation"*. Opt. Express. 8, 6676 (2009)

[84] P. U. Jepsen, D. Cooke and M. Koch, *"Terahertz spectroscopy and imaging - Modern techniques and applications"*. Laser and Photonics Reviews 5, 124 (2011)

[85] D. J. Jones, S. A. Diddams, J. K. Ranka, A. Stentz, R. S. Windeler, J. L. Hall and S. T. Cundiff, *"Carrier-Envelope Phase Control of Femtosecond Mode Locked Lasers and Direct Optical Frequency Synthesis"*. Science 288, 635 (2000)

[86] T. Yasui, Y. Kabetani, E. Saneyoshi, S. Yokoyama and T. Araki, *"Terahertz frequency comb by multifrequency-heterodyning photoconductive detection for high-accuracy, high-resolution terahertz spectroscopy"*. Appl. Phys. Lett. 88, 241104 (2006)

[87] T. Yasui, S. Yokoyama, H. Inaba, K. Minoshima, T. Nagatsuma and T. Araki, *"Terahertz frequency metrology based on frequency comb"*. IEEE J. Sel. Top. Quantum Electron. 17, 191 (2011)

[88] L. Consolino, A. Taschin, P. Bartolini, S. Bartalini, P. Cancio, A. Tredicucci, H. E. Beere, D. A. Ritchie, R. Torre, M. S. Vitiello and P. De Natale, *"Phase-locking to a free-space terahertz comb for metrological-grade terahertz lasers"*. Nature Commun. 3, 1040 (2012)

[89] M. Scheller, J.M. Yarborough, J.V. Moloney, M. Fallahi, M. Koch and S. Koch, *"Room temperature CW milliwatt THz source"*. Opt. Exp. 18, 138143 (2010)

[90] N. J. Doran and David Wood, *"Nonlinear-optical loop mirror"*. Opt. Lett. 13, 56 (1988)

[91] K. K. Hamatsu Photonics, *"Guide to streak camera"*. www.hamamatsu.com

[92] A. Hayat, A. Nevet, P. Ginzburg and M. Orenstein, *"Applications of two-photon processes in semiconductor photonic devices: invited review"*. Semicond. Sci. Technol. 26, 083001 (2011)

[93] R. S. Weis and T. K. Gaylord, *"Lithium niobate: Summary of physical properties and crystal structure"*. Appl. Phys. A 37, 191 (1985)

[94] R. C. Alferness, *"Guided-wave devices for optical fiber communications"*. Proc. 1st European Conf. on Integrated Optics, 46 (1981)

[95] C. W. Carr, H. B. Radousky and S. G. Demos, *"Wavelength Dependence of Laser-Induced Damage: Determining the Damage Initiation Mechanisms"*. Phys. Rev. Lett. 91, 127402 (2003)

[96] E. I. Moses, R. N. Boyd, B. A. Remington, C. J. Keane and R. Al-Ayat, *"The National Ignition Facility: Ushering in a new age for high energy density science"*. Physics of Plasmas 16, 041006 (2009)

[97] O. F. Schirmer, M. Imlau, C. Merschjann and B. Schoke, *"Electron small polarons and bipolarons in LiNbO$_3$"*. Journal of Physics: Condensed Matter 21, 123201 (2009)

[98] I. Breunig, M. Falk, B. Knabe, R. Sowade, K. Buse, P. Rabiei, and D. H. Jundt, *"Second harmonic generation of 2.6 W green light with thermo-electrically oxidized undoped congruent lithium niobate crystals below 100 ^{o}C"*. Appl. Phys. Lett. 91, 221110 (2007)

[99] G. D. Miller, R. G. Batchko, W. M. Tulloch, D. R. Weise, M. M. Fejer, and R. L. Byer, *"42 % efficient single-pass cw second-harmonic generation in periodically poled lithium niobate"*. Opt. Lett. 22, 1834 (1997)

[100] D. A. Bryan, R. Gerson, and H. E. Tomaschke, *"Increased optical damage resistence in lithium niobate"*. Appl. Phys. Lett. 44, 847 (1984)

[101] N.Iyi, Y.Kitamure, and S.Kimuar, *"Defect structure modelof MgO-doped LiNbO$_3$"*. J. Solid State Chem. 118, 148 (1995)

[102] G. E. Peterson, A. M. Glass, A. Carnevale, and P. M. Bridenbaugh, *"Control of laser damage in LiNbO$_3$"*. J. Am. Ceram. Soc. 56, 278 (1973)

[103] M. Koesters, B. Sturman, P. Werheit, D. Haertle, and K. Buse, *"Optical cleaning of congruent lithium niobate crystals"*. Nature Photonics 3, 510 (2009)

[104] D. E. Zelmon, D. L. Small and D. Jundt, *"Infrared corrected Sellmeier coefficients for congruently grown lithium niobate and 5 mol.% magnesium oxide-doped lithium niobate"*. J. Opt. Soc. Am. B 12, 3319 (1997)

[105] O. Gayer, Z. Sacks, E. Galun and A. Arie, *"Temperature and wavelength dependent refractive index equations for MgO-doped congruent and stoichiometric LiNbO$_3$"*. Appl. Phys. B 91, 343 (2008)

[106] B. J. Thompson, E. Hartfield, W.G. Driscoll, and Vaughan *"Handbook of Optics"*. McGraw Hill, New York (1978)

[107] A. N. Kaul and K. Thyagarajan, *"Inverse WKB method for refractive index profile estimation of monomode graded index planar optical waveguides"*. Opt. Comm. 48, 313 (1984)

[108] I.P. Kaminov and L. W. Stulz, *Loss in cleaved Ti-diffused LiNbO$_3$ waveguides"*. Appl. Phys. Lett. 33, 62 (1978)

[109] Y. Okamura, S. Yoshinaka and S. Yamamoto, *Measuring mode propagation losses of integrated optical waveguides: a simple method"*. Appl. Opt. 22, 3892 (1983)

[110] Y. C. Wu *"Planar waveguides of Y2O3, Y2O3:Tb3+ and YAG prepared by sol-gel: analysis, structure and optical"*. PhD dissertation, Claude Bernard University, Lyon (2005)

[111] R. Regener and W. Sohler, *"Loss in low finesse Ti:LiNbO$_3$ optical waveguide resonators"*. Appl. Phys. B 36, 143 (1985)

[112] J. Dai, J. Zhang, W. Zhang, and D. Grischkowsky *"Terahertz time-domain spectroscopy characterization of the far-infrared absorption and index of refraction of high-resistivity, float-zone silicon"*. J. Opt. Soc. Am. B 21, 1379 (2004)

[113] J. Kiessling, K. Buse, and I. Breunig, *"Temperature-dependent Sellmeier equation for the extraordinary refractive index of 5 mol. % MgO-doped LiNbO*$_3$ *in the terahertz range"*. J. Opt. Soc. Am. B 30, 950 (2013)

[114] S. Fan, H. Takeuchi, T. Ouchi, K. Takeya and K. Kawase, *‘’Broadband terahertz wave generation from a MgO:LiNbO*$_3$ *ridge waveguide pumped by a 1.5 μm fmtosecond fiber laser"*. Opt. Lett. 38, 1654 (2013)

[115] M. Nagaia, K. Tanaka, H. Ohtake, T. Bessho, T. Sugiura, T. Hirosumi, and M. Yoshida, *‘’Generation and detection of terahertz radiation by electro-optical process in GaAs using 1.56 μm fiber laser pulses"*. Appl. Phys. Lett 85, 3974 (2004)

[116] J. Villarroel, J. Carnicero, F. Luedtke, M. Carrascosa, A. Garcia-Cabanes1, J. M. Cabrera, A. Alcazar and B. Ramiro, *"Analysis of photo-refractive optical damage in lithium niobate: application to planar waveguides"*. Opt. exp. 20, 20852 (2010)

[117] F.C. De Lucia, *"The submillimeter: A spectroscopist's view"*. Journal of Molecular Spectroscopy 261, 1 (2010)

[118] A.S. Skryl, D.G. Pavelyev, M.Y. Tretyakov and M.I. Bakunov, *"High-resolution terahertz spectroscopy with a single tunable frequency comb"*. Opt. Exp. 22, 32277 (2014)

[119] Y. Hsieh, H. Kimura, K. Hayashi, T. Minamikawa, Y. Mizutani, H. Yamamoto, T. Iwata, H. Inaba, K. Minoshima, F. Hindle and T. Yasui, *"THz frequency domain-spectroscopy of a low-pressure acetonitrile gas by a dual optical frequency combs"*. J. IR Mill. THz Wave 37, 903 (2016)

[120] S. Bartalini, L. Consolino, P. Cancio, P. De Natale, P. Bartolini, A. Taschin, M. De Pas, H. Beere, D. Ritchie, M. Vitiello and R. Torre, *"Frequency-comb-assisted THz quantum cascade laser spectroscopy"*. Phys. Rev. X 4, 021006 (2014)

[121] C. Bray, A. Cuisset, F. Hindle, R. Bocquet, G. Mouret and B.J. Drouin, *"CH3D photomixing spectroscopy up to 2.5 THz: new set of rotational and dipole parameters, first THz self-broadening measurements"*. J. of Quantitative spectroscopy and Radiative Transfer 189, 198 (2017)

[122] L. Consolino, A. Campa, M. Ravaro, D. Mazzotti, M.S. Vitiello, Sbartalini and P. De Natale, *"Saturated absorption in a rotational molecular transition at 2.5 THz using a quantum cascade laser"*. Appl. Phys. Lett. 106, 021108 (2015)

[123] T. Hagelschuer, M. Wienold, H. Richter, L. Schrottke, K. Biermann, H.T. Grahn and H.W. Huebers, *"THz gas spectroscopy through self-mixing in a quantum cascade laser"*. Appl. Phys. Lett. 109, 191101 (2016)

[124] E. V. Loewenstein, D. R. Smith, and R. L. Morgan, *"Optical Constants of Far Infrared Materials. 2: Crystalline Solids"* . Appl. Opt. 12, 938 (1973)

[125] H. J. Bakker, S. Hunsche, and H. Kurz, *"Investigation of anharmonic lattice vibrations with coherent phonon polaritons"*. Phys. Rev. B 50, 914 (1994)

[126] M. Unferdorben, Z. Szaller, I. Hajdara, J. Hebling and L. Palfalvi, *"Measurement of Refractive Index and Absorption Coefficient of Congruent and Stoichiometric Lithium Niobate in the Terahertz Range"* . J Infrared Milli Terahz Waves 36, 1203 (2015)

[127] R. M. Lees and J. G. Baker, *"Torsion-vibration-rotation interactions in methanol. I. Millimeter wave spectrum"*. J. Chem. Phys. 48, 5299 (1968)

[128] G. Moruzzi, P. Riminucci, F. Strumia, B. Carli, M. Carlotti, R. M. Lees, I. Mukhopadhyay, J. W. C. Johns, B. P. Winnewisser and M. Winnewisser , *"The spectrum of CH_3OH between 100 and 200 cm^{-1}; torsional and forbidden transitions"*. J. of Molec. Spectrosc. 144, 139 (1990)

[129] F. Matsushima, K. M. Evenson and L. R. Zink, *"Absolute frequency measurements of methanol from 1.5 to 6.5 THz"*. J. of Molec. Spectrosc. 164, 517 (1994)

[130] H. Odashima, F. Matsushima, K. Nagai, S. Tsunekawa and K. Takagi, *"Far-infrared spectroscopy of methanol using a tunable radiation source"*. J. of Molec. Spectrosc. 173, 404 (1995)

[131] L. Consolino, A. Campa, M. Ravaro, D. Mazzotti, M.S. Vitiello, Sbartalini and P. De Natale, *"Saturated absorption in a rotational molecular transition at 2.5 THz using a quantum cascade laser"*. Appl. Phys. Lett. 106, 021108 (2015)

[132] D. W. Allan and M. A. Weiss, *"Accurate Time and Frequency Transfer During Common-View of a GPS Satellite"*. Proceedings of the 1980 Frequency Control Symposium, 334 (1980)

[133] A. D. Ludlow, M. M. Boyd, J. Ye and P. O. Schmidt, *"Optical atomic clocks"* Rev. Mod. Phys. 87, 637 (2015)

[134] A. Yamaguchi, M. Fujieda, M. Kumagai, H. Hachisu, S. Nagano, Y. Li, T. Ido, T. Takano, M. Takamoto and H. Katori, *"Direct comparison of distant optical lattice clocks at the* 10^{-16} *uncertainty"*. Appl. Phys. Express 4, 082203 (2011)

[135] A. Matveev, C. G. Parthey, K. Predehl, J. Alnis, A. Beyer, R. Holzwarth, T. Udem, T. Wilken, N. Kolachevsky, M. Abgrall, D. Rovera, C. Salomon, P. Laurent, G. Grosche, O. Terra, T. Legero, H. Schnatz, S. Weyers, B. Altschul and T. W. Hansch, *"Precision measurement of the hydrogen 1S2S frequency via a 920 km fiber link"*. Phys. Rev. Lett. 110, 230801 (2013)

[136] S. Droste, C. Grebing, J. Leute, S. M. F. Raupach, A. Matveev, T. W. Hansch, A. Bauch, R. Holzwarth and G. Grosche, *"Characterization of a 450 km baseline GPS carrier-phase link using an optical fiber link"*. New J. Phys. 17, 083044 (2015)

[137] P. Morzy'nski, M. Bober, D. Bartoszek-Bober, J. Nawrocki, P. Krehlik and L.Sliwczy'nski *"Absolute measurement of the $^1S_0$-$^3P_0$ clock transition in neutral ^{88}Sr over the 330 km-long stabilized fiber optic link"* Sci. Rep. 5, 17495 (2015)

[138] B. Argence, B. Chanteau, O. Lopez, D. Nicolodi, M. Abgrall, C. Chardonnet, C. Daussy, B. Darqui'e, Y. Le Coq and A. Amy-Klein, *"Quantum cascade laser frequency stabilization at the sub-Hz level"*. Nature Photon. 9, 456 (2015)

[139] C. Clivati, G. Cappellini, L. F. Livi, F. Poggiali, M. S. de Cumis, M. Mancini, G. Pagano, M. Frittelli, A. M., G. A. Costanzo, F. Levi, D. Calonico, L. Fallani, J. Catani and M. Inguscio, *"Measuring absolute frequencies beyond the GPS limit via long-haul optical frequency dissemination"*. Opt. Express 24, 11865 (2016)

[140] M. Lombardi, *"The use of GPS disciplined oscillators as primary frequency standards for calibration and metrology laboratories, NCSLI Measure"* J. Meas. Sci. 3, 56 (2008)

[141] C. Clivati, A. Mura, D. Calonico, F. Levi, G. A. Costanzo, C. E. Calosso and A. Godone, *"Planar-waveguide external cavity laser stabilization for an optical link with 10-19 frequency stability"*. IEEE Trans. Ultrason. Ferroelectr. Freq. Control 58, 2582 (2011)

[142] D. Calonico, E. K. Bertacco, C. E. Calosso, C. Clivati, G. A. Costanzo, M. Frittelli, A. Godone, A. Mura, N. Poli, D. V. Sutyrin, G. Tino, M. E. Zucco and F. Levi, *"High-accuracy coherent optical frequency transfer over a doubled 642 km fiber link"*. Appl. Phys. B 117, 979 (2014)

·– –